PERFORMANCE EVALUATION OF A GROUND MOTION MODEL APPLICABLE TO HARD ROCK SITE CONDITIONS FOR TURKEY

A THESIS SUBMITTED TO
THE GRADUATE SCHOOL OF NATURAL AND APPLIED SCIENCES
OF
MIDDLE EAST TECHNICAL UNIVERSITY

BY

ONUR KANUN

IN PARTIAL FULFILLMENT OF THE REQUIREMENTS
FOR
THE DEGREE OF MASTER OF SCIENCE
IN
CIVIL ENGINEERING

JULY 2023

Approval of the thesis:

PERFORMANCE EVALUATION OF A GROUND MOTION MODEL APPLICABLE TO HARD ROCK SITE CONDITIONS FOR TURKEY

submitted by **ONUR KANUN** in partial fulfillment of the requirements for the degree of **Master of Science in Civil Engineering, Middle East Technical University** by,

Prof. Dr. Halil Kalıpçılar
Dean, Graduate School of **Natural and Applied Sciences** _____

Prof. Dr. Erdem Canbay
Head of the Department, **Civil Engineering** _____

Assoc. Prof. Dr. Onur Pekcan
Supervisor, **Civil Engineering, METU** _____

Prof. Dr. Zeynep Gülerce
Co-Supervisor, **Civil Engineering, METU** _____

Examining Committee Members:

Prof. Dr. Berna Unutmaz
Civil Engineering, Hacettepe University _____

Assoc. Prof. Dr. Onur Pekcan
Civil Engineering, METU _____

Prof. Dr. Zeynep Gülerce
Civil Engineering, METU _____

Assoc. Prof. Dr. Atilla Arda Özacar
Geological Engineering, METU _____

Assoc. Prof. Dr. M. Abdullah Sandıkkaya
Civil Engineering, Hacettepe University _____

Date: 07.07.2023

I hereby declare that all information in this document has been obtained and presented in accordance with academic rules and ethical conduct. I also declare that, as required by these rules and conduct, I have fully cited and referenced all material and results that are not original to this work.

Name Last name: Onur Kanun

Signature:

ABSTRACT

PERFORMANCE EVALUATION OF A GROUND MOTION MODEL APPLICABLE TO HARD ROCK SITE CONDITIONS FOR TURKEY

Kanun, Onur
Master of Science, Civil Engineering
Supervisor: Assoc. Prof. Dr. Onur Pekcan
Co-Supervisor: Prof. Dr. Zeynep Gülerce

June 2023, 94 pages

One of the most common methods used in earthquake engineering applications is to determine the design ground motion parameters for engineering bedrock conditions using ground motion models (GMMs). Then, by modeling the response of the soil layers overlying the engineering bedrock, a site-specific response spectrum is developed. This process requires that the GMM is applied to stiff/hard rock site conditions with high shear wave velocity (V_S) values (V_S>1100 m/s). The application of GMMs to stiff/hard rock site conditions involves several uncertainties due to the limited amount of ground motion data compiled from hard rock site conditions (Bard et al., 2019). In order to overcome the data sparsity, deconvolution of surface ground motions by 1-dimensional (1-D) soil response analysis may be applied to obtain ground motion values on deeper and stiffer soil layers (Laurendeau et al., 2018). The objective of this study is to evaluate the performance of GMMs applicable to hard rock site conditions using the strong ground motion network managed by the Turkish Disaster and Emergency Management Presidency (AFAD). By examining the site characterization reports of

AFAD stations, 40 candidate stations and 2977 strong motion recordings were selected for this study. By utilizing the V_S profile of these stations, 1-D ground response analyses were performed and ground motion records in the engineering bedrock were estimated using the recorded ground motions on the surface. The performance of the Laurendeau et al. (2018) model to predict the deconvolved ground motions was evaluated by using the analysis of residuals. Analysis results showed that the selected GMM is applicable for earthquake engineering applications in Turkey for hard rock site conditions.

Keywords: Ground motion model, Deconvolution, Hard rock GMMs, Ground response analysis, 1-D equivalent linear analysis

ÖZ

TÜRKİYE İÇİN SERT SAHA KOŞULLARINA UYGULANABİLECEK BİR KUVVETLİ YER HAREKETİ TAHMİN DENKLEMİNİN PERFORMANS DEĞERLENDİRMESİ

Kanun, Onur
Yüksek Lisans, İnşaat Mühendisliği
Tez Yöneticisi: Doç. Dr. Onur Pekcan
Ortak Tez Yöneticisi: Prof. Dr. Zeynep Gülerce

Haziran 2023, 94 sayfa

Deprem mühendisliği uygulamalarında kullanılan en yaygın yöntemlerden biri kuvvetli yer hareketi tahmin denklemlerini kullanarak mühendislik anakayası için tasarım yer hareketi değerlerini belirlemektir. Sonrasında, mühendislik anakayası üzerinde yer alan zeminlerin davranışı da modellenerek sahaya özel tepki spektrumu oluşturulur. Bu süreç, kuvvetli yer hareketi tahmin denklemlerinin kayma dalgası hızı (V_S) yüksek (V_S>1100 m/s) sert saha koşulları için kullanılmasını gerektirmektedir. Kuvvetli yer hareketi tahmin denklemlerinin sert saha koşullarına uygulanması, sert saha koşullarından derlenen yer hareketi verisinin sınırlı olması nedeniyle çok sayıda belirsizlik içermektedir (Bard vd., 2019). Veri sayısını arttırabilmek için, 1-boyutlu (1-B) zemin tepki analizi ters yönde uygulanarak sert zemindeki yer hareketi değerleri elde edilebilir (Laurendeau vd., 2018). Bu çalışmanın amacı, Türkiye Afet ve Acil Durum Yönetimi Başkanlığı (AFAD) tarafından yönetilen kuvvetli yer hareketi ağını kullanarak Türkiye için sert kaya koşullarına uygulanabilir bir kuvvetli yer hareketi tahmin denkleminin performansını değerlendirmektir. AFAD istasyonlarının saha

karakterizasyonu raporları incelenerek, bu çalışmada kullanılabilecek 40 adet aday istasyon ve bu istasyonlarda kaydedilen 2977 adet yer hareketi kaydı derlenmiştir. Bu istasyonların kayma dalgası hız profili modellenerek 1-B zemin tepki analizleri yapılmış ve yüzeydeki yer hareketinden yola çıkarak mühendislik anakayasındaki yer hareketi kayıtları elde edilmiştir. Analizler sonucu oluşturulan ve sert saha koşullarını temsil eden yer hareketi veri seti kullanılarak, V_S>1100 m/s sahalar için geçerli Laurendeau vd. (2018) tahmin denkleminin performansı artıkların analizi yöntemi ile değerlendirilmiştir. Analiz sonuçları Laurendeau vd. (2018) tahmin denkleminin Türkiye'de yapılacak sert zemin koşullarındaki mühendislik uygulamalarında kullanılabileceğini göstermektedir.

Anahtar Kelimeler: Yer hareketi tahmin denklemi, Geriye tepki analizi, Sert kaya, Sahaya özel tepki analizi, 1-B eşdeğer lineer analiz

Dedicated to those who lost their lives in the 6 February earthquake…

ACKNOWLEDGMENTS

I would like to express my sincere appreciation to my advisor Assoc. Prof. Dr. Onur Pekcan for his guidance, and support throughout my research journey. His presence and insights provided valuable perspective and encouragement.

I am immensely grateful to Prof. Dr. Zeynep Gulerce for her invaluable guidance, unwavering support, and expert supervision throughout the entire research process. Her profound knowledge and constant encouragement have been instrumental in shaping this thesis and enhancing its quality.

I would also like to extend my heartfelt appreciation to Assoc. Prof. Dr. Abdullah Sandıkkaya for his valuable input during the course of my research. His expertise and willingness to share his knowledge have been immensely beneficial in shaping the direction of my work.

I would like to extend my heartfelt appreciation to all the jury members that spent their valuable time on my thesis process, and to faculty members at METU Civil Engineering Department for their commitment to excellence in education, and their valuable contributions to my academic development.

I would like to express my deepest gratitude to my wife, Zeynep Kanun, for her love, support, and understanding throughout this challenging journey. Her patience, encouragement, and belief in my abilities have been a constant source of motivation, and I am truly grateful for her presence in my life.

To my beloved parents, I thank them for their unconditional love, encouragement, and continuous support throughout my academic journey. Their belief in me has been a driving force behind my accomplishments, and I am forever grateful for their sacrifices and faith in me.

Lastly, I would like to acknowledge my friends, Sencer Kaçar and Burak Akbaş, for their constant support during the course of my research.

TABLE OF CONTENTS

LIST OF TABLES

TABLES

LIST OF FIGURES

FIGURES

CHAPTER 1

INTRODUCTION

Turkey is located in one of the most seismically active regions in the world. In recent earthquake engineering applications including the seismic design of high-rise buildings, bridges, and nuclear power plants, there is a need for an extensive and careful analysis of site-specific seismic hazards in such regions. As part of these seismic hazard assessment (SHA) applications, GMMs are useful tools to estimate ground motion intensities at a particular site including the characteristics of the source, path, and site effects. The uncertainties arising from the GMMs dominate the uncertainties introduced by the other models in seismic hazard analysis. Due to its importance, the selection of proper GMM is a key issue in SHA studies.

Most GMMs are developed by combining various types of sites which generally consist of soil. In most GMMs, the site effects are considered through a site parameter, the shear wave velocity at the uppermost 30 m (V_{S30}) (Laurendeau et al., 2018). Furthermore, utilizing a single parameter, V_{S30}, to represent the hard rock conditions at a site is not adequate to describe the deeper parts of the site, and to capture the actual response of the site (Laurendeau et al., 2013). In some cases, the regional evaluation of SHA for hard rock site conditions is needed since the properties of local reference bedrock vary regionally and there is a data sparsity at hard rock sites (Laurendeau et al., 2018, Bard et al., 2020). Delavaud et al. (2012) mentioned the requirement for a precise definition of the local reference rock in the use of probabilistic SHA projects (Seismic Hazard Harmonization in Europe) (Laurendeau et al., 2018). Consequently, defining the properties of local reference bedrock is considered to be a significant part of SHA. Thus, generating a ground motion dataset at hard rock sites with V_{S30} larger than 1100 m/s is needed to

estimate site-specific ground motions since currently existing GMMs are not able to make such estimations (Laurendeau et al., 2018) and a GMM applicable to hard rock site conditions is required to be used in many earthquake engineering applications.

1.1 Research Statement

The rock ground motion models (GMMs) developed in the current literature are quite limited and were studied for different regions of the world including Central and Eastern America (CENA) (Toro et al., 1997), Eastern North America (ENA) (Campbell, 2003, Pezesk et al. 2011, Atkinson and Boore, 2006), Japan (Laurendeau et al., 2013, Edwards and Fah, 2017, Laurendeau et al., 2018), and Himalayan region (Bajaj and Anbazhagan, 2019). All of these studies were studied to develop GMMs in these regions because of the availability of an adequate number of high V_S sites. Similar to these regions, Turkey is also located in a region with many available high V_S sites, which requires ground motion predictions for large V_S for seismic hazard assessment purposes. In addition to the previous efforts on rock GMM studies, there are also limitations as regards the Turkish strong ground motion database. The compilation of comprehensive and high-quality input ground motion datasets is one of the most important parts while generating GMMs. The Turkish ground motion database was compiled by Akkar et al. (2010) under the extent of the "Compilation of Turkish strong motion network according to the international standards." The project was an important stepping stone for future ground motion studies conducted in Turkey. Also, many studies mentioned that the Turkish ground motion dataset utilized in their study was pretty limited (Akkar et al., 2014, Kale et al., 2015, Gulerce et al., 2016, Sandıkkaya and Akkar, 2017). In 2020, two different earthquakes occurred in Turkey with M>6.5, and in 2023, two earthquake events also hit the southern part of Turkey with M>7.5. These events, especially the ones that happened in 2023, increased the number of strong ground motion data and provided a fundamental requirement for a comprehensive and

well-established evaluation of the Turkish ground motion database. The limitations introduced by an inadequate number of large-magnitude earthquake data in the strong ground motion database of Turkey should be carefully evaluated for developing a GMM for hard rock sites from a high-quality and broad ground motion database with global standards.

The main objective of this study is to evaluate the performance of a GMM applicable to rock site conditions, using rock sites of a strong ground motion station database with site characterization in Turkey. For this purpose, a comprehensive and precise methodology is utilized to compile the candidate rock stations and eliminate bad-quality waveforms of ground motion recordings. Candidate rock stations from the strong ground motion database of AFAD are compiled. The information about the quality of the waveforms and the metadata information on the accelerometric data retrieved from Sandıkkaya et al. (2023) are reviewed to eliminate the bad-quality waveforms. Rock motions are retrieved from the database of PEER, and eight rock motions are selected to obtain empirical transfer functions. Empirical transfer functions are compared with theoretical transfer functions for 40 candidate stations. Site-dependent amplification factors are obtained for 40 candidate stations from input ground motion data recorded on each station. Finally, these results are used to evaluate the performance of a rock GMM using statistical regression analysis, considering the source characteristics and path influences of input ground motions, and site effects of 40 candidate stations. A significant contribution of this research is that it will be the first study to compile a rock ground motion dataset to evaluate the performance of a GMM, using the strong ground motion database of Turkey. Additionally, this extensive study attempts to complete the theoretical gap to assess the performance of a rock GMM to be used in various earthquake engineering applications including seismic hazard assessment in Turkey.

1.2 Scope of Thesis

This chapter gives general information about the study and presents the research statement with the limitations of the current literature. It also summarizes the extent of this study.

Chapter 2 presents deconvolution methodology and former studies conducted on deconvolution. A description of the site-dependent amplification factor and recent studies on the site-dependent amplification models are provided. Also, the theoretical background of hard rock GMMs and the current studies on hard rock GMMs are discussed.

Chapter 3 presents an extensive summary of the selection of candidate stations from a strong ground motion database utilized in this study. The site characterization reports as regards the strong ground motion stations are reviewed, and the selection of candidate stations is presented. The quality check of the waveforms is examined to determine the input ground motion dataset. After discussing the rock motion selection to obtain empirical transfer functions, a comparison of empirical transfer functions (ETFs) and theoretical transfer functions (TTFs) is provided.

In Chapter 4, the deconvolution methodology used in this study is illustrated with a well-structured and comprehensive flowchart. The flowchart summarizes the selection criteria used for the selection of candidate stations, the quality check of ground motion data, the procedure to model the simplified soil profiles, the deconvolution analysis, and the comparison of amplification factors of 40 candidate stations obtained from deconvolution analyses with the current literature. Further eliminations for future studies are discussed in the last part of this chapter.

Chapter 5 begins with the introduction of the features of the base model Laurendeau et al. (2018) (L18), and continues with the discussion of which parameters of our dataset are used to evaluate the performance of the L18 model. The average elastic acceleration response spectra of four GMMs of the NGA-

West2 and the L18 model are compared and discussed. The residual analysis of L18 for the Turkish ground motion dataset is presented with several plots, and the results are discussed thoroughly. After this, p values of residuals as a function of V_{S30} and V_{SROCK} are reviewed. At the end of this chapter, the conclusion of this chapter is presented as the discussion of the residual analysis of L18's performance.

In Chapter 6, an extensive summary and conclusions of the study is presented.

CHAPTER 2

CURRENT LITERATURE ON SITE RESPONSE ANALYSIS BY DECONVOLUTION

This chapter provides a summary of the current literature on site response analysis by deconvolution, site amplification factor models in ground motion prediction equations, and the ground motion prediction equations developed for hard rock site conditions.

2.1 Site Response Analysis by Deconvolution

In the practice of geotechnical earthquake engineering, site response analysis by deconvolution is a method utilized for a wide range of purposes (Kramer, 1996). One of the most common applications of the deconvolution process is to obtain input motions at a given site from the surface ground motions when there is a lack of representative rock motions (Markham et al., 2016). Another application of deconvolution is generating ground motions at a particular depth (e.g. at the control point or below the foundation) for analyzing the dynamic behavior of a soil-foundation-structure system (Idriss, 1979). The deconvolution procedure is also utilized to deconvolve the motions from the surface to the bedrock level to conduct earthquake analyses of bridges, dams, and nuclear power plants (Kabanda et al., 2015, Leger & Boughoufalah, 1989, Elgamal, 2008, as cited in Poul & Zerva, 2018).

Kramer (1996) defined deconvolution as generating the bedrock motion in the frequency domain from a known free surface motion using the inverse transfer functions. In order to define the transfer functions, surface motions were computed according to the solution given for vertical S-wave transmission in soil with

damping through multiple layers. In this analysis, the soil is assumed to be on an elastic half-space. The equation of horizontally polarized shear waves in one dimension proposed by Kramer (1996) is given in Eq. (2.1):

$$\rho \frac{\partial^2 u}{\partial t^2} = G^* \frac{\partial^2 u}{\partial z^2} \tag{2.1}$$

where,

$$G^* = G(1 + 2i\xi) \tag{2.2}$$

In Eq. (2.1) and Eq. (2.2), G* is the complex shear modulus, ρ is the density, and ξ is the damping ratio. Therefore, the solution of wave equation is given in Eq (2.3) for a periodic motion:

$$u(z,t) = Ae^{i(\omega t + k^* z)} + Be^{i(\omega t - k^* z)} \tag{2.3}$$

where,

$$k^* = \sqrt{\frac{\rho\omega^2}{G^*}} \tag{2.4}$$

In Eq. (2.3) and Eq. (2.4), ω is the angular frequency, t is the time, and k* is the complex wavenumber. The first part in Eq. (2.5) represents an ascending wave with A amplitude, while the second part represents a wave descending with B amplitude. The shear waves for harmonic waves are demonstrated as:

$$\tau(z,t) = G^* \frac{\partial u}{dz} = ik^* G^* \left(Ae^{i(\omega t + k^* z)} - Be^{i(\omega t - k^* z)}\right) \tag{2.5}$$

After declaring the local coordinate system, the shear stresses at the surface (z_m= 0) and the base (z_m= h_m) of layer m are defined as:

$$\tau(z_m,t) = G^* \frac{\partial u}{dz} = ik^* G^* \left(Ae^{i(\omega t + k^*_m z_m)} - Be^{i(\omega t - k^*_m z_m)}\right) \tag{2.6}$$

At layer boundaries, continuity of shear stresses is expressed by:

$$\tau_m(z_m = h_m, t) = \tau_{m+1}(z_{m+1} = 0, t) \tag{2.7}$$

Therefore, the wave equation is expressed as:

$$A_{m+1} - B_{m+1} = \frac{k^*_m G^*_m}{k^*_{m+1} G^*_{m+1}} \left(A_m e^{ik^*_m h_m} - B_m e^{ik^*_m h_m} \right) \quad (2.8)$$

Adding Eq. (2.6) and Eq. (2.8) and subtracting Eq. (2.8) from Eq. (2.6) redefines the equation as:

$$A_{m+1} = \frac{1}{2} A_m (1 + \alpha^*_m) e^{ik^*_m h_m} + \frac{1}{2} B_m (1 - \alpha^*_m) e^{-ik^*_m h_m} \quad (2.9)$$

$$B_{m+1} = \frac{1}{2} A_m (1 - \alpha^*_m) e^{ik^*_m h_m} + \frac{1}{2} B_m (1 + \alpha^*_m) e^{-ik^*_m h_m} \quad (2.10)$$

where α^*_m is the complex impedance ratio at the boundary between layers m an m+1, and it is given by:

$$\alpha^*_m = \frac{k^*_m G^*_m}{k^*_{m+1} G^*_{m+1}} = \frac{\rho_m (v_S^*)_m}{\rho_{m+1} (v_S^*)_{m+1}} \quad (2.11)$$

Since shear stresses at the ground surface must be equal to zero, A_1 should be equal to B_1. Therefore, Eq. (2.11) is employed for all layers and the amplitudes are expressed as:

$$A_m = a_m(\omega) A_1 \quad (2.12)$$

$$B_m = b_m(\omega) B_1 \quad (2.13)$$

The transfer functions as regards the amplitudes in terms of displacements at layer i to layer j was formulated as:

$$F_{ij}(\omega) = \left| \frac{u_i}{u_j} \right| = \frac{a_i(\omega) + b_i(\omega)}{a_j(\omega) + b_j(\omega)} \quad (2.14)$$

Eq. (2.14) also represents the acceleration and velocity amplification between layer i and layer j since for harmonic motions $|\ddot{u}| = \omega|\dot{u}| = \omega^2|u|$. Kramer (1996) stated that Eq. (2.14) makes the deconvolution process possible, and the motion at any layer could be generated if the motion at any other layer in a soil profile is known.

Deconvolution analysis has been used in geotechnical engineering practice for a long time. Recently, Paolucci et al. (2015) performed 1-D deconvolution analyses using an Italian accelerometric network (RAN) to improve mid-term and long-term seismic hazard analysis of Italy. In this study, 1-D linear and equivalent linear

deconvolution analyses in the frequency domain were performed in STRATA software (Kottke & Rathje, 2009) to acquire the accelerometric ground motion records equivalent to the reference site conditions. 100 deconvolution analyses were performed for each earthquake recording to obtain the uncertainties influencing the seismic stratigraphy of the region. For these analyses, horizontal components were used for each earthquake recording, and their geometric mean, maximum spectral acceleration (SA) at 0.15, 1, and 2 seconds of components, and maximum peak ground acceleration (PGA) of components were considered. One of the challenges in their study was the V_S measurements due to the position of the stations. Therefore, two arrays were put to develop V_S profiles in one of their stations; however, one of the dispersion curves for creating V_S profiles was not readable. To mitigate this problem, 21 different measurements were taken to be able to perform a deconvolution analysis.

Markham et al. (2016) conducted a study to evaluate the response of potentially liquefiable soils under dynamic loads using 1-D nonlinear effective stress ground response analysis. This study used nonlinear effective stress, total stress nonlinear, and equivalent linear approaches to perform seismic site response analyses; however, recorded rock motion data were sparse. To overcome the lack of representative rock motion, 1-D equivalent linear deconvolution analyses were performed. For this purpose, 6 events from the 2010-2011 Canterbury earthquake sequence for the Christchurch area were utilized to generate the input motions at the firm base material. The main source of uncertainty about generating rock motions from deconvolving surface motions arose from the selection of input surface motions. There were some consistent biases in the results of the analyses; however, the response of the sites that did or did not show liquefaction illustrated reasonable trends.

Jeong & Bradley (2017) presented a case study for capturing the site effects of Heathcote Valley during the 2010-2011 Canterbury earthquake sequence by utilizing 1-D nonlinear dynamic finite element analyses with the use of recorded ground motions. In this study, simulations were performed in the finite element

analysis program OpenSees (Mazzoni et al., 2006); however, the absence of input ground motions for the simulations required deconvolving surface motions to the bedrock motion at a target depth. Therefore, recorded surface motion located at the Lyttelton Port was utilized to perform 1-D equivalent linear deconvolution analyses by using the Thomson-Haskell transfer matrix method.

Cabas & Rodriguez-Marek (2017) conducted a study about for V_S-κ_0 correction applied to input ground motions used in ground response analyses. In this study, the Japanese database Kiban-Kyoshin (KiK-net) was utilized. Correction factors of V_S-κ_0 were implemented on their input ground motion dataset, and they were reviewed in comparison with the conventional deconvolution approach proposed by Schnabel et al. (1972) & Kramer (1996). The main limitation of this study was that the V_S-κ_0 framework is only applicable when the V_S profile of the site is available. The V_S profile might not be available on some sites. Therefore, the deconvolution methodology might not be useful to generate rock motions at such sites.

Poul & Zerva (2018) performed equivalent linear deconvolution analyses of ground motions for soil-structure interaction (SSI) analyses. In this study, all three components (two horizontal and one vertical) of surface ground motion recordings were utilized. The target (design) surface ground motions were deconvolved through an equivalent-linear medium with viscoelastic behavior and multiple layers using the phase-amplitude modification. These deconvolved motions at a specific depth were used for finite element time-domain SSI analyses.

Ashayeri et al. (2021) conducted a seismic microzonation study for the Sarpol-e-zahab area in Iran after November 12, 2017 (M_w=7.3) Iran earthquake. This study aimed to propose maps for the Sarpol-e-zahab area in terms of site amplification factors and ground shaking levels. For this purpose, deconvolution of ground motions recorded in the closest station to the epicenter of the earthquake, coded ISMN-SPZ, was performed to generate horizontal bedrock motions. Deconvolution analyses were performed in the frequency domain using the

equivalent linear approach in ground response analysis software DEEPSOIL (Hashash et. al., 2017). After generating bedrock motions, convolution of bedrock motions was performed to obtain ground motions at 38 different points in the Sarpol-e-zahab area.

2.2 Pioneering and Recent Studies on Site Amplification Factors

In earthquake engineering design practice, local site conditions have a vital effect on the intensity of earthquake shaking and damage. Gutenberg (1927) was one of the first to develop site-dependent amplification factors from ground motion recordings for various site conditions, followed by several other pioneering studies (e.g. Seed and Idriss, 1971). Kramer (1996) defined the amplification factor (AF) as the amplitude proportion between the surface motion and the bedrock outcropping motion. One of the methods to determine the amplification factor is by performing ground response analysis and AF is calculated by the following equation using the proportion between soil and bedrock (Borcherdt, 1970, as given in Akin et al., 2013):

$$\mathrm{AF} = \frac{\mathrm{IM_{soil}}}{\mathrm{IM_{bedrock}}} \tag{2.15}$$

where IM is the intensity measure (e.g. peak ground accelerations).

In current practice, site-amplification models in ground motion models (GMMs) that simulate the behavior of soil are used to illustrate the influence of local site conditions through simplified functional forms. These functional forms are generally generated either through empirical datasets or through stochastic simulations. The traditional method used to represent the local site conditions in GMMs is amplification factors. This is done through the normalization of a ground motion intensity at a particular site. Another method is used to represent the local site effects through the use of stochastic methods. This method uses simulations to generate site amplification models by establishing a model between bedrock and

surface motion based on different functional forms for various site conditions (Sandıkkaya et al., 2013).

Early-state ground motion prediction models include simplified functional forms for site amplification terms. For example, Boore et al. (1997) proposed GMM based on Western North American earthquakes. In this study, V_{S30} values of the sites included were ranging from 180 - 750 m/s. The amplification factor was defined as the amplification of soil with respect to the reference bedrock with a shear wave velocity greater than 750 m/s. The proposed linear site amplification model lacked the nonlinear term and V_{S30} was presented to be a continuous variable of their model as shown in Eq. (2.16):

$$\ln(\mathrm{Amp}) = a\ln\left(\frac{V_{S30}}{V_{REF}}\right) \tag{2.16}$$

Abrahamson & Silva (1997) developed a GMM for shallow crustal earthquakes. The site term included in this GMM accounted for the nonlinear behavior of soil, which Boore et al. (1997) lacked. The site amplification model was proposed as the function of PGA_{rock} (the estimated PGA on reference rock, which was the predicted median spectral acceleration at T=0 seconds) representing the model's nonlinearity. However, the model did not include shear wave velocity dependency since the related information about the sites was not available. Therefore, the nonlinear site amplification model proposed was:

$$\ln(\mathrm{Amp}) = a + b\ln\left(\widehat{PGA}_{rock} + c\right) \tag{2.17}$$

Choi & Stewart (2005) developed an empirical nonlinear site amplification factor model based on V_{S30} with reference sites of 760 m/s and a baseline shaking level of 0.1g. The soil sites included in this study were grouped based on NEHRP's (1994) site classification. Soft clays with undrained shear strength less than 24 kPa, plasticity index greater than 20, and water content greater than 40% were included in addition to all types of soil classes ranging from A to E. The first term of the proposed model was similar to Boore et al. (1997), which was a function of V_{S30}.

This study extended the V_{S30}-dependent linear model, including nonlinearity through the b term. The proposed functional form is given by:

$$\ln(\text{Amp}) = \text{a}\ln\left(\frac{V_{S30}}{V_{ref}}\right) + \text{b}\ln\left(\frac{PGA_{rock}}{0.1}\right) \tag{2.18}$$

Walling et al. (2008) conducted a study on nonlinear site amplification factors generated using the equivalent-linear approach for constraining the NGA GMMs (Ancheta et al., 2014, Bozorgnia et al., 2014). In this study, the site response analysis was performed by the random vibration theory approach in RASCALS (Silva & Lee 1987) software. V_{S30} of sites included in the study varied between 160 and 900 m/s while the depth of soil profiles changed between 15 and 914 meters. Four different types of dynamic soil properties were utilized: Imperial Valley, EPRI, Peninsular Range, and Bay Mud. The reference bedrock was considered to be 1100 m/s, and the PGAs of the input rock motion changed between 0.01 and 1.5g. The proposed model was dependent on V_{S30} when the soil behavior was linear similar to Boore et al. (1997). In addition to Boore et al. (1997)'s model, the term d was added to illustrate the conditions when V_{LIN} was not the reference velocity. It also included PGA_{rock} dependency similar to Abrahamson & Silva (1997) with an additional V_{S30} function. The general form of the site amplification model was given by:

$$\ln(\text{Amp}) = \begin{cases} \text{a}\ln\left(\frac{V_{S30}}{V_{LIN}}\right) - \text{b}\ln(PGA_{rock} + \text{c}) \\ +\text{b}\ln\left(PGA_{rock} + \text{c}\left(\frac{V_{S30}}{V_{LIN}}\right)^{\text{n}}\right) + \text{d} & \text{for } V_{S30} < V_{LIN} \\ (\text{a} + \text{bn})\ln\left(\frac{V_{S30}}{V_{LIN}}\right) + \text{d} & \text{for } V_{S30} \geq V_{LIN} \end{cases} \tag{2.19}$$

Sandıkkaya et al. (2013) proposed linear and nonlinear site amplification models applicable to the next Pan-European ground motions models. Sandıkkaya et al. (2013) used the general form proposed by Walling et al. (2008), yet only utilized empirical data to estimate the regression coefficients. For this purpose, V_{S30} of the different sites from the database of the pan-European region was utilized. It was recommended to use the model ranging from 150 m/s to 1200 m/s for V_{S30}. V_{CON} was introduced to limit amplifications for V_{S30} larger than 1 km/s, and the shear

wave velocity of reference bedrock (V_{REF}) was considered to be 750 m/s. PGA_{REF} was represented as the maximum ground acceleration of input rock motion at V_{REF}. The proposed site model was given by:

$$\ln(\text{Amp}) = \begin{cases} a\ln(V_{S30}/V_{REF}) \\ \quad + b\ln\left[\frac{PGA_{REF}+c(V_{S30}/V_{REF})^n}{(PGA_{REF}+c)(V_{S30}/V_{REF})^n}\right] & \text{for } V_{S30} < V_{REF} \\ a\ln(V_{S30}/V_{REF}) & \text{for } V_{REF} \le V_{S30} < V_{CON} \\ a\ln(V_{CON}/V_{REF}) & \text{for } V_{S30} \ge V_{CON} \end{cases} \quad (2.20)$$

Seyhan & Stewart (2014) analyzed NGA-West2 data and performed site-response simulations for developing a semi-empirical site amplification model with V_{S30} and nonlinear soil effects. In this study, five different soil classes with representative V_{S30} were considered according to NEHRP (2014), and the median value of all GMMs of the NGA-West2 Project was taken. The model consisted of both linear and nonlinear parts, and the sum of them was introduced as the response spectrum amplification term ($F_{S,B}$). The linear part of site amplification was a function of V_{S30} whereas the nonlinear part was dependent on both V_{S30} and the PGA_{rock} with a reference velocity of 760 m/s. V_c was introduced as the velocity that limits the ground motion scaling with V_{S30}. PGA_{rock} represented the median peak ground acceleration at reference bedrock, and f_2 was a function of period and V_{S30}. The proposed model was given by:

$$F_{S,B} = \ln(F_{lin}) + \ln(F_{nl}) \quad (2.21)$$

$$\ln(F_{lin}) = \begin{cases} c\ln\left(\frac{V_{S30}}{V_{ref}}\right) & \text{for } V_{S30} \le V_c \\ c\ln\left(\frac{V_c}{V_{ref}}\right) & \text{for } V_{S30} > V_c \end{cases} \quad (2.22)$$

$$\ln(F_{nl}) = f_1 + f_2\ln\left(\frac{PGA_{rock}+f_3}{f_3}\right) \quad (2.23)$$

$$f_2 = f_4[\exp\{f_5\min(V_{S30}, 760) - 360\} - \exp\{f_5(760-360)\}] \quad (2.24)$$

Recently, Stewart et al. (2020) conducted a study to develop ergodic linear site amplification models applicable to Central and Eastern North America (CENA). This model was also used in this thesis to compare the amplification factors which

are empirically produced for each candidate station. The proposed model included both linear and nonlinear site effects, and it was one of the most complicated models in the current literature. The nonlinear component of the amplification model was presented by Hashash et al. (2020). In this study, a linear component of the model was separated into two parts including the V_{S30}-scaling model (F_V) and the F_{760} model. In the F_V model, V_l and V_u represented the limiting lowest and uppermost velocities that the model applicable (200 and 2000 m/s, respectively.), and V_{ref} was considered to be 760 m/s. F_{760} model aimed to adjust the ground motion intensities between the local bedrock with V_S equal to 3000 m/s and the reference bedrock of CENA with V_S equal to 760 m/s, depending on the period. The linear part of the model is presented in the equations below:

$$F_S = F_{lin} + F_{nl} \tag{2.25}$$

$$F_{lin} = F_V(V_{S30}, T) + F_{760}(V_{S30}, T) \tag{2.26}$$

$$F_V = \begin{cases} c\ln\left(\frac{V_1}{V_{ref}}\right) & \text{for } V_l < V_{S30} \le V_1 \\ c\ln\left(\frac{V_{S30}}{V_{ref}}\right) & \text{for } V_1 < V_{S30} \le V_2 \\ c\ln\left(\frac{V_2}{V_{ref}}\right) & \text{for } V_2 < V_{S30} \le V_u \\ c\ln\left(\frac{V_2}{V_{ref}}\right) - \left[c\ln\left(\frac{V_2}{V_{ref}}\right) + F_{760}\right]\left[\frac{\ln\left(\frac{V_{S30}}{V_u}\right)}{\ln\left(\frac{3000}{V_u}\right)}\right] & \text{for } V_2 < V_{S30} \le V_u \end{cases} \tag{2.27}$$

$$F_{760}(V_{S30}, T) = w_{imp}(V_{S30}){F^{imp}}_{760}(T) + w_{gr}(V_{S30}){F^{gr}}_{760}(T) \tag{2.28}$$

$$w_{imp}(V_{S30}) = \begin{cases} w_1 & for\ V_{S30} \ge V_{w1} \\ (w_1 - w_2)\left[\frac{\ln\left(\frac{V_{S30}}{V_{w2}}\right)}{\ln\left(\frac{V_{w1}}{V_{w2}}\right)}\right] + w_2 & for\ V_{w2} \le V_{S30} < V_{w1} \\ w_2 & for\ V_{S30} < V_{w1} \end{cases} \tag{2.29}$$

$$w_{gr} = 1 - w_{imp} \tag{2.30}$$

Hashash et al. (2020) is a companion study of Stewart et al. (2020), and the nonlinear component of the site amplification model was proposed. The scope of the study was to develop ergodic nonlinear site amplification models CENA by performing one-dimensional (1-D) site-response analyses. This model was similar

to the nonlinear component proposed by Seyhan & Stewart (2014). The first difference was the introduction of V_c in the nonlinear component, which was the limiting V_{S30} for nonlinear site effects. The second difference was the reference condition of 3000 m/s (V_{ref}), which was considered as 760 m/s by Seyhan & Stewart (2014). Furthermore, $I_{r,3000}$ was the peak ground acceleration at reference with V_{ref}. The nonlinear site model was given by:

$$F_{nl} = \begin{cases} f_2 \times \ln\left[\frac{(I_{r,3000}+f_3)}{f_3}\right] & \text{for } V_{S30} < V_c \\ 0 & \text{for } V_{S30} \geq V_c \end{cases} \quad (2.31)$$

$$f_2 = f_4[\exp\{f_5 \min(V_{S30}, V_{ref}) - 360\} - \exp\{f_5(V_{ref} - 360)\}] \quad (2.32)$$

$$I_{r,3000} = \frac{I_{r,760}}{2.275} \quad (2.33)$$

2.3 Ground Motion Models Applicable to Hard Rock Site Conditions

In the applications of seismic design, GMMs are a useful tool to estimate the ground motion intensity parameters at a given site. The prediction of ground motions for hard rock sites is especially crucial because critical infrastructure, such as nuclear power plants, is generally located on rock site conditions (Laurendeau et al., 2018 & Laurendeau et al., 2013). In the current practice of GMMs, the use of GMMs is limited for predicting a site with V_{S30} greater than 1000 m/s (Laurendeau et al., 2018). Since the derivation of GMMs is generally done by using both soil and rock motions, there is a significant sparsity in the number of recordings on hard rock stations that are utilized in empirical GMMs. Thus, the ground response scaling in the GMMs cannot be deduced to hard rock site conditions (Laurendeau et al., 2013 & Atik et al., 2022). For this purpose, the prior hazard estimation at reference bedrock is needed, since the local reference bedrock is often corresponding to “hard rock” with shear wave velocity larger than 1500 m/s. The adjustment for “standard rock” seismic hazard estimates should be done to reflect the real characteristics of local reference bedrock (Bard et al., 2020). The conventional application to do this is by computing scaling factors depending on

V_S (shear-wave velocity) and κ_0 (site-specific high-frequency attenuation parameter), which is called the host-to-target adjustment (HTTA). However, in comparison to a standard rock, this adjustment generally estimates hard rock motions with larger high-frequency content, and this is affected by large uncertainties (Al Atik et al., 2014, as cited in Bard et al., 2020).

Alternative approaches were used to eliminate the level of uncertainties in estimating the ground motions at hard rock site conditions in the past. An alternative approach is to calibrate GMMs in the Fourier domain (Bora et al., 2015 as given in Bard et al., 2020) for target sites. The variability related to the back-and-forth conversion between Fourier and response spectrum domain can be eliminated with the use of this method. Other methods are utilizing hard rock surface motions to develop empirical models (Ktenidou et al., 2016 as given in Bard et al., 2020) or scaling generic GMMs to the site-specific ground motion by utilizing the site residuals if there is an adequate number of recordings (Kotha et al., 2017 & Ktenidou et al., 2018 as given in Bard et al., 2020). The final method is the direct derivation of hard rock GMMs which would apply to hard rock site conditions (Bard et al., 2020). Rock and soil stiffness (with the use of V_{S30}) is the basis for this method similar to the previously developed GMMs, and GMMs can directly be applied to local bedrock with large V_S without making any adjustments. This method is conducted by performing a ground response analysis, and it is the methodology used in this thesis.

One of the first hard rock GMMs was developed by Toro et al. (1997) using CENA database. Four different GMMs were developed (2 crustal regions and 2 magnitude scales). The GMM is applicable in a frequency range of 1 - 35 Hz, a distance range between 1 and 500 km, and a magnitude range of 5 to 8. The results of the model was applicable to hard rock site conditions with an average shear wave velocity of 2800 m/s, and with three different kappa values such as κ_0=0.002 s, 0.006 s, 0.012 s. To obtain predictions for soil sites, the model suggested using amplification factors provided by EPRI (1993) and Silva et al. (1996).

In 2003, Campbell developed a hybrid empirical GMM for Eastern North America (ENA) using GMMs from Western North America (WNA) to adjust GMMs from one region to another. In this study, the model accounted for the stress drop, source properties, crustal attenuation, structural difference between regions, and the profiles of generic rock sites between two regions. The empirical GMM presented was developed from hard rock sites that have V_S=2800 m/s and κ_0=0.002 s, 0.006 s, 0.012 s, using ground motion data of $M_w \geq 5.0$, and $R_{rup} \leq 70$ km.

After these studies, Atkinson and Boore (2006) presented a new GMM for both hard rock and soil sites located in eastern North America (ENA). The GMM included ground motions from events with a magnitude larger than 5, and distances less than 100 km. The shear wave velocities of the sites of ENA generally had an average of 2000 m/s, and κ_0 between 0.002 and 0.008. Due to the scarcity of data in these magnitude and distance ranges, the GMMs were developed from simulated ground motion data rather than using a regression analysis from empirical ground motion data. In addition to predictions for hard rock sites, an estimation for reference conditions (V_S= 760 m/s, B/C boundary) according to National Earthquake Hazards Reduction Program (NEHRP) was also provided in this study.

Laurendeau et al. (2013) conducted a study on developing a site amplification model for stiff-soil and rock sites based on κ_0 and V_{S30}. In this study, a GMM specific to stiff-soil and rock sites was developed based on large V_S sites in Japan, and the site amplification model in GMM was analyzed to understand the dependency on V_{S30} and κ_0. The GMM included sites with V_{S30} between 500 m/s and 1500 m/s, and events with magnitudes between 4.5 and 6.9. Japan databases including KiK-net and K-NET were utilized for the ground motion data. Some selection criteria were utilized to build an input ground motion dataset. Earthquakes events from the beginning of April 1999 until the end of 2009 are used. Abrahamson and Silva's (1992) random effect approach was used to derive the coefficients of GMM. A new functional form was not developed, and it was rather based on Rodriguez-Marek et al. (2011)'s model. Functional form of the model is given in Eq. (2.34):

$$\ln(SA_{ij}) = F_{M_i} + F_{D_{ij}} + F_{S_j} + \delta W_{ij} + \delta B_i \quad (2.34)$$

where i and j are the event and station, respectively. δW_{ij} and δB_i are the within-event residuals and between-event residuals, respectively. F_M, $F_{D,}$ and F_S are the functions of magnitude, distance, and site model, respectively, and their equations are given by:

$$F_{M_i} = \begin{cases} a_1 + a_2(M_{W_i} - M_h) + a_3(M_{W_i} - M_h)^2 & \text{for } M_{W_i} \leq M_h \\ a_1 + a_4(M_{W_i} - M_h) & \text{for } M_{W_i} > M_h \end{cases} \quad (2.35)$$

$$F_{D_{ij}} = [b_1 + b_2(M_{W_i} - 4.5)]\ln(R_{ij}/1) + b_3(R_{ij} - 1) \quad (2.36)$$

$$R_{ij} = \sqrt{R^2{}_{RUP_{ij}} + h^2} \quad (2.37)$$

$$F_{S_j} = c_1 \ln(V_{S30_j}/800) \quad (2.38)$$

Laurendeau et al. (2018) developed a hard rock GMM for sites that have V_S ranging from 1000 m/s and 3000 m/s using downhole and surface recordings obtained from the Japanese KiK-net database. In this study, the V_{S30} of ground motion stations of the Japanese database varied between 500 m/s and 1350 m/s. The lower boundary for the applicability was the same for Laurendeau et al. (2013); however, the uppermost boundary was increased. Two different corrections related to the hard rock sites with V_S between 1000 and 3000 m/s were made to generate two virtual datasets. These corrections included the modification of within motions from down-hole recordings to outcropping motions by correcting with depth factor and the deconvolution of surface recordings by performing 1-D site-specific response analysis simulations. For the input ground motion dataset, the KiK-net dataset compiled by Laurendeau et al. (2013) was utilized. The input dataset contained 2086 six-component recordings from 272 different events and 164 sites. The magnitude of earthquake events ranged from 3.5 to 6.9 similar to Laurendeau et al. (2013). The distance varied between 4 and 290 kilometers. After creating the dataset, and performing the analyses, GMM was developed with the appropriate site term. The geometrical mean of two horizontal components is

derived from Abrahamson & Silva's (1992) random effects regression method, and a simple functional form was generated as given by:

$$\ln\left(\mathrm{SA(T)}\right)_{es} = a_1(T) + a_2(T)M_W + a_3(T)M^2{}_W + b_1(T)R_{RUP} - \ln(R_{RUP}) + c_1(T)\ln(V_S/1000) + \delta B_e(T) + \delta W_{es}(T) \quad (2.39)$$

where SA(T) is the spectral acceleration for the period T. δB_e and δW_{es} stand for the inter-event and intra-event variability in turn. a_1, a_2, a_3, b_1, c_1 are the coefficients derived from regression analysis. M_w is moment magnitude, R_{RUP} is the rupture distance in km, and V_S is the shear wave velocity of the corresponding site. V_S can be either taken as V_{S30} or the shear wave velocity at the down-hole sensor (V_{SDH}).

CHAPTER 3

DATA COMPILATION

The Disaster and Emergency Management Presidency (AFAD) of Turkey operates 1039 strong ground motion recording stations. These stations are spread all over Turkey and Northern Cyprus but are densely populated in seismically active regions. The strong-motion database of Turkey is disseminated through the website of AFAD (https://tadas.afad.gov.tr/; last accessed on: 31.12.2022). This website is called TADAS hereafter.

To determine candidate stations for this study, station information, topography class, technical information, ground motion records, and site characterization reports were accessed from TADAS. Even though there are 1039 recording stations available in TADAS, site characterization reports of 539 are not available. Hence, these stations are eliminated. At some stations, two different site characterization studies were conducted. One set of reports is from the collaborated study of AFAD and the Geophysical Engineering Department of Kocaeli University under the scope of the AFAD National Earthquake Research program. They conducted both Multichannel Analysis of Surface Waves (MASW) and Refraction Microtremor (ReMi) techniques for shear wave velocity (V_S) profiles of 296 strong ground motion stations. They also provided a combined V_S profile of these two techniques in the site characterization reports. The second set of reports was prepared by AFAD and the Middle East Technical University (METU) Earthquake Engineering Research Center under the scope of The Scientific and Technological Research Council of Turkey (TÜBİTAK) research project entitled Compilation of Data Base

for the National Strong-Motion Seismograph Network in Turkey. In this TÜBİTAK research project, only the MASW method was used to measure the V_S profiles for 204 strong ground motion stations.

3.1 Stations with only MASW Measurement

Initially, stations with a V_S profile reaching $V_S \geq 760$ m/s were selected to represent hard rock site conditions. From these stations, the ones that met one or more of the criteria below are eliminated:

- The presence of a large reversal in V_S profiles,
- Soft soil layer presence (layers with low V_S),
- Low number of recordings at the strong ground motion station[1]

Example V_S profiles of three stations that were eliminated based on each criterion are shown in Figure 3.1.

ST1101 has a significant V_S reversal between 3 and 7 meters. There is also a dramatic decrease in V_S between 7 and 29 meters in depth, which are not "typical" in stiff soil profiles. Therefore, ST1101 and the stations with similar V_S profiles are excluded from this study.

ST1003 is eliminated due to the presence of layers with low V_S. The depth that V_S reaches over 1000 m/s is around 56 meters, and the seismic shear wave velocity of the upper 30 meters soil layer (V_{S30}) is 460 m/s, which can be considered relatively deep to represent hard rock site conditions. Also, the decrease in the accuracy of

[1] The initial limit for the minimum number of recordings was 10 per station. However, after considering the selected sites, the minimum number of recordings has occurred to be 19.

the MASW method for measurements under 30 meters strengthened the fact that the profile should be excluded. To avoid the soil amplification effects that would increase when modeling deeper soil profiles, ST1003 and the stations with a similar trend are eliminated.

ST6901 recorded 51 waveforms until January 1st, 2023. The number of recordings may be considered enough for modeling; however, the large reversal in the V_S between 2 and 7 meters, and V_S of this layer is around 250 m/s are considered as the deterrent reasons to eliminate ST6901 and stations with similar characteristics.

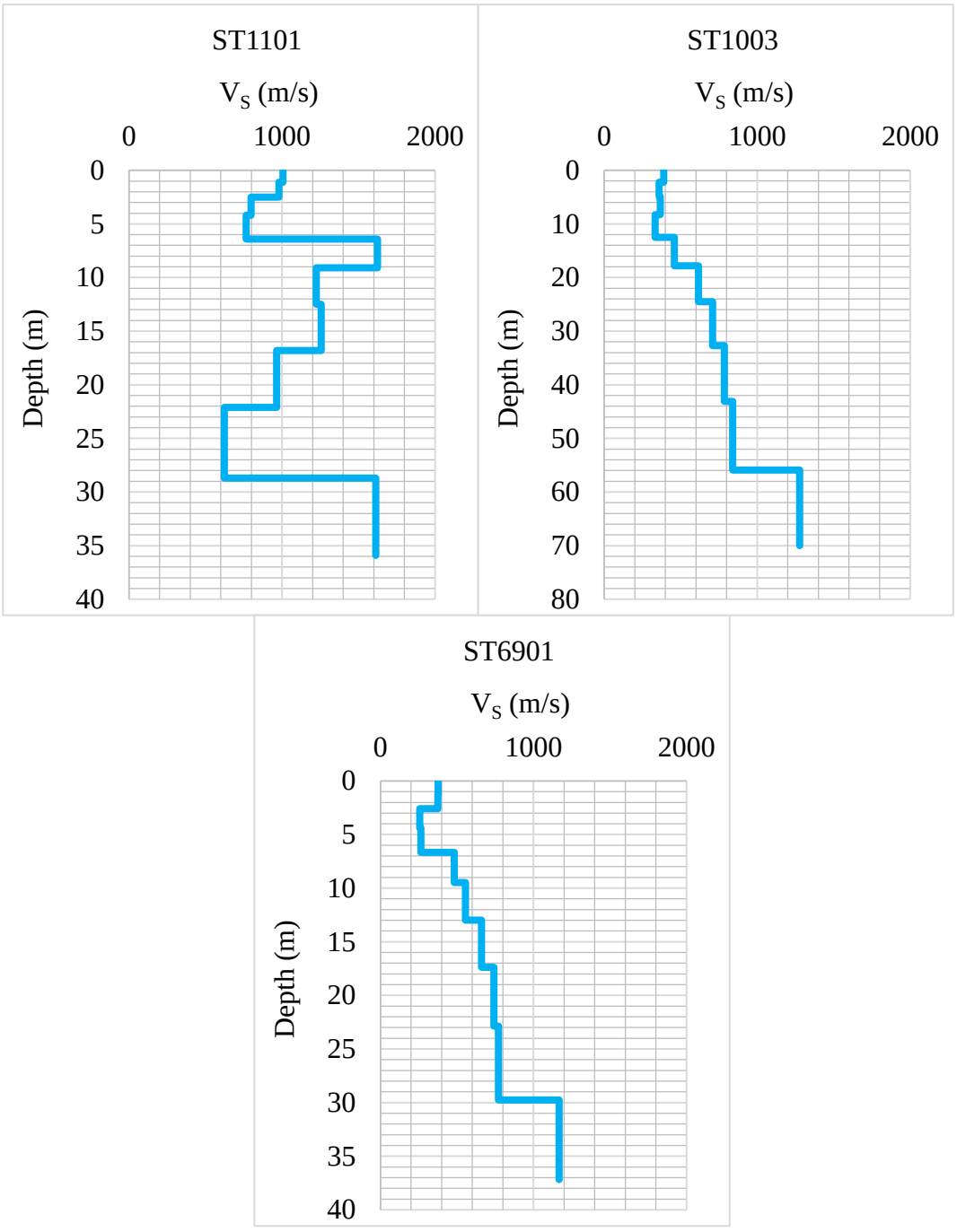

Figure 3.1. Examples of eliminated V_S profiles (ST1101, ST1003, ST6901)

Figure 3.2 shows the V_S profile of an example of the stations included in the database (ST2703). There is a smooth increment of V_S with depth without any soft soil presence. There is only a slight decrease in V_S around 5 meters; however, V_S is still above 500 m/s. In addition, the station has 88 ground motion recordings. After the elimination, 14 sites are selected and added to the station database from this group as shown in Table 3.1. The reader should refer to Appendix A for the available V_S profiles of the selected stations.

Table 3.1. Selected 14 stations with MASW measurement

Station ID	**City**	**District**	**Number of recordings**
0118	Adana	Çukurova	41
0603	Ankara	Bala	58
1009	Balıkesir	Dursunbey	408
2101	Diyarbakır	Bağlar	83
2302	Elazığ	Maden	364
2703	Gaziantep	Şahinbey	88
3602	Kars	Kağızman	34
4104	Kocaeli	Başiskele	58
4404	Malatya	Pütürge	438
4701	Mardin	Artuklu	57
4801	Muğla	Menteşe	194
4807	Muğla	Yatağan	223
6301	Şanlıurfa	Haliliye	48
6601	Yozgat	Merkez	23

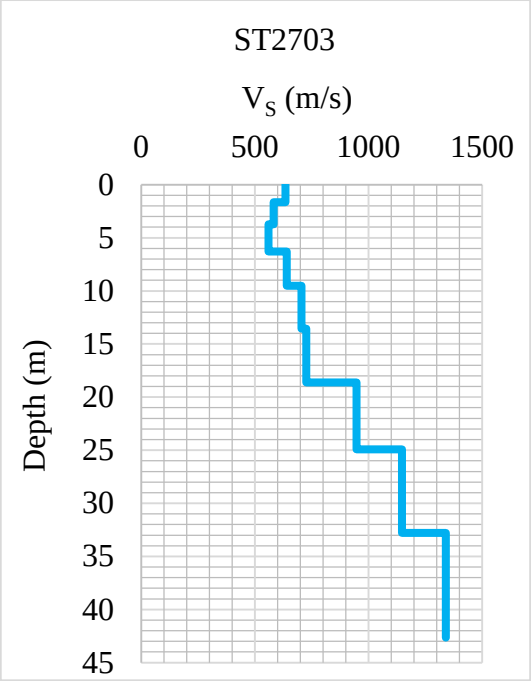

Figure 3.2. V_S profile of candidate station ST2703

3.2 Stations with MASW and ReMi Measurement

Kurtuluş et al. (2020) conducted MASW and ReMi measurements to obtain V_S profiles for site characterization of strong ground motion recording stations in Turkey under the scope of National Earthquake Research Project. In this project, the seismic shear wave velocity of sites at the uppermost 30 meters (V_{S30}) was determined by MASW method. In MASW technique, a 48-channel GEODE seismic receiver with 4.5 Hz geophones was utilized. Kurtuluş et al. (2020) selected the spacing between the receivers as 2 meters with 2 meters offset distance, and the receiver spread length was determined to be 96 meters in their analyses. In addition, the V_S for deeper parts of the stations were determined by ReMi method. They used the same 48-channel receivers with the same procedure

in the MASW for ReMi method with a passive seismic source. After the measurements, dispersion curves were obtained and MASW and ReMi methods were compared. Kurtuluş et al. (2020) also combined MASW+ReMi inversion solution from dispersion curves of these two methods to increase the accuracy of V_S profiles, and to avoid the differences between the V_S profiles and the site structure at deeper parts. They concluded that the MASW+ReMi inversion solution provides more precise V_S profiles than either MASW technique or ReMi method alone.

There are 296 strong ground motion stations with V_S profiles measured by the MASW and the ReMi methods in TADAS. These stations contain three different V_S profiles (MASW, ReMi, the combination of both), and for this study, each station is modeled with the most suitable V_S profile (for details, please see the examples below). The same procedure applied to the stations with only MASW measurement is also followed for these stations. As mentioned in the previous section, three criteria are used for the selection of stations.

Since these stations have three different V_S profiles, the elimination process is applied to three V_S profiles at each station. To be able to show the elimination process, three different stations that met each criterion separately are selected. V_S profiles of these three stations are illustrated in Figure 3.3.

ST0206 is provided as an example that satisfies the first criterion. Figure 3.3 shows that the ReMi measurement shows a significant decrease in V_S profile between 12 and 32 meters at around 500 m/s. In addition to the reversal at shallow depths, V_S exceeds 1000 m/s around 140 meters; hence, the ReMi profile is eliminated to avoid the site amplification effects. Similar to the ReMi profile, the MASW profile has a moderate V_S reversal of around 700 m/s between 8 and 16 meters in depth and is eliminated. Furthermore, the combined profile is considered unrealistic,

especially in the first 15 m and below 40 m, because its values are too high to be the combined version of the other two methods.

An example of the second criterion is ST0511, which has shear wave velocities of around 300 m/s in the first 10 meters in all three profiles. To avoid significant site amplification effects, stations with soft soil layers similar to ST0511 are excluded.

ST4119 recorded 19 ground motion recordings until January 1st, 2023, which makes it a weak candidate to consider modeling. In addition to this, there is also a presence of a large reversal at around 20 meters in depth in all three V_S profiles; therefore, ST4119 is eliminated.

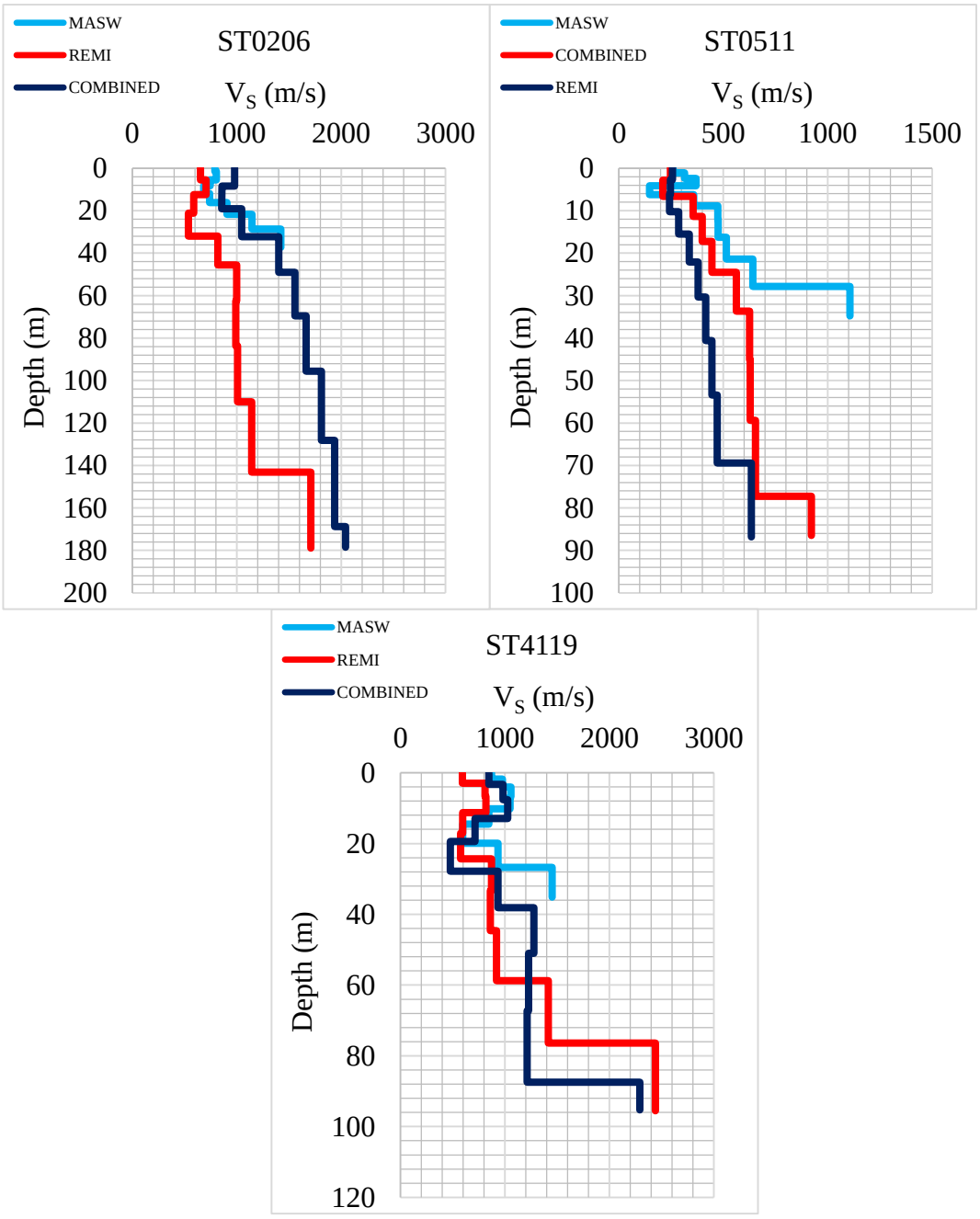

Figure 3.3. Vs profiles of eliminated stations ST0206, ST0511, ST4119

To this end, 26 strong ground motion stations with the MASW and the ReMi measurements are selected to be analyzed in this study. Table 3.2 gives information about the code, the location of stations, and the number of recordings available in each station. For further review of V_S profiles of candidate stations, refer to Appendix B.

Table 3.2. 26 candidate stations with MASW and ReMi measurement

Station ID	City	District	Number of recordings
0129	Adana	Tufanbeyli	50
0716	Antalya	Kaş	81
0919	Aydın	Karpuzlu	459
1807	Çankırı	Kurşunlu	57
2305	Elazığ	Palu	288
2309	Elazığ	Keban	277
2705	Gaziantep	İslahiye	100
2707	Gaziantep	İslahiye	77
3302	Mersin	Gülnar	31
3405	İstanbul	Kartal	67
3417	İstanbul	Sultanbeyli	77
3418	İstanbul	Tuzla	34
3517	İzmir	Buca	334
4124	Kocaeli	Körfez	19
4310	Kütahya	Tavşanlı	44
4406	Malatya	Akçadağ	289
4611	Kahramanmaraş	Çağlayancerit	146
4621	Kahramanmaraş	Dulkadiroğlu	80
4808	Muğla	Menteşe	466
4814	Muğla	Milas	356
4817	Muğla	Midas	425
4818	Muğla	Kavaklıdere	318
5202	Ordu	Akkuş	20
5814	Sivas	Gölova	50
6302	Şanlıurfa	Viranşehir	29
6303	Şanlıurfa	Siverek	31

Each candidate station had three V_S profiles. However, the most suitable V_S profile to be used in the 1-D deconvolution analyses needed to be selected. Initially, for all 26 candidate stations, the combined V_S profiles were planned to be used in the analysis since it is the method that provides the most precise results according to Kurtuluş et al. (2020). Nevertheless, the combined V_S profiles of 7 out of 26 candidate stations were not found to be suitable to be used in the 1-D deconvolution analysis. The V_S profiles measured by ReMi method was selected for stations ST2305, ST2707, ST3302, ST3405, ST4406 due to the large V_S reversal in the combined profile. In addition, for stations ST3417 and ST3418, there was a smaller V_S difference between the surface and the base rock in combined profile than the ReMi profile. As a result, the ReMi profiles were preferred over the combined profiles for 7 candidate stations, and the combined profiles were used in the analysis for the remaining 19 candidate stations.

To show examples for the selection of the ReMi profiles over the combined profiles, Figure 3.4 is provided. The MASW profile of ST2707 has several large V_S reversals, which affect the combined profile since the combined MASW+ReMi inversion solution is derived from both MASW and ReMi measurements. Due to the presence of this reversal, the combined profile would not give accurate results for 1-D deconvolution analysis; therefore, the ReMi profile is preferred for ST2707. Similarly, for ST3418, even though the combined profile could be preferred, we did not want to model the simplified soil profiles deeper since 1-D deconvolution analysis would not give accurate results. Therefore, the base rock for this station is determined to be at around 90 meters in depth. For this determined depth, the V_S difference between the surface and the base rock is smaller for the combined profile than the ReMi profile, which also affects the 1-D deconvolution analysis negatively. Thus, the ReMi profile is preferred for ST3418.

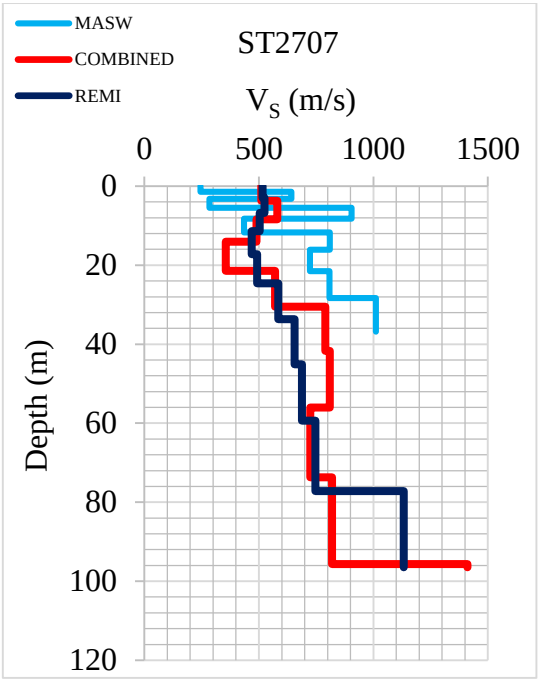

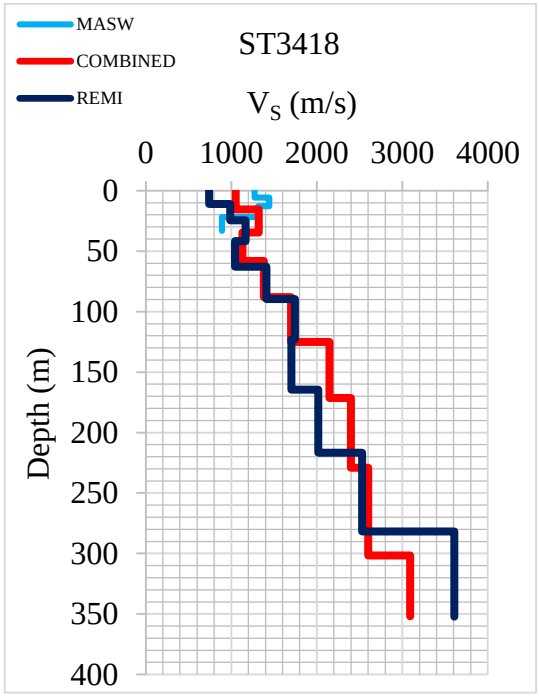

Figure 3.4. V_S profiles of candidate stations ST2707 and ST3418

The site parameters (V_{S30}, $Z_{1.0}$, $Z_{2.5}$) of the selected 40 stations are determined. V_{S30} values are directly calculated from the selected V_S profiles. Since each station has V_S values larger than 1 km/s, $Z_{1.0}$ can be calculated for all stations. However, V_S of some stations does not reach 2.5 km/s; hence, $Z_{2.5}$ is estimated using the empirical relation given below (Power et al., 2015):

$$Z_{2.5} = 0.519 + 3.595 * Z_{1.0} \quad (3.1)$$

3.3 Ground Motion Recordings

A total of 40 strong ground motion stations are selected out of 1039 stations in TADAS. 6322 records are available at these stations. The raw versions of these three-component waveforms are reviewed in terms of quality, and bad-quality waveforms are eliminated. In this sense, a visual check is done to eliminate the ones with spikes, high noise content, multiple wave groups, and incomplete trace problems. Metadata information on the accelerometric data and information about the quality of the waveforms are taken from Sandıkkaya et al. (2023). Only the recordings with good quality in both horizontal components are chosen to be used for the analyses. After this elimination, 2977 recordings from 1532 earthquakes are used for the calculations. It should be noted that the horizontal components of ground motions recorded no later than January 1st, 2023 are included. Standard processing tools of AFAD-TADAS are utilized.

After determining the input motions, the event parameters and the recording parameters are compiled. Firstly, all parameters are retrieved from the flat file provided by Sandıkkaya et al. (2023). The missing parameters are completed from TADAS. After compiling the parameters from these two sources, there are still missing parameters. For example, 2234 of 2977 ground motion recordings had M_w values assigned to them by either Sandikkaya et al. (2023) or TADAS. The

remaining 743 ground motion recordings had a local magnitude (M_L), and a duration magnitude (M_D). M_w of these 743 recordings are determined using the empirical relationship provided by Kadirioğlu and Kartal (2016) with the formulas given below:

$$M_W = 0.7947M_D + 1.3420 \quad (3.2)$$

$$M_W = 0.8095M_L + 1.3003 \quad (3.3)$$

Another event parameter compiled for the dataset is the style of faulting. The pie chart shows the style of faulting of events in the input dataset. There are 717 (24%) normal events, 657 (22%) strike-slip events, and 70 (2%) reverse earthquakes. However, the style-of-faulting information for 51% of the events is not available, and these events' style-of-faulting is left unspecified.

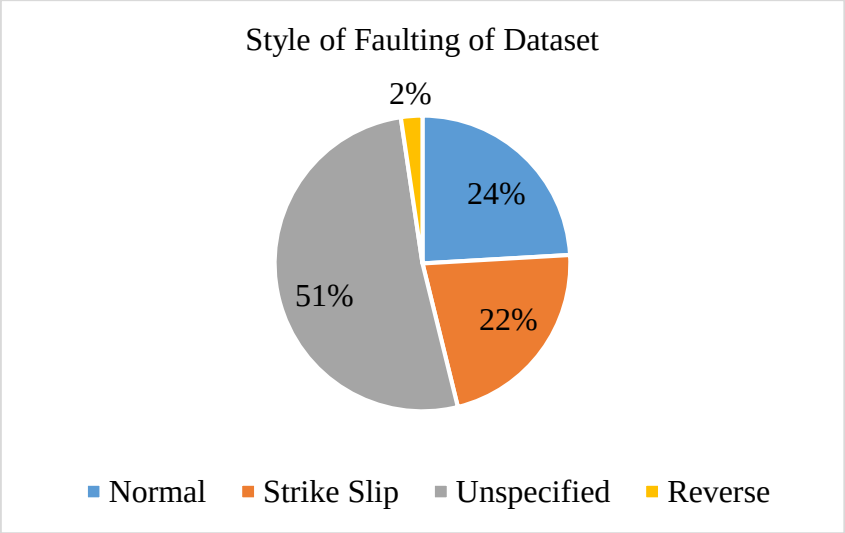

Figure 3.5. The proportion of style of faulting of the input dataset

The depth to the top of rupture (Z_{TOR}) of each event is calculated according to Mai et al. (2005)'s empirical relationship:

$$Z_{TOR} = \max[(Z_{HYP} - 0.5W\sin\delta), 0] \tag{3.4}$$

According to Eq. (3.4), hypocentral depth (Z_{HYP}), fault width (W), and dip angle (δ) are needed to determine Z_{TOR}. Z_{HYP} is calculated based on the fault type according to Sherbaum et al. (2004)'s empirical relationship provided below:

$$Z_{HYP} = \begin{cases} 5.63 + 0.68M & \text{for strike} - \text{slip faulting} \\ 11.25 - 0.2M & \text{for non} - \text{strike} - \text{slip faulting} \\ 7.08 + 0.61M & \text{for general (unspecified) faulting} \end{cases} \tag{3.5}$$

To calculate the fault width, Wells and Coppersmith (1994)'s empirical relationship between fault width and M_w given below is utilized. Also, events with unspecified faulting are calculated using the relationship for all types of faults.

$$W = \begin{cases} 10^{-0.76+0.27M_w} & \text{for strike} - \text{slip events} \\ 10^{-1.61+0.41M_w} & \text{for reverse events} \\ 10^{-1.14+0.35M_w} & \text{for normal events} \\ 10^{-1.01+0.32M_w} & \text{for all faults} \end{cases} \tag{3.6}$$

The dip angle is determined according to Ancheta et al. (2014). Generic dip angle values corresponding to each fault type are assigned. The dip angle for reverse and normal events are assumed to be 40° and 55°, respectively. Strike-slip and unspecified faulting events the dip angle of 90°is used.

1530 of 2977 recordings lacked Joyner-Boore distance (R_{JB}) and rupture distance (R_{rup}). Most of this data consists of small-magnitude events; thus, both distance parameters are assumed to be equal to the epicentral distance since the epicentral distance is available for all recordings.

Figure 3.6 illustrates the M_w of ground motion records and the R_{rup} distribution of the recordings. Because of the sensitivity of the recording stations, there are visible censoring issues. For instance, earthquakes with M_w>4.0 are not recorded if the rupture distance is larger than 100 km (R_{rup}>100 km). Similarly, earthquakes with

an M_w smaller than 4.5 and 5.0 are also not recorded if the rupture distance is larger than 200 (R_{rup}>200 km) and 250 km (R_{rup}>250 km), respectively. In terms of R_{rup}, approximately 73% of the dataset is between 10 and 100 km, having the highest number of recordings in this particular interval. Nearly 10% of the ground motions are considered near field (R_{rup}<30 km), and just above 96% of near field events have M_w between 3 and 4.5. In terms of M_w, almost 70% of ground motion data are between M_w=3-4.5, being the dominating magnitude range. On the other hand, over 16% of recordings are considered moderate-to-large magnitude earthquakes (M_w>5), and nearly 75% of recordings from moderate-to-large magnitude earthquakes (M_w>5) have rupture distances larger than 100 km (R_{rup}>100 km).

Figure 3.7 shows information about the distribution of the M_w of the ground motion records and V_{S30} of the stations. The distribution of recordings is heavily accumulated on sites with a V_{S30} smaller than 1000 m/s with approximately 90% of the recordings lying in this interval. The distribution of M_w is also significantly dense for M_w<5.5 with over 95% of them lying in this interval. Nevertheless, events with larger magnitudes (M_w>5.5) and sites with V_{S30}>1000 m/s are also present.

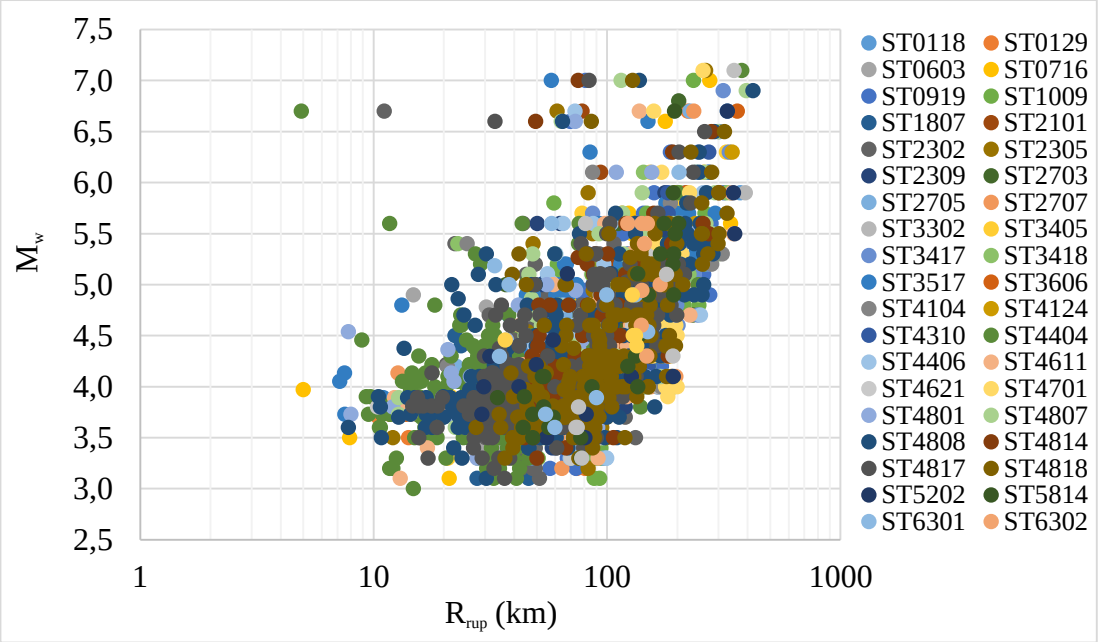

Figure 3.6. The distribution of the M_w and R_{rup} of the recordings in the dataset

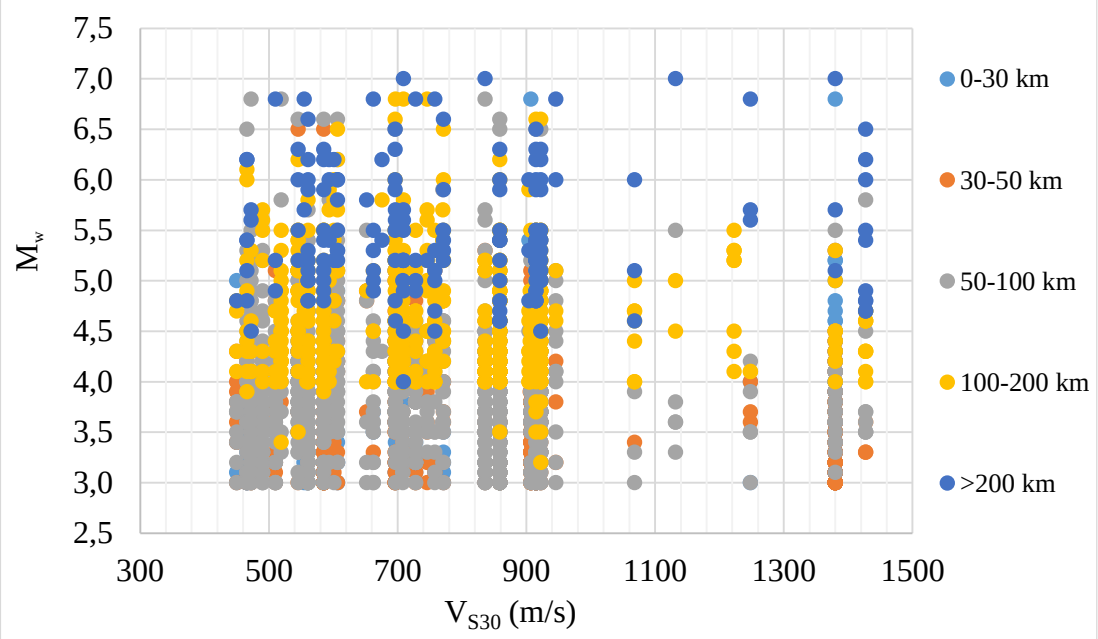

Figure 3.7. The distribution of V_{S30} and M_w of the recordings in the dataset

Table 3.3 shows site information of 40 stations selected for the analysis. It also shows the number of input motions in each station after eliminating the bad-quality ground motion recordings. The table includes the time-based average of V_S profile to 30 m (V_{S30}), the depth of measurement (V_S of the deepest layer), and V_S at the surface ($V_{SSurface}$). Besides, the depth of the bedrock horizon and corresponding V_S (V_{SRock}) are also given in Table 3.3. Each station is modeled to deconvolve (backward analysis) recordings to a particular depth to create a dataset at the engineering bedrock (equivalent outcropping rock). The layer below this particular depth represents the hard rock site conditions in this study, and V_{SRock} represents V_S of the hard rock layer. Every layer above this hard rock layer is considered to be modeled as soil.

Table 3.3. Information about 40 candidate stations

Station ID	V_S Profile Used	Number of input motion	V_{S30} (m/s)	$V_{SSurface}$ (m/s)	V_{SRock} (m/s)	V_{SRock} Depth (m)	V_S of Max Depth (m/s)	Max Depth (m)
0118	MASW	19	946	654	1558	20.35	1994	33.07
0129	COMBINED	30	662	680	1030	62.50	1920	313.00
0603	MASW	25	669	663	1051	33.65	1051	43.78
0716	COMBINED	41	771	650	1770	76.00	4050	355.00
0919	COMBINED	319	856	800	1480	110.00	3040	190.00
1009	MASW	162	562	351	1088	27.20	1088	32.00
1807	COMBINED	33	559	390	1300	66.60	2130	123.00
2101	MASW	32	519	376	1090	41.29	1760	67.12
2302	MASW	138	907	749	1474	24.33	1750	41.65
2305	REMI	127	836	923	1480	50.67	3377	145.15
2309	COMBINED	71	490	480	1000	71.50	1515	116.00
2703	MASW	36	758	635	1341	32.79	1341	42.64
2705	COMBINED	74	728	720	1440	79.50	2280	194.00
2707	REMI	60	510	516	1133	77.20	1133	96.50
3302	REMI	14	1068	1168	2183	69.17	5212	271.82
3405	REMI	22	594	583	1489	99.87	3267	286.11
3417	REMI	32	1427	1493	2037	67.41	3532	377.07
3418	REMI	14	904	742	1743	89.61	3609	352.17
3517	COMBINED	78	606	740	1240	98.50	1550	171.50
3602	MASW	16	555	320	1008	29.25	1008	38.04
4104	MASW	24	769	611	1865	34.00	1865	42.50
4124	COMBINED	4	673	640	1220	81.00	2080	277.00
4310	COMBINED	19	599	560	1020	54.00	1730	81.70
4404	MASW	237	1380	1362	1581	26.31	2446	60.30
4406	REMI	110	472	436	1291	82.08	1291	102.60
4611	COMBINED	71	698	725	1125	55.10	1132	124.20
4621	COMBINED	49	710	725	1150	72.20	1470	117.36
4701	MASW	42	709	409	1432	22.31	1432	27.89
4801	MASW	69	1024	1025	1878	32.60	3301	69.80
4807	MASW	80	697	451	1422	29.10	1422	32.00
4808	COMBINED	306	904	865	1680	85.00	3750	243.00
4814	COMBINED	98	553	600	1530	59.00	2090	254.20
4817	COMBINED	245	579	600	1320	86.00	2150	228.00
4818	COMBINED	205	908	760	1950	41.50	5660	164.00
5202	COMBINED	15	1247	1360	1960	44.30	2895	215.60
5814	COMBINED	28	743	810	1760	114.50	1980	259.00
6301	MASW	11	652	601	1123	34.75	1123	45.19
6302	COMBINED	8	1216	1250	2080	101.36	4150	290.37
6303	COMBINED	8	1133	1200	2030	67.50	2100	102.80
6601	MASW	5	906	777	1618	32.02	1618	41.64

The determination of the depth of base rock is another important parameter that holds great uncertainty. To represent hard rock site conditions, V_S values of base rock are aimed at between 1000 m/s and 3000 m/s. Figure 3.8 shows the determination of base rock and simplified soil profile for ST0716. The selected V_S profile of ST0716 is the combined profile. Due to the uncertainties that would increase while performing 1-D deconvolution analysis with deeper soil profiles, base rock is determined to be at 76 meters with a V_S of 1770 m/s for ST0716.

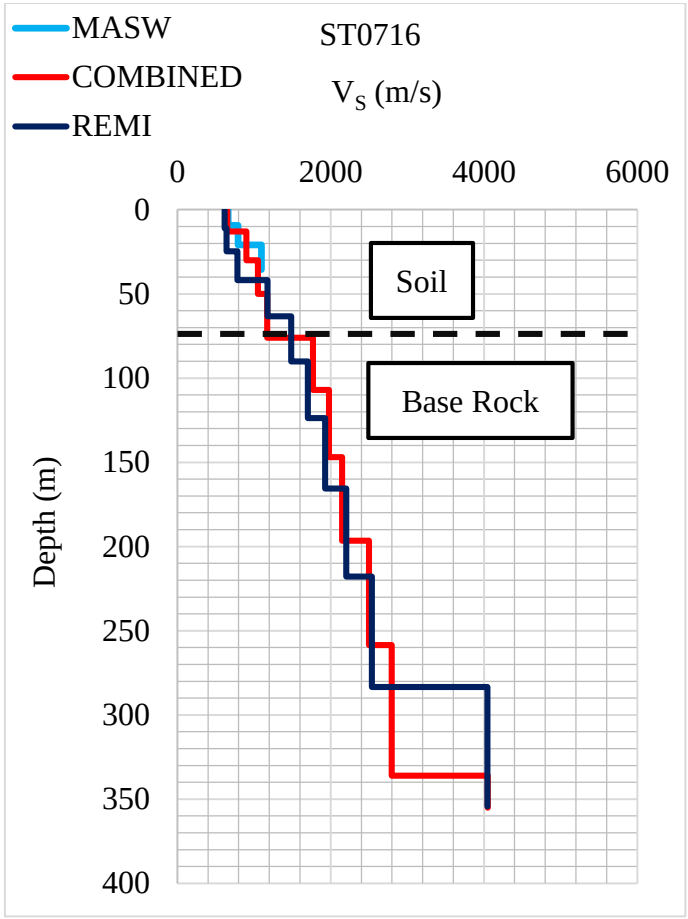

Figure 3.8. V_S profiles of station ST0716

3.4 Transfer Functions

The transfer function is the proportion between surface and bedrock Fourier amplitude spectra (FAS), and it is used to illustrate the soil amplification effects in the frequency domain. To show the linear behavior of 40 simplified soil profiles, empirical transfer functions (ETFs) are generated by performing 1-D equivalent linear ground response analyses (GRA) in DEEPSOIL (Hashash et. al., 2017), and they are compared with the surface-bedrock theoretical transfer functions (TTFs)

computed in DEEPSOIL (Hashash et. al., 2017). To obtain TTFs, linear analyses are performed in the frequency domain.

For performing these analyses, rock motions are selected from the database of The Pacific Earthquake Engineering Research Center (PEER) Next Generation Attenuation (NGA)-West2 project (Ancheta et al., 2014, Bozorgnia et al., 2014).

For the selection of rock motions, the following criteria are used:

- Include all fault types,
- Include recordings with M_w=6.5-8.0 to avoid small ground-shaking levels with a possible linear behavior
- Include recordings with R_{JB}=0-50 km to avoid the large-distance attenuation effects for ground motions in short periods,
- Include recordings with V_{S30}=800-1500 m/s to avoid the soil amplification effects,
- Exclude pulse-like records.

15 ground motions are selected based on this selection criteria. Since only horizontal components are used, there are a total of 30 ground motion recordings. The elastic acceleration response spectra with 5% damping of these 30 ground motion recordings are plotted to determine a dataset. The recordings that lie furthest from the average response spectra of these 30 records are removed consecutively, and eight rock motion recordings relatively closer to the average response spectra are selected as the input motion dataset. The elastic acceleration response spectra with 5% damping of these eight rock motions are illustrated in Figure 3.9, and the information about these rock motions is given in Table 3.4.

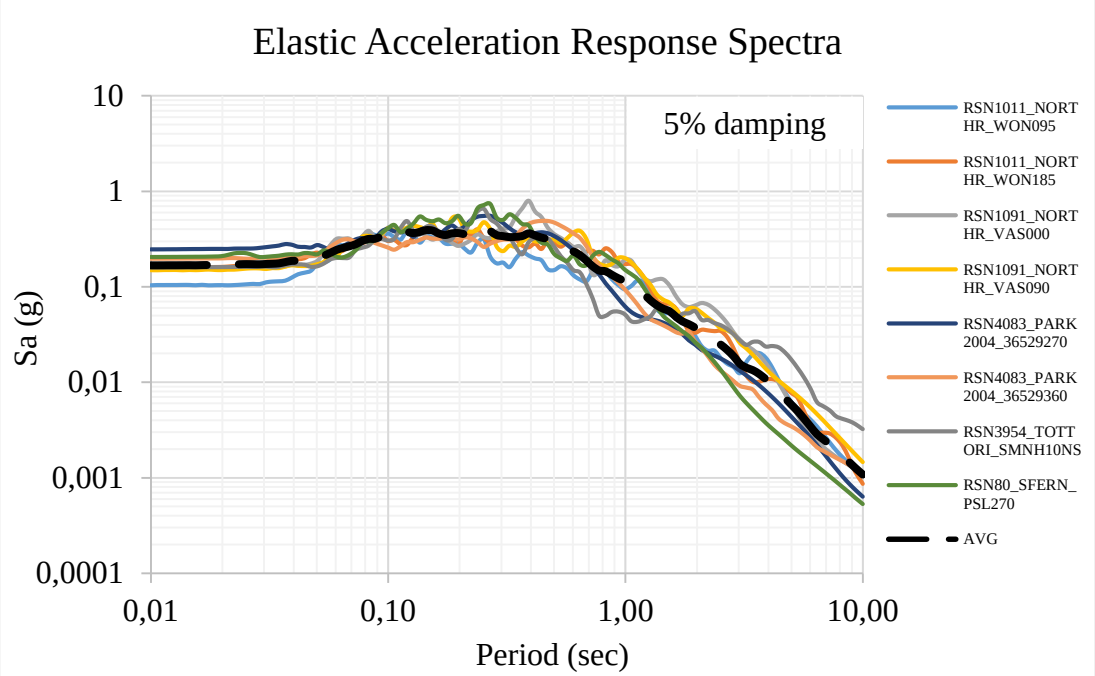

Figure 3.9. Elastic acceleration response spectra of selected 8 rock motions with 5% damping

Table 3.4. Information about selected 8 rock motions

Result ID	Record Seq. #	Event	Year	Station	Magnitude	Fault Mechanism	Rjb(km)	Rrup(km)	V_{S30}(m/s)	Component
1	80	San Fernando	1971	Pasadena - Old Seismo Lab	6.61	Reverse	21.5	21.5	969.07	SFERN_PSL270
2	1011	Northridge-01	1994	LA - Wonderland Ave	6.69	Reverse	15.11	20.29	1222.52	NORTHR_WON095
3	1011	Northridge-01	1994	LA - Wonderland Ave	6.69	Reverse	15.11	20.29	1222.52	NORTHR_WON185
4	1091	Northridge-01	1994	Vasquez Rocks Park	6.69	Reverse	23.1	23.64	996.43	NORTHR_VAS000
5	1091	Northridge-01	1994	Vasquez Rocks Park	6.69	Reverse	23.1	23.64	996.43	NORTHR_VAS090
6	3954	Tottori, Japan	2000	SMNH10	6.61	Strike slip	15.58	15.59	967.27	TOTTORI_SMNH10NS
7	4083	Parkfield-02, CA	2004	PARKFIELD - TURKEY FLAT #1 (0M)	6	Strike slip	4.66	5.29	906.96	PARK2004_36529270
8	5483	Iwate, Japan	2008	AKTH05	6.9	Reverse	37.45	39.41	829.46	PARK2004_36529360

Eight rock motions are used to perform GRA in DEEPSOIL (Hashash et. al., 2017), and the mean of ETFs and TTFs are plotted for each station separately.

TTFs and ETFs for all stations are plotted for response spectra periods of NGA GMMs; thus, there is smoothing in the graphs.

Figure 3.10 shows the comparison of the mean ETF and TTF of the eight rock motions for ST0716. Overall, there is a good fit in the graph with a soil amplification effect around 3.5 Hz which is the natural frequency of the simplified soil profile. There is also a peak at around 10 Hz because of the soil amplification effects with a negligibly small misfit between ETF and TTF. After 20 Hz, there is a slight shift in the shape (the difference might be related to the high-frequency diminution, known as kappa), and it is considered negligible. Therefore, it can be concluded that the behavior of ST0716 is not nonlinear. Similar to ST0716, all 40 profiles are found to have a linear behavior. As a result, selected stations are determined to be suitable for equivalent linear analysis. To review other stations, the reader should refer to Appendix C.

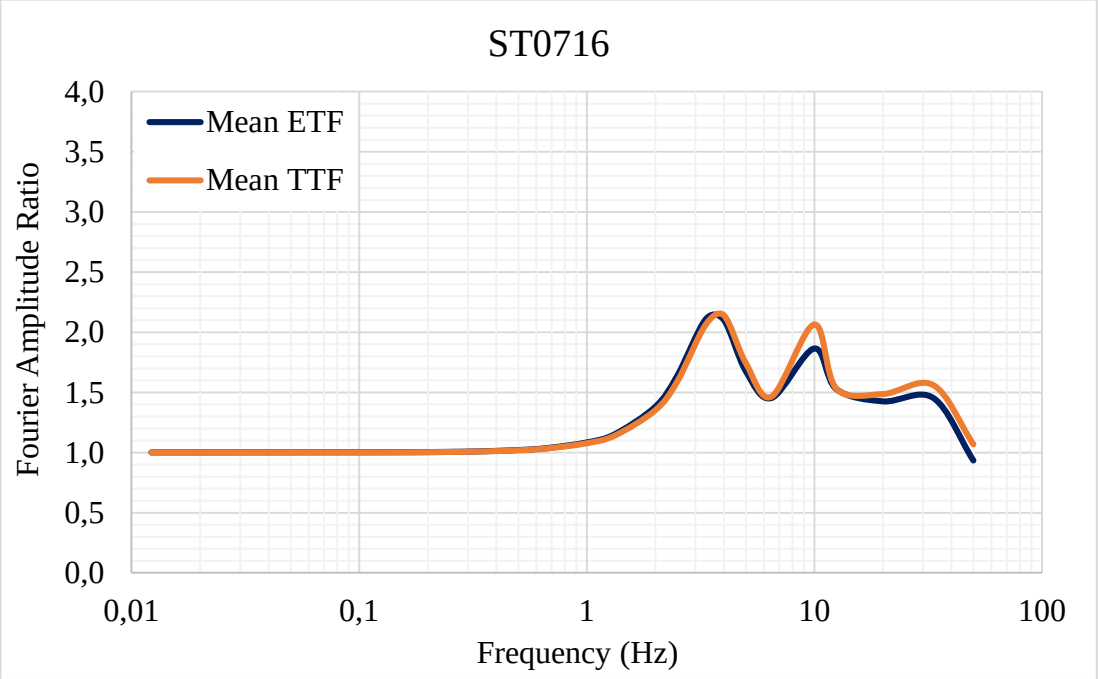

Figure 3.10. Comparison of the mean ETF and TTF for station ST0716

CHAPTER 4

SITE RESPONSE ANALYSES BY DECONVOLUTION AND SITE AMPLIFICATION FACTORS

This chapter presents the details of the methodology used in this study for site response analysis by deconvolution. Then, the site amplification factors obtained from each station are discussed and compared with the median predictions of current site amplification models.

4.1 4.1. Methodology for Deconvolution Analysis

The flowchart for the methodological steps applied for the 1-dimensional (1-D) equivalent-linear site response analysis by deconvolution is presented in Figure 4.1. As shown in the figure, the analyses started with the selection of candidate strong ground motion stations that represent the hard rock site conditions, which is thoroughly discussed in Chapter 3. Please note that 40 out of 1039 AFAD's strong motion stations are selected for this study based on a systematic review of the V_S profiles given in the site characterization reports (see Chapter 3.1 for details). Processed acceleration-time histories of the recordings from each station are retrieved through AFAD's website: 6322 recordings of two orthogonal horizontal components from 40 stations are acquired in total. After the quality control of the recordings (Chapter 3.2), almost half of the recordings were eliminated and 2977 ground motion recordings are used in the deconvolution analysis.

One of the critical tasks in the site response analysis is the modeling of simplified soil profiles. In 1-D equivalent linear site response analysis, a simplified soil profile is characterized by horizontal layers with dynamic (V_S, damping, and shear modulus reduction curves) and mechanical (unit weight) soil parameters (an example is provided in Table 4.1).

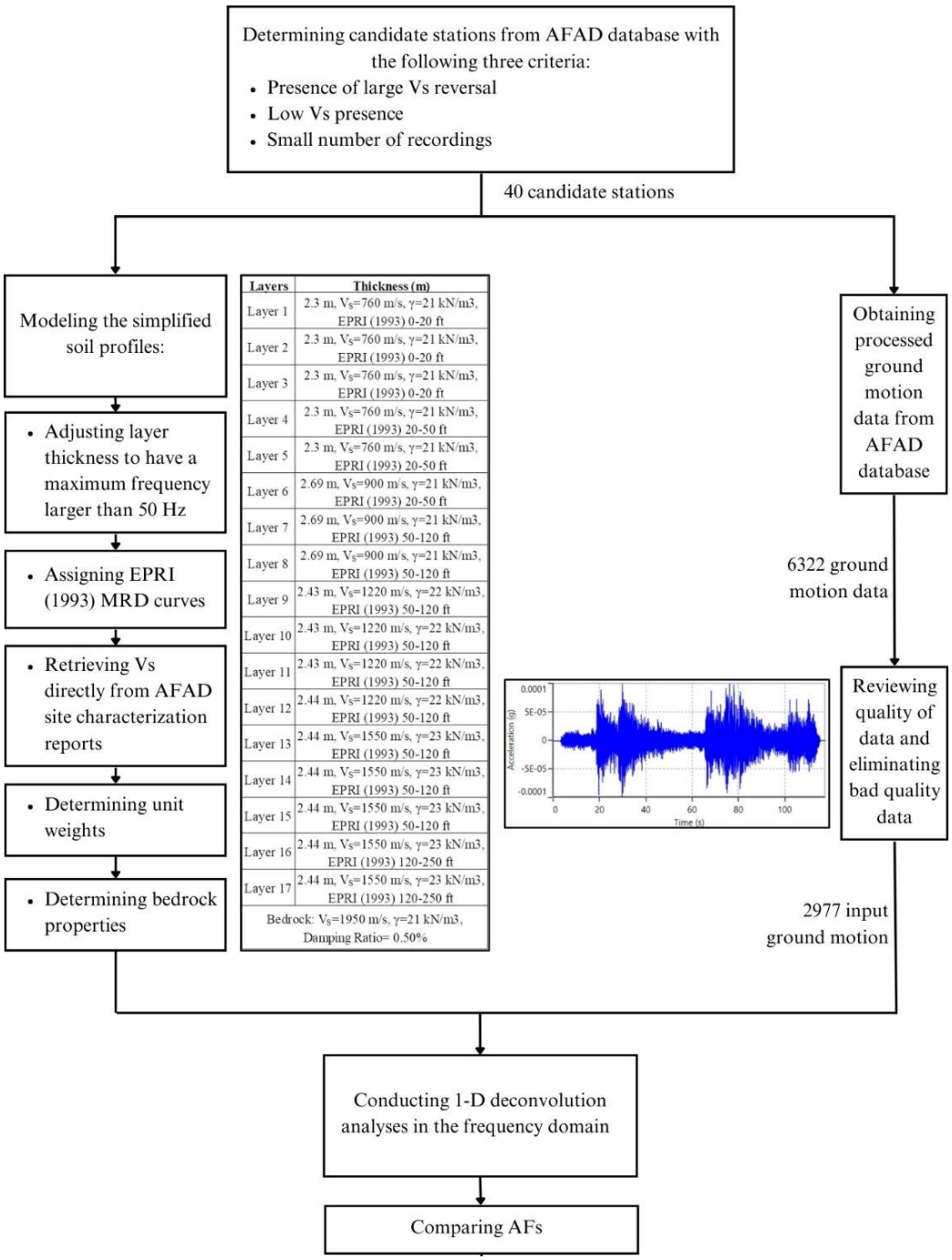

Figure 4.1. Flowchart for the methodological steps applied for the 1-D equivalent-linear site response analysis by deconvolution

The soil layer thicknesses in the simplified profiles are defined as 1.5-3.5 meters to ensure that the maximum frequency of each layer is at least 50 Hz. Also, the difference in maximum cut-off frequency in consecutive layers is monitored to eliminate abrupt changes. Since the site characterization reports provided by AFAD are not uniform, there is a lack of information about the geotechnical parameters of soil layers. To minimize the uncertainties related to the unknown soil parameters, depth-dependent EPRI shear modulus reduction and damping (MRD) curves are preferred (EPRI, 1993) as shown in Figure 4.2.

Table 4.1. An example simplified soil profile (ST4818)

Layers	Depth (m)	Thickness (m)	Vs (m/s)	Modulus Reduction and Damping Curve	Unit Weight (kN/m3)	Maximum Frequency (Hz)
Layer 1	0.00	2.30	760	EPRI (1993) 0-20 ft (0-6.1 m)	21	83
	2.30					
	2.30	2.30			21	83
	4.60					
	4.60	2.30			21	83
	6.90					
	6.90	2.30		EPRI (1993) 20-50 ft (6.1-15.24 m)	21	83
	9.20					
	9.20	2.30			21	83
	11.50					
Layer 2	11.50	2.69	900		21	84
	14.19					
	14.19	2.69		EPRI (1993) 50-120 ft (15.24-36.58 m)	21	84
	16.88					
	16.88	2.69			21	84
	19.57					
Layer 3	19.57	2.43	1220		22	126
	22.00					
	22.00	2.43			22	126
	24.43					
	24.43	2.43			22	126
	26.86					
	26.86	2.44			22	125
	29.30					
Layer 4	29.30	2.44	1550		23	159
	31.74					
	31.74	2.44			23	159
	34.18					
	34.18	2.44			23	159
	36.62					
	36.62	2.44		EPRI (1993) 120-250 ft (36.58-76.2 m)	23	159
	39.06					
	39.06	2.44			23	159
	41.50					

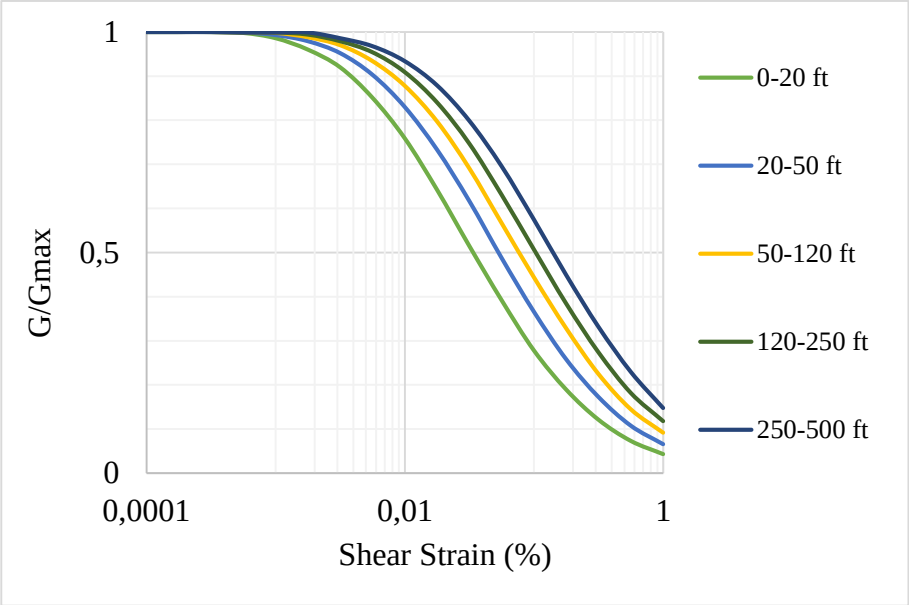

(a)

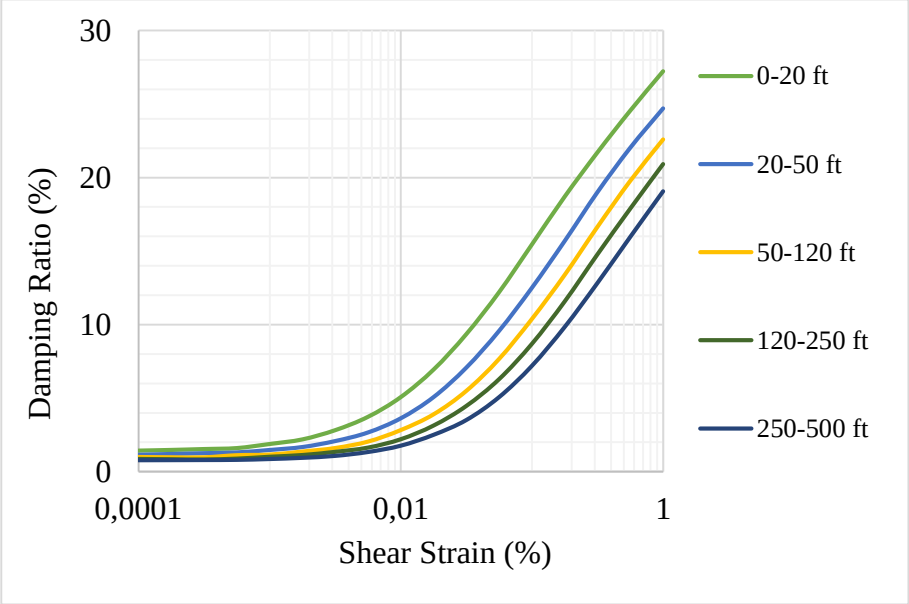

(b)

Figure 4.2. Depth-dependent EPRI (1993)'s (a) shear modulus reduction and (b) damping curves

The V_S values provided in AFAD's site characterization reports are directly used without any modifications. Unit weights are determined by using the site classification of NEHRP (2020) based on the V_S value and the empirical relationship provided by Boore (2016) (given in Table 4.2). The site classification provided by

the NEHRP (2020) offers a more detailed classification and allows us to assign unit weights to smaller V_S intervals; therefore, it is preferred over the classification in the Turkish Building Earthquake Code (TBDY-2018, 2018). Furthermore, Boore (2016) provides an empirical relationship between unit weights and shear wave velocities, and unit weights of each layer are calculated for different V_S intervals. Elastic half-space is used as the engineering bedrock with 0.50% damping and 25 kN/m^3 unit weight.

Table 4.2. NEHRP (2020) site classes and the unit weights proposed by Boore (2016) for each class

Site Class	Interval of Vs (m/s)	Unit Weight (kN/m3)
A	>1500	23
B	914-1500	22
BC	640-914	21
C	442-640	20
CD	305-442	19
D	213-305	19
DE	152-213	18
E	<152	17

1-D deconvolution analyses are conducted in the frequency domain by using ground response analysis software DEEPSOIL (Hashash et. al., 2017). Deconvolution is calculating the ground motion at a specific depth below the level where the ground motions are recorded using the equivalent linear approach (Idriss and Akky, 1979, Kramer, 1996, Markham et al., 2016). Input surface motions are deconvolved through the soil column to depths that represent hard rock site conditions with the parameters defined above. The determination of the depth of the bedrock-soil interface for each soil profile is explained in Chapter 3. The output motions are selected to be equivalent outcrop motions for deconvolution analyses in this study.

4.2 4.2. Estimated Site Amplification Factors

Estimated site amplification factors (AFs) are used to evaluate the results of 1-D equivalent linear deconvolution analyses for each station as shown in Figures 4.3-

4.7. AFs are calculated as the ratio of bedrock and surface response spectra with 5% damping by using the formula given below (Kramer, 1996, Stanko et al., 2019):

$$\mathrm{AF}\ (\mathrm{T}) = \frac{\mathrm{Sa}_{\mathrm{SURFACE}}\ (\mathrm{T})}{\mathrm{Sa}_{\mathrm{BEDROCK}}\ (\mathrm{T})} \tag{4.1}$$

In Figures 4.3 - 4.7, the black lines represent the average of AFs calculated from the full set of recordings in each station and the dotted lines show the median plus 1 and 2 standard deviation values. The orange lines in Figures 4.3 - 4.7 are the median predictions of site amplification models proposed by Stewart et al. (2020, S20) and Hashash et al. (2020, H20). The geometric average PGA_{rock} of recordings computed from deconvolution analysis is calculated for each station and utilized in the S20 and H20 site amplification models for calculating the median estimates.

There are 24 stiff soil stations with V_{S30}<760 m/s and half of them have AF difference in terms of the location of the peak, the amplitude of the peak and the number of peaks from the S20 & H20 site models. Nevertheless, only 30% of the rock site stations (V_{S30}>760 m/s) do not match with the site models of S20 & H20. Therefore, the stations with larger V_{S30} (V_{S30}>760 m/s) have a better fit with S20 & H20 site models. Also, having a V_S reversal in V_S profiles tends to increase the number of peaks, decreasing the level of match with the S20 & H20 models. However, the V_S profiles used to generate estimated AFs are the real profiles with field measurements, whereas the site model is developed through stochastic simulations with virtually generated V_S profiles with smooth V_S increments. Therefore, the differences between estimated AFs and the site model can be considered well since estimated AFs still lie within the median±sigma to median±2sigma of site model.

AFs of ST4701 and ST4801 show a significant fit with the S20 & H20 site models. The V_{S30} and V_{SRock} difference of ST4701 and ST4801 is around 700 m/s and 1200 m/s, respectively. The locations and the amplitudes of AFs are in line with the model for both stations; however, after 0.2 seconds, ST4801 is significant lie above the site model. Since larger V_S difference between soil and bedrock increases the AFs in 1-D site response analyses, the AF of ST4801 is significantly larger than that of ST4701 after 0.2 seconds.

AFs of ST0716, ST2707, ST3418, ST3517, ST4124, ST4310, and ST4611 peak at the same location as the S20 & H20 models; however, the amplitude of the peaks is significantly different. AFs of all these stations have two or more peaks because there are slight V_S reversals in V_S profiles of stations; however, their first peak are at the same location as the S20 & H20 models. The presence of other peaks decreases the level of fit with the S20 & H20 models around the periods of peaks; nonetheless, the general fit between the estimated AFs of these stations and the site model is considered great since the site model is not based on real V_S profiles and the AFs still within the median±sigma range of the site model.

AFs of ST2302, ST2703, ST4104, ST4807, ST4818, and ST6601 have a single peak at the same period as the S20 & H20 models, but estimated AFs have slightly larger amplitudes. Also, all stations have almost a perfect fit with the site models after the periods of 0.1 to 0.2 seconds, where the AFs peak. In addition, V_{S30} of these stations are in the range of 700 m/s to 900 m/s, and V_{SRock} is between 1300 m/s and 2000 m/s. The difference between V_{S30} and V_{SRock} of each station are pretty similar; hence, the AF amplitudes of stations is quite similar to each other.

For ST2101, ST4406, ST4808, and ST6302, there are two AF peaks. The location of the first AF peak is similar to the S20 & H20 site models for all stations; however, there is also a second peak in estimated AFs. This decreases the level of fit with the site model. Also, the AFs lie above the S20 & H20 site models between 0.5 and 0.7 seconds. For ST4808 and ST6302, the fit with the site model after 0.7 second is considerable, whereas the AFs of the other two stations lie significantly above the site models. This may have an influence on the AFs at larger periods as both ST4808 and ST6302 have approximately 600 m/s larger V_{S30} and V_{SRock} values compared to the other two, medianing that they are much stiffer than the other two stations.

ST0118, ST4404, and ST3602 have peaks in different locations with respect to S20 & H20 models. The amplitudes of ST0118 and ST4404 are the same as the site model; however, ST3602 has an additional AF peak. This may be due to the larger V_S reversal in V_S profile of ST3602. Although all three stations have a V_S reversal, ST3602 have a significantly larger reversal than that of ST0118 and ST4404. Another difference between the estimated AFs of three profiles is the fit at larger

periods. The AF of ST3602 is significantly larger than the other two stations, and this decreases the level of fit with the site model compared to the other two. This is due to relatively soft soil layer presence and lower V_{SRock} of ST3602 since it affects the 1-D site response analyses significantly. V_{S30} of ST0118 and ST4404 is approximately 1170 m/s, and ST3602 is a soil site with a V_{S30} of 555 m/s. V_{SRock} of the former two is about 1500 m/s, being almost 500 m/s larger than that of ST3602.

The location and the amplitude of the peaks of ST0603, ST2305, ST2705, ST3417, ST4621, ST5202, ST6301, ST6303 do not match to S20 & H20 models. However, they are still within the median±2sigma range, which is considered to be quite great. ST0603 has the smallest V_{S30} and V_{SRock} of this group with 450 m/s and around 1050 m/s, respectively, and it has the largest AFs in this group. Therefore, it may be the reason why it lies quite above the site model, and the fit with the site model is lower than the other stations. The rest of the stations demonstrate a relatively better match after the period of their peaks.

ST0129, ST0919, ST1009, ST1807, ST2309, ST3302, ST3405, ST4814, ST4817, and ST5814 are similar to the previous group. However, these stations have an additional AF peak, which makes them less in line with the site models. On the other hand, ST0129, ST0919, ST3302, ST4817, and ST5814 have a match after the last peak of around 1-3 seconds.

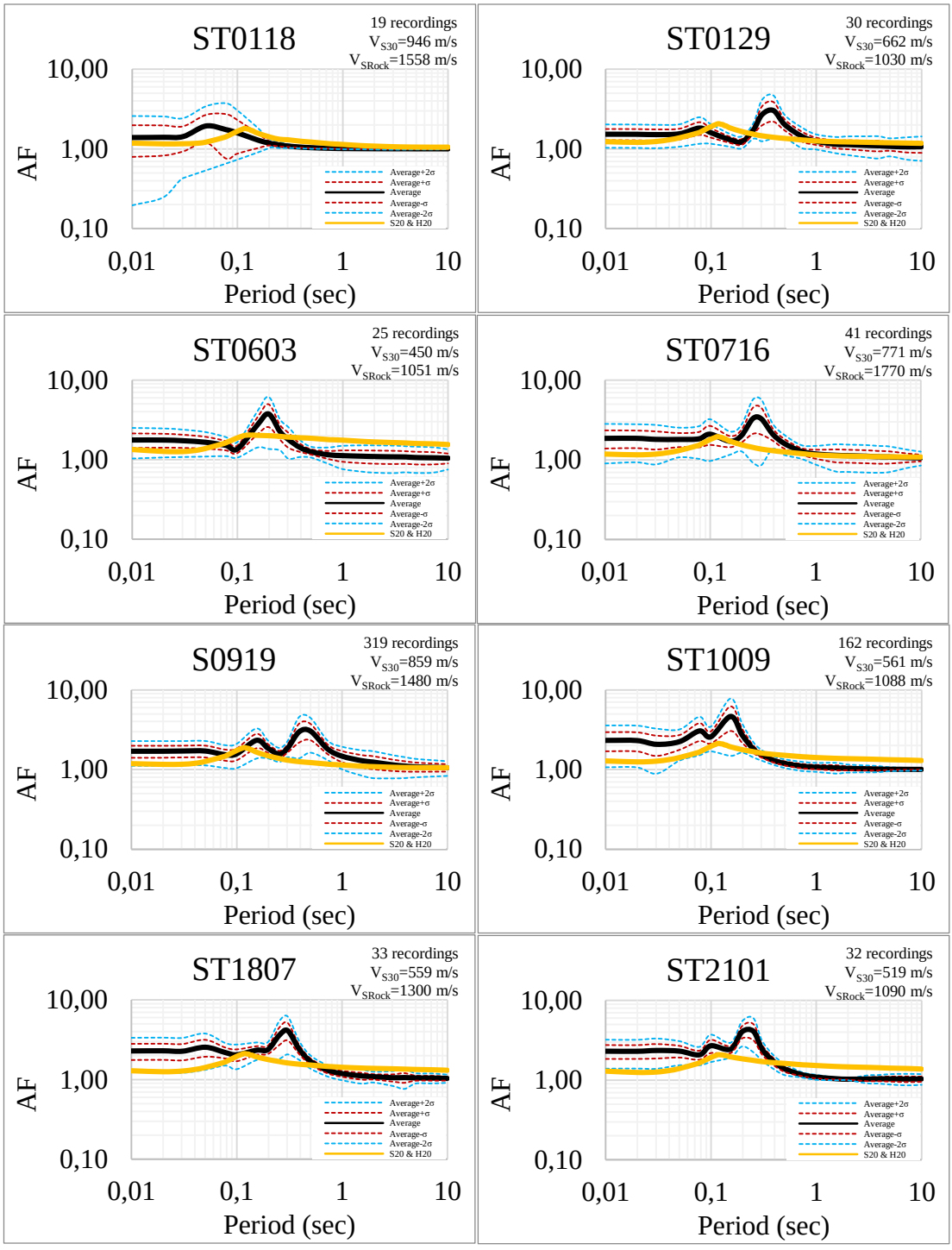

Figure 4.3. Comparison of AFs and Stewart et al. (2020) & Hashash et al. (2020)'s site model for candidate stations ST0118, ST0129, ST0603, ST0716, ST0919, ST1009, ST1807, ST2101

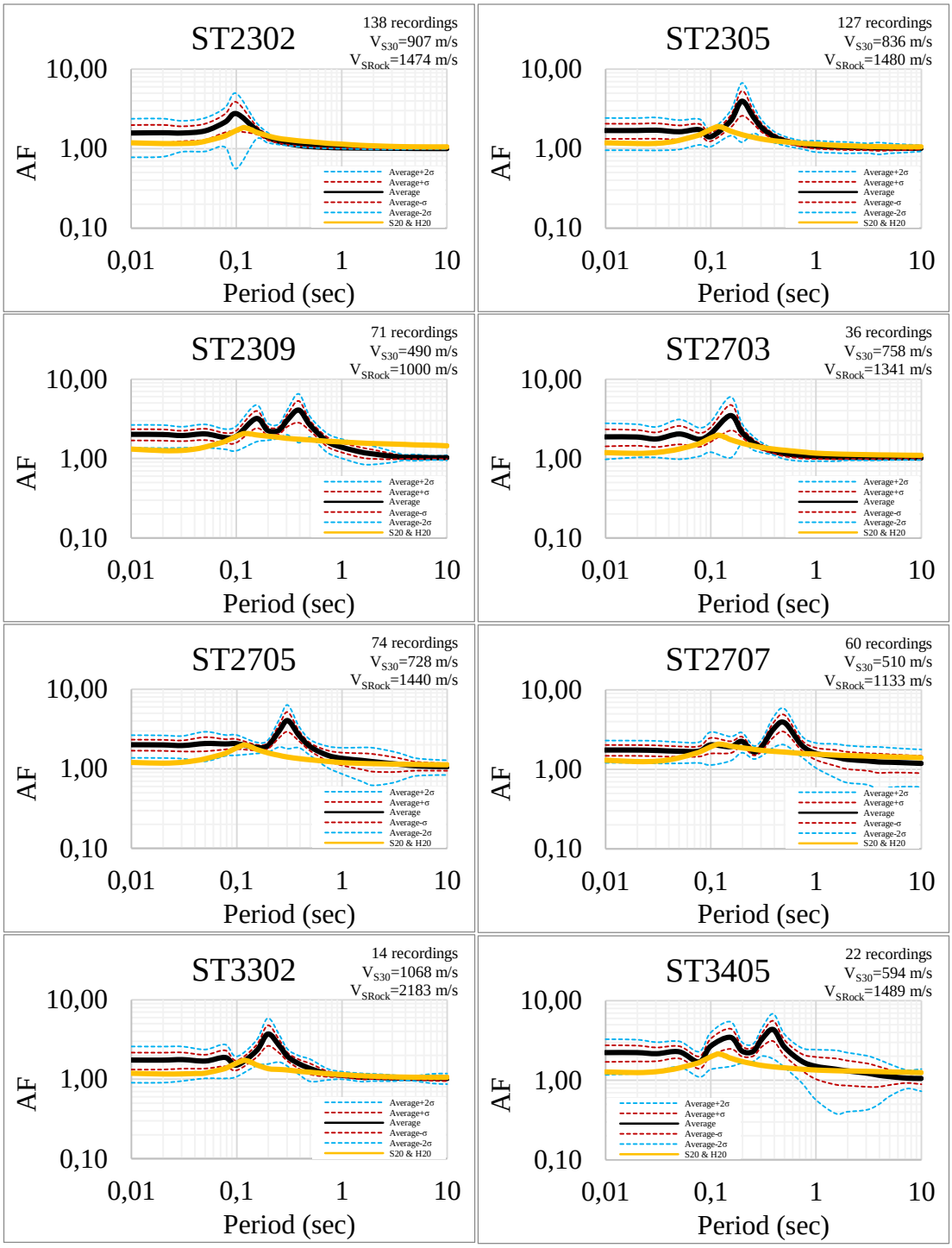

Figure 4.4. Comparison of AFs and Stewart et al. (2020) & Hashash et al. (2020)'s site model for candidate stations ST2302, ST2305, ST2309, ST2703, ST2705, ST2707, ST3302, ST3405

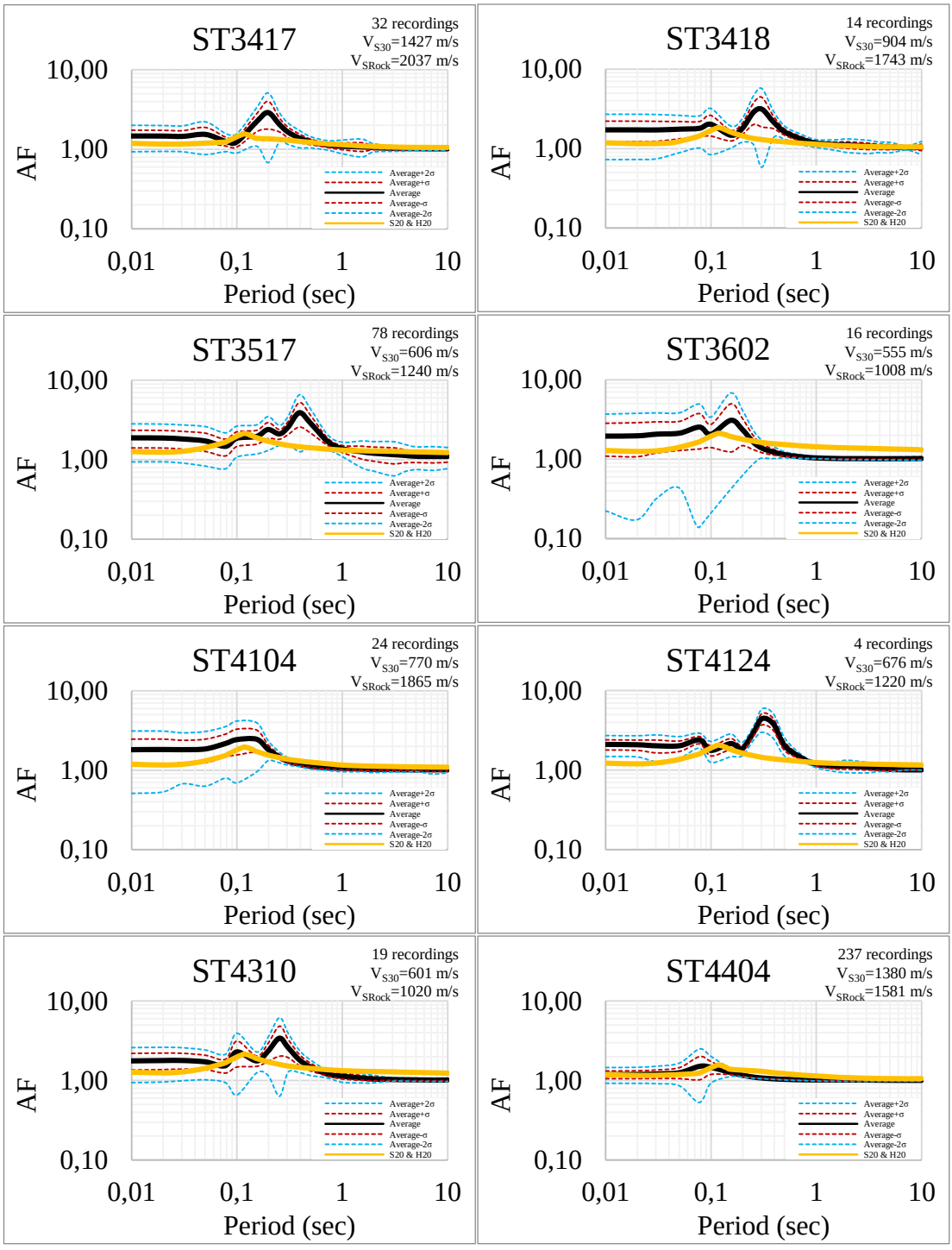

Figure 4.5. Comparison of AFs and Stewart et al. (2020) & Hashash et al. (2020)'s site model for candidate stations ST3417, ST3418, ST3517, ST3602, ST4104, ST4124, ST4310, ST4404

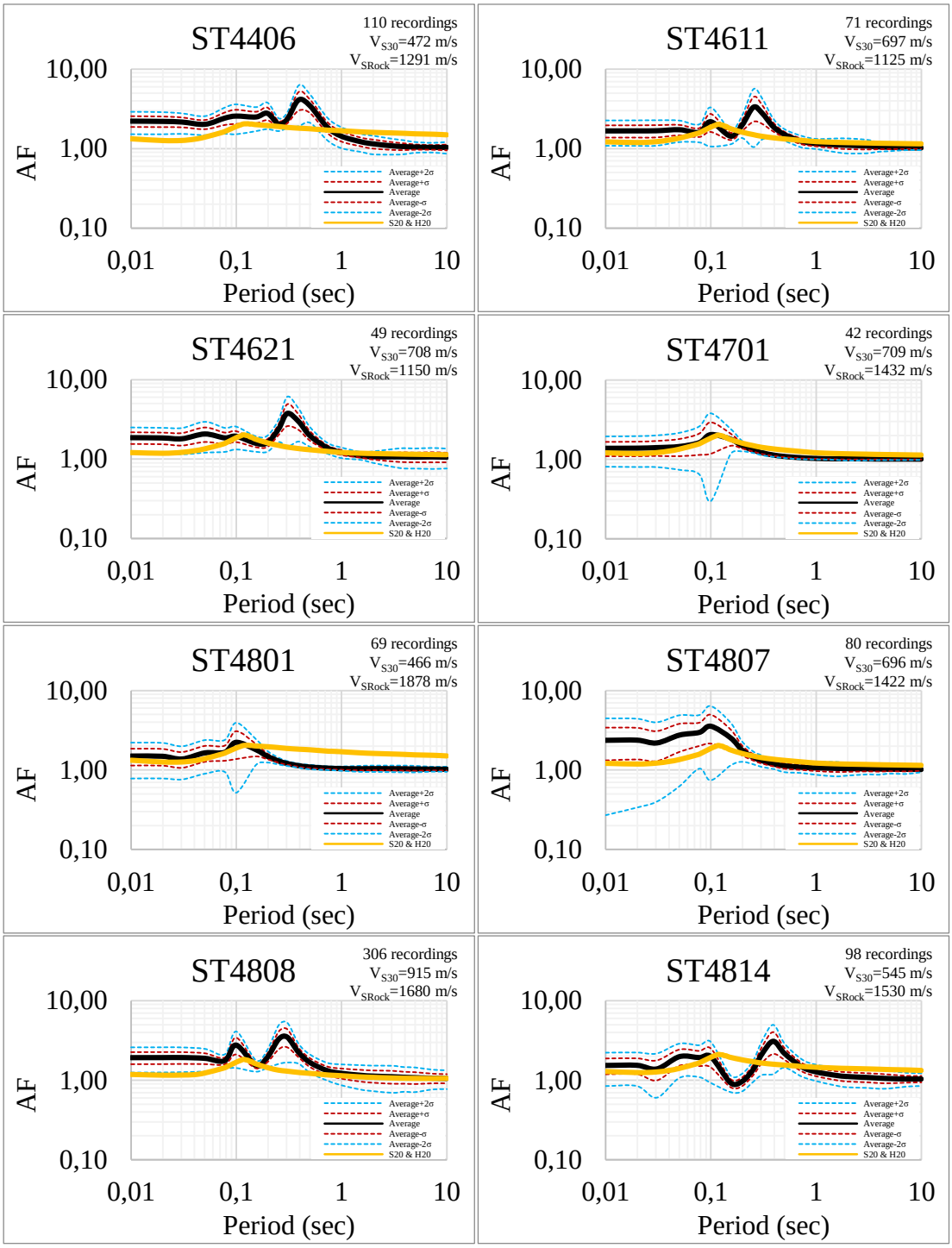

Figure 4.6. Comparison of AFs and Stewart et al. (2020) & Hashash et al. (2020)'s site model for candidate stations ST4406, ST4611, ST4621, ST4701, ST4801, ST4807, ST4808, ST4814

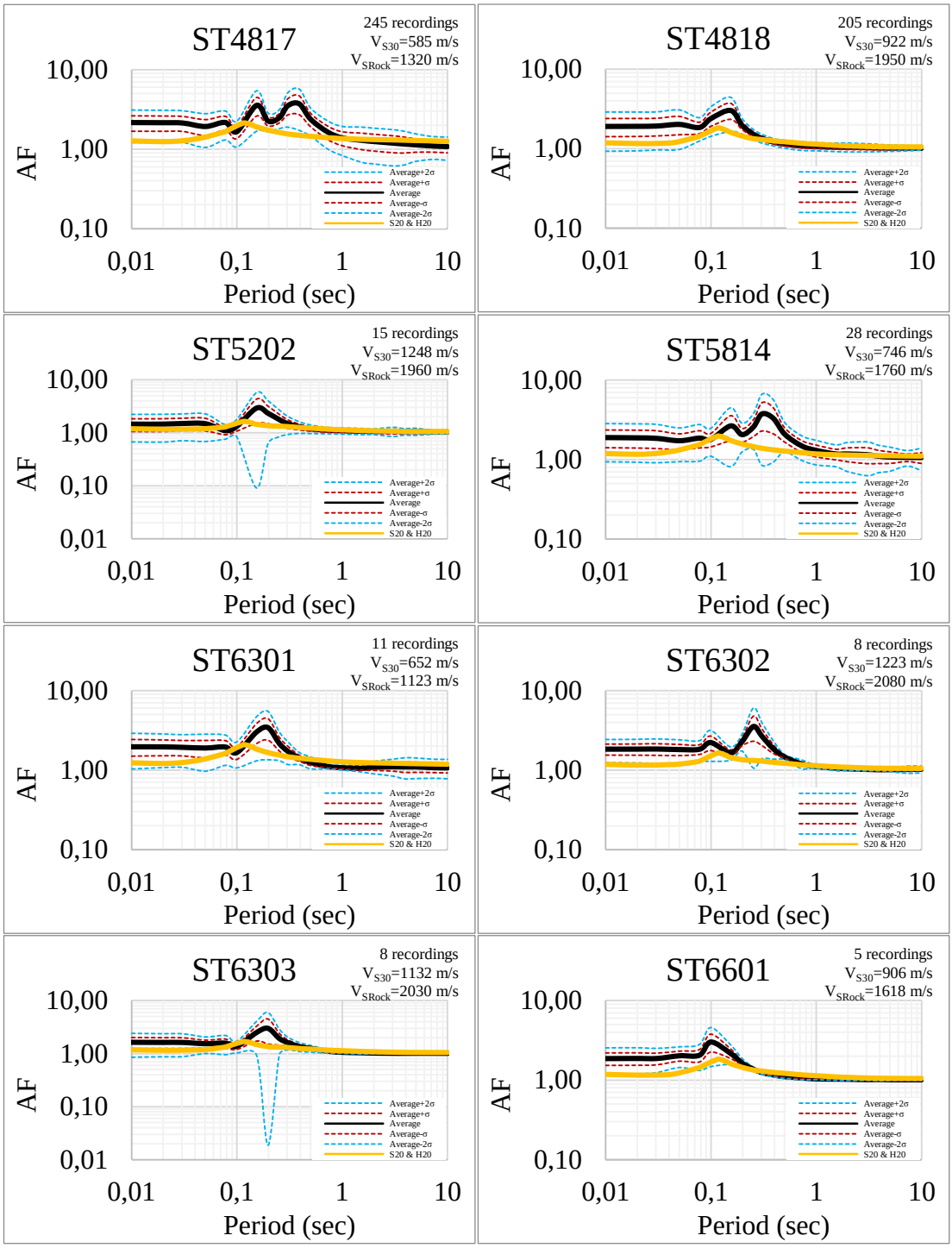

Figure 4.7. Comparison of AFs and Stewart et al. (2020) & Hashash et al. (2020)'s site model for candidate stations ST4817, ST4818, ST5202, ST5814, ST6301, ST6302, ST6303, ST6601

CHAPTER 5

ROCK GROUND MOTION MODEL

The PSA_{rock} values are obtained from the methodology with the use of the ground motion dataset compiled in the previous chapters. The geometric mean of two horizontal components of PSA_{rock} values is taken to analyze the performance of the rock GMM of Laurendeau et al. (2018) (hereafter L18). The fundamental reason that L18 is chosen as the candidate model in our study is that it proposes a quite simple functional form. They obtained a geometrical mean of horizontal components through the random-effects method (Abrahamson & Silva, 1992), and L18 functional form is given by:

$$\ln\left(\mathrm{SA(T)}\right)_{es} = a_1(\mathrm{T}) + a_2(\mathrm{T})M_W + a_3(\mathrm{T})M^2{}_W + b_1(\mathrm{T})R_{RUP} - \ln(R_{RUP}) + c_1(\mathrm{T})\ln(V_S/1000) + \delta B_e(\mathrm{T}) + \delta W_{es}(\mathrm{T}) \quad (5.1)$$

where SA(T) is the spectral acceleration for the oscillator period T. δW_{es} and δB_e stand for the within-event and between-event variability terms, respectively. a_1, a_2, a_3, b_1, c_1 are the coefficients determined by regression analysis. R_{RUP} is the rupture distance between the site and the fault in km, and M_w is the moment magnitude. V_S is taken differently depending on the dataset type. In this sense, L18 developed this GMM within the range of 500-1350 m/s and 1000-3000 m/s for V_{S30} and V_S, respectively.

As regards the input ground motion dataset for analyzing the performance of L18, the selection of the proper dataset is vital since there are 4 different virtual rock motion datasets used in L18. Japanese KiK-net database is utilized in this study, and they are classified according to the level where the sensors are located as described below:

- The first set of ground motions is named as DH_{cor}, which is the virtual data determined from downhole data recorded at a particular depth. This within-motion dataset is then corrected to remove the depth effects, which are then turned into an equivalent outcropping motion dataset.

- The second ground motion dataset is termed as $SURF_{cor}$. It is the other virtual type of ground motion, which is recorded at the ground level. The site correction is applied to these motions by deconvolving through generic soil profiles derived from V_{S30} (Cotton et al., 2006, Boore and Joyner, 1997) utilizing a 1-D reflectivity approach (Kenneth, 1974). After applying this method, rock motions are obtained.
- The other two sets of ground motion datasets are the actual recordings without any corrections. They are used for the comparison of virtual rock motions. These two datasets are classified into two categories as DATA_surf and DATA_dh, which are surface recordings and downhole recordings in turn.

The GMM coefficients and the type of V_S to be used in the estimations also vary depending on the dataset type. As regards the coefficients, there are four different coefficients given for the datasets of DH_{cor}, $SURF_{cor}$, the combination of $SURF_{cor}$ and DATA_surf, and the combination of DH_{cor} and DATA_surf. Our input dataset is determined to be similar to $SURF_{cor}$ since both $SURF_{cor}$ and our input ground motion dataset are surface recordings and deconvolved by 1-D ground response analyses. Therefore, the coefficients suggested to be used for $SURF_{cor}$ are preferred. In addition, there are two parameters to show V_S dependency in L18: V_{S30}, and V_S (which is correlated to the V_{SROCK} in our study). V_{S30} is suggested to be used for types of datasets similar to DATA_surf, and all other types of datasets are suggested to be used with V_S. As a result, in the proposed functional form, V_S is considered to be V_{SROCK} for our study.

Figure 5.1 shows the locations where V_{S30} and V_{SROCK} are defined. V_{S30} is defined as the average V_S at the uppermost 30 meters of the soil column from the ground level, while V_{SROCK} corresponds to V_S of the first layer below the soil and rock interface in our study. The determination of the soil and rock interface is explained in detail in Chapter 3. However, the V_{SROCK} definition is given here since it is utilized in the residual analysis to review the performance of L18 as a base model for the Turkish ground motion database. V_S average of rock layers and V_S of the first rock layer did not differ considerably, and the depth below the soil and rock interface differ

significantly for different soil profiles, the V_{SROCK} is determined to be the V_S of the first rock layer for consistency.

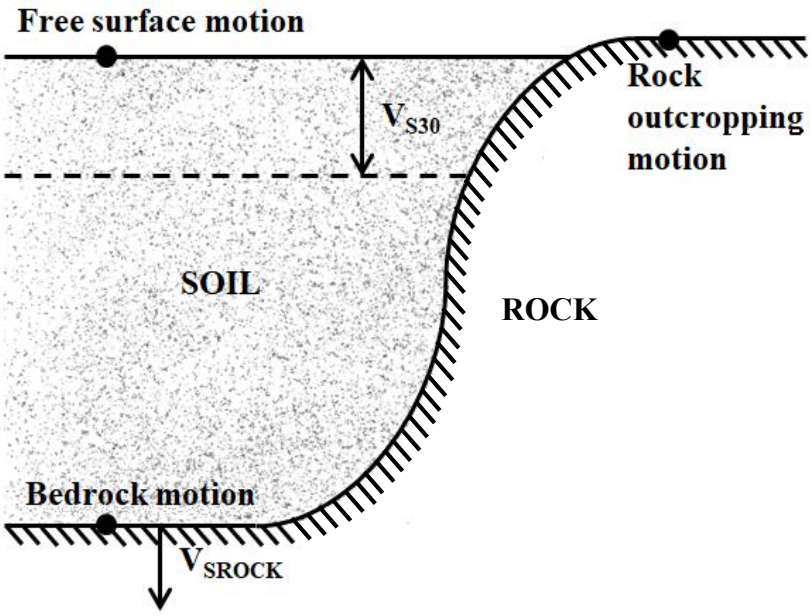

Figure 5.1. The locations of V_{S30} and V_{SROCK} and corresponding ground motion locations

The average of four NGA-West2 GMMs is plotted to be compared with the estimations of the L18 model. The selected candidate GMMs are Abrahamson et al. (2014), Boore et al. (2014), Campbell and Bozorgnia (2014), and Chiou and Youngs (2014) (hereafter, ASK14, BSSA14, CB14, CY14, respectively). The same procedure to determine the event parameters, station parameters, and recording parameters followed in Chapter 3 is applied for NGA-West2 GMMs. Figure 5.2 - Figure 5.4 show the median comparison of the elastic acceleration response spectra of L18, ASK14, CY14, and the average of four NGA-West2 GMMs. The median spectra are plotted for an M_w=6.5 strike-slip earthquake at an R_{RUP}=30 km for V_{S30}=1100 m/s, 1500 m/s, and 2000 m/s in Figure 5.2 - Figure 5.4, respectively. Figure 5.2 shows that L18 is less smooth, with estimates significantly higher than the other models for V_{S30}=1100 m/s, especially at around the oscillator period of 0.15 s. Despite the overprediction of L18, there is still a similarity of L18 with other plots. The similarity between CY14 and L18 increases in Figure 5.3 and Figure 5.4 as the

median spectra of the L18 model shift downward for V_{S30}=1500 m/s and V_{S30}=2000 m/s, respectively. However, the ASK14 median spectrum decreases as V_{S30} increases, which underpredicts the most among all models. In Figure 5.4, the L18 model decreases for V_{S30}=2000 m/s as opposed to the other models; therefore, CY14 and L18 estimations are quite similar, especially at the intermediate and long periods (T>0.2 s). The average of four GMMs, ASK14, and CY14 stay almost the same between V_{S30}=1500 m/s and V_{S30}=2000 m/s, indicating that estimations of four candidate GMMs above 1500 m/s saturate. In general, L18 overpredicts for V_{S30} below 1500 m/s compared to NGA-West2 GMMs, specifically at short and intermediate periods. However, there is still a considerable agreement between L18 and the NGA-West2 GMMs in the median prediction of rock sites (V_{S30}>1000 m/s) at long periods.

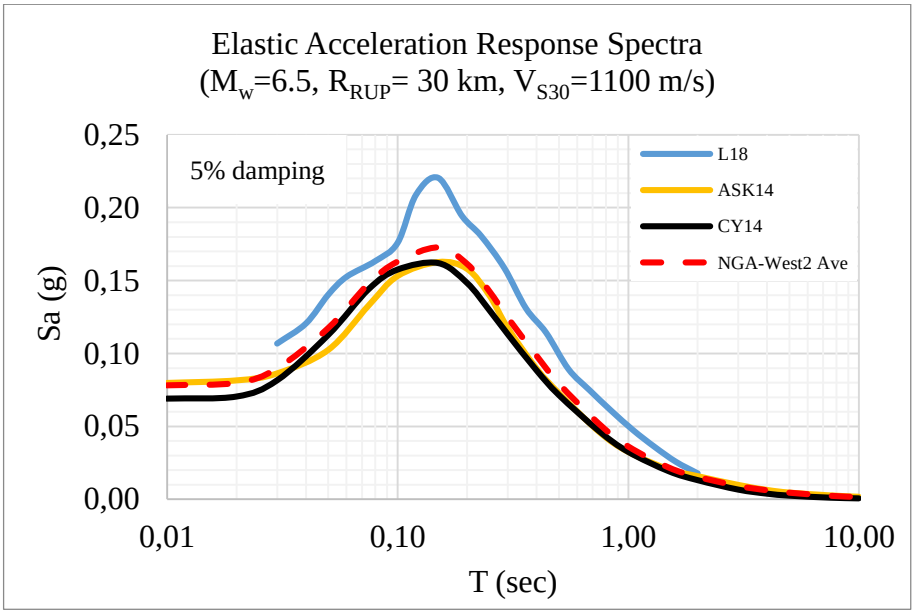

Figure 5.2. Median comparison of response spectra for M_w=6.5, R_{RUP}=30 km, V_{S30}=1100 m/s for strike-slip earthquakes

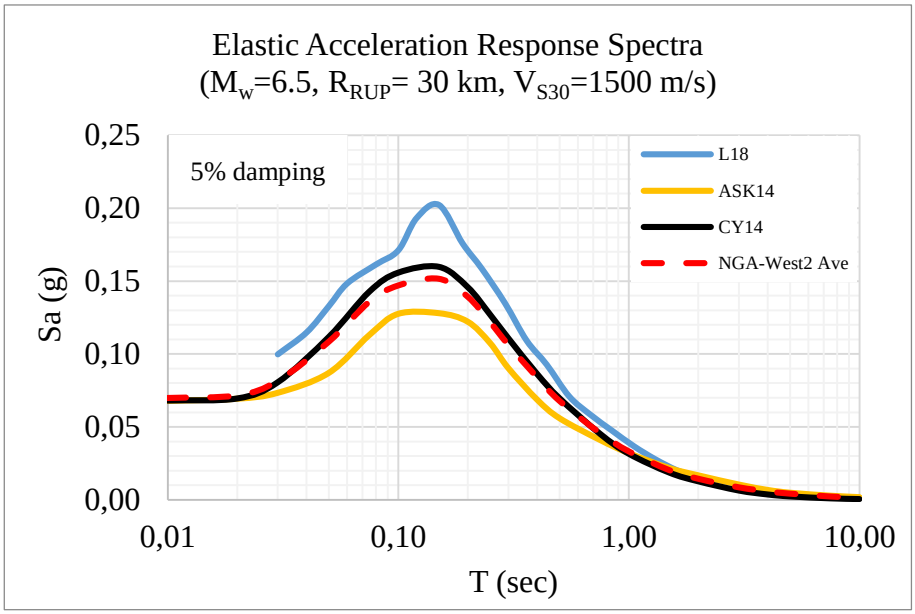

Figure 5.3. Median comparison of response spectra for M_w=6.5, R_{RUP}=30 km, V_{S30}=1500 m/s for strike-slip earthquakes

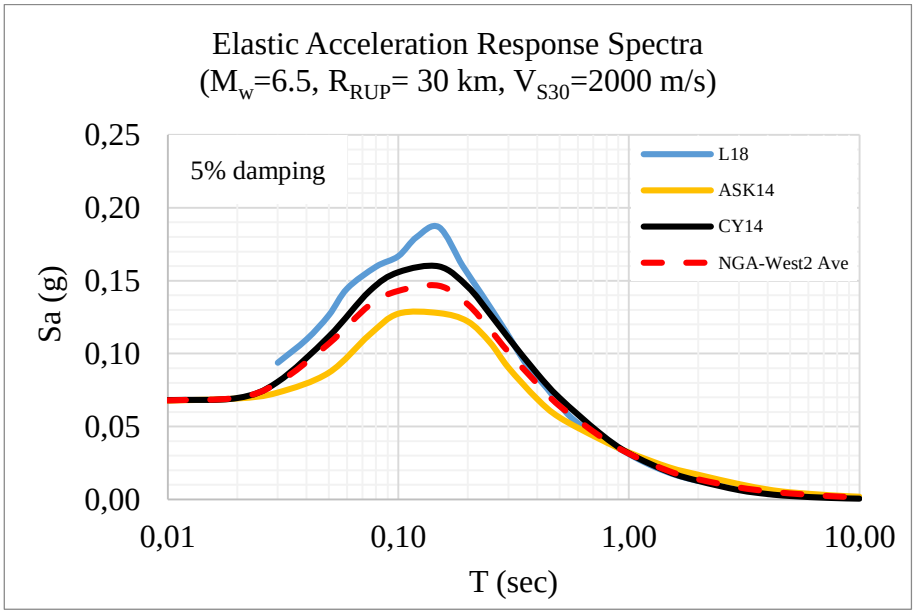

Figure 5.4. Median comparison of response spectra for M_w=6.5, R_{RUP}=30 km, V_{S30}=2000 m/s for strike-slip earthquakes

After these considerations, the within-event residuals and the between-event residuals for L18 with our input ground motion dataset are calculated by utilizing the random-effects regression process proposed by Abrahamson and Youngs (1992). Figure 5.5 - Figure 5.9 illustrate the distribution of between-event residuals generated for L18 with a dependency of moment magnitude, and depth to the top of rupture for

the oscillator periods of 0.03, 0.1, 0.5, 1, and 2 seconds, respectively. Overall, Figure 5.5 - Figure 5.9 demonstrate that the between-event residuals are negative which is an indication of overestimation at T<1 second, especially for moment magnitudes between 5 and 6. However, at long periods (T=1, 2 sec), the residuals are centered on the line of zero. The negative residuals at lower periods have a considerable over-prediction, which means that there is not an obvious trend with respect to the magnitude at such periods. This overestimation is a trend in the Turkish strong ground motion database, and a similar trend of event terms with a moment magnitude was also observed in Önder (2022). In addition, the distribution of residuals with depth to the top of rupture is heavily accumulated between 6 km to 10 km. This is because the depth to the top of rupture is derived from an empirical study (Mai et al., 2005), and most of the data is estimated between this interval.

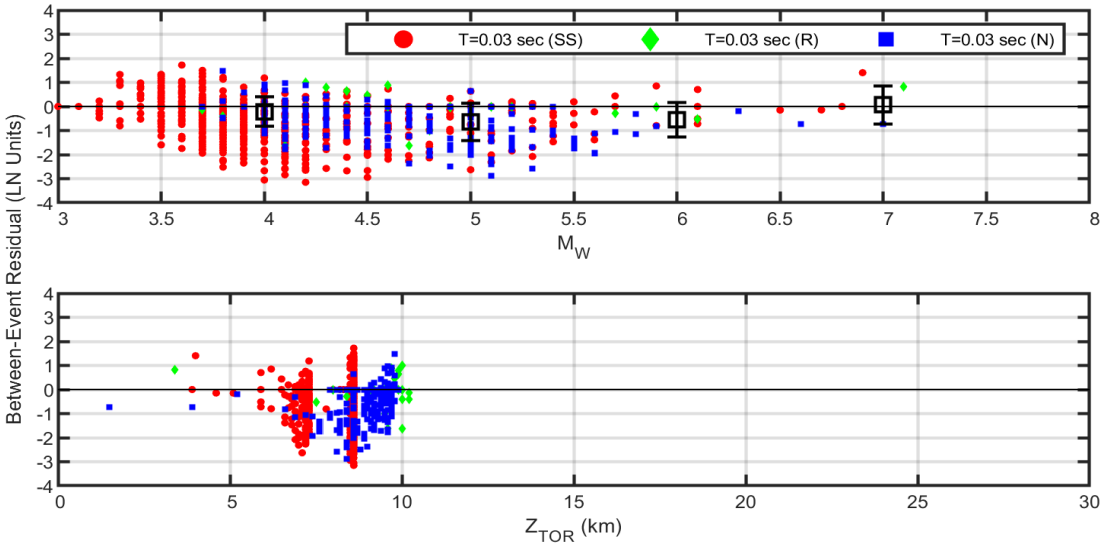

Figure 5.5. The distribution of between-event residuals with respect to moment magnitude (M_w), and the depth to the top of rupture (Z_{TOR}) for L18 at T=0.03 seconds

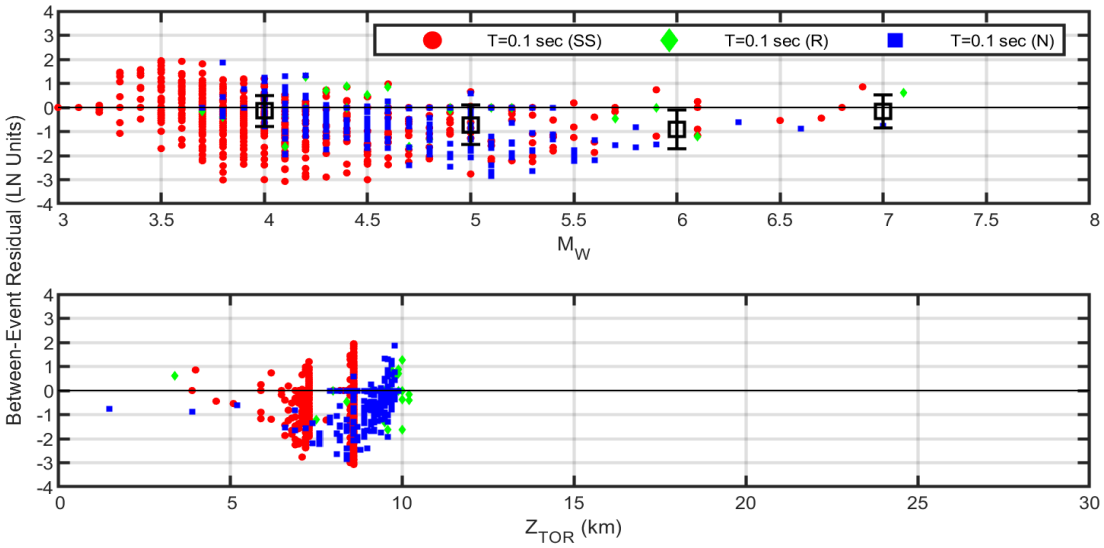

Figure 5.6. The distribution of between-event residuals with respect to moment magnitude (M_w), and the depth to the top of rupture (Z_{TOR}) for L18 at T=0.1 seconds

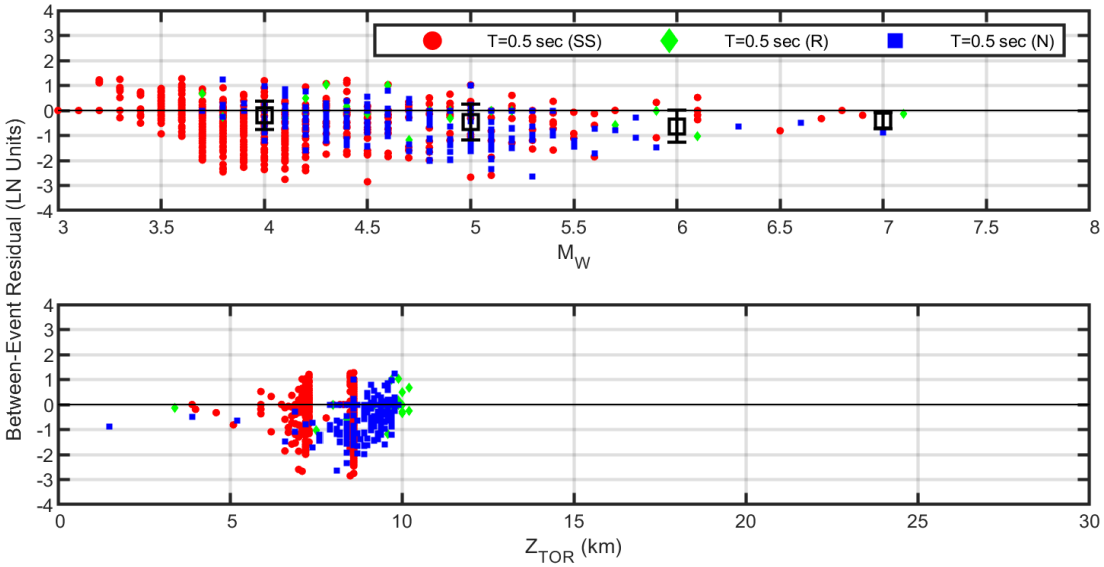

Figure 5.7. The distribution of between-event residuals with respect to moment magnitude (M_w), and depth to the top of rupture (Z_{TOR}) for L18 at T=0.5 seconds

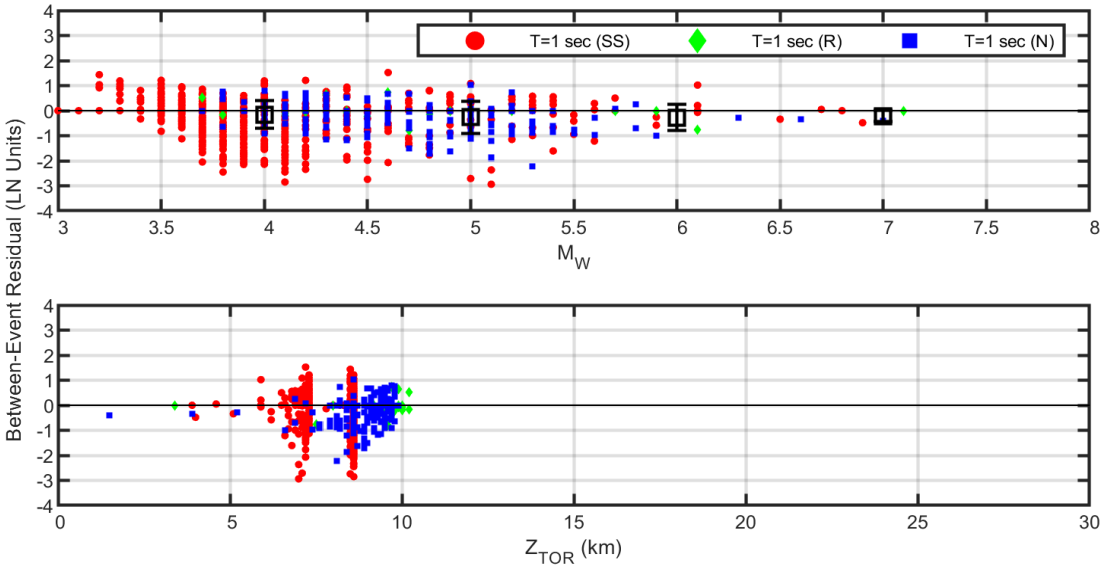

Figure 5.8. The distribution of between-event residuals with respect to moment magnitude (M_w), and depth to the top of rupture (Z_{TOR}) for L18 at T=1 second

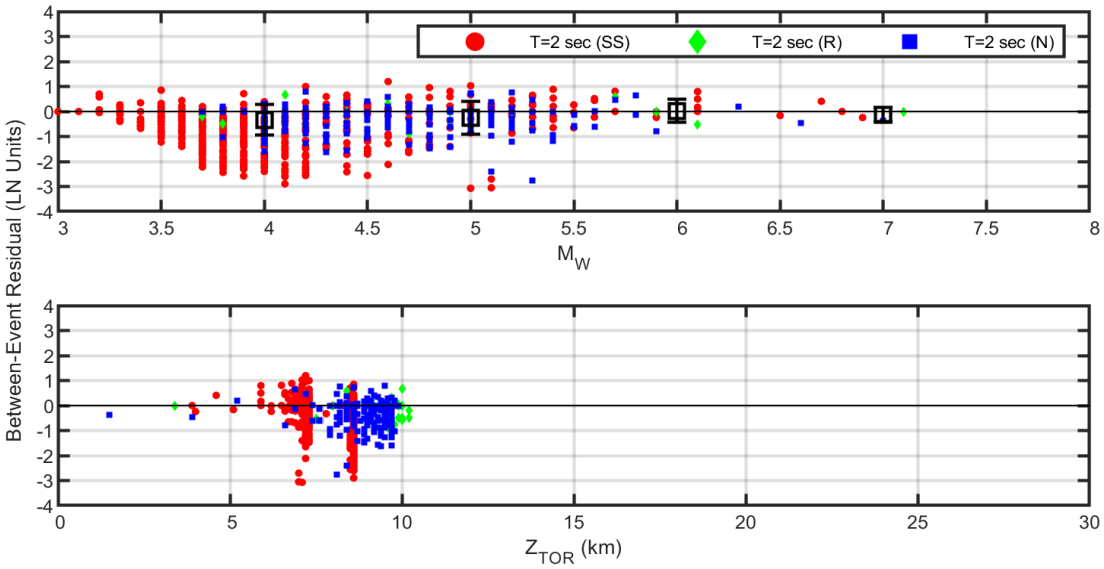

Figure 5.9. The distribution of between-event residuals with respect to moment magnitude (M_w), and depth to the top of rupture (Z_{TOR}) for L18 at T=2 seconds

Figure 5.10 - Figure 5.14 depict the distribution of within-event residuals for L18 with rupture distance for different moment magnitude intervals at T=0.03, 0.1, 0.5, 1, and 2 seconds. Figure 5.10 - Figure 5.14 illustrate that the within-event residuals are generally focused at the line of zero for all R_{RUP} at all oscillator periods for $M_w<6$. However, for $R_{RUP}<20$ km, there is a slight negative trend for $5\leq M_w<6$ due to the sparsity of near-site events at short periods (T=0.03, 0.1 s). Also, the event-term distribution for $M_w>6$ shows that there is no trend to observe due to the lack of

earthquake data with M_w>6 in the Turkish ground motion database. To conclude, the overall fit of within-event residuals at the line of zero is great with R_{RUP}>20 km for M_w<6 at all oscillator periods.

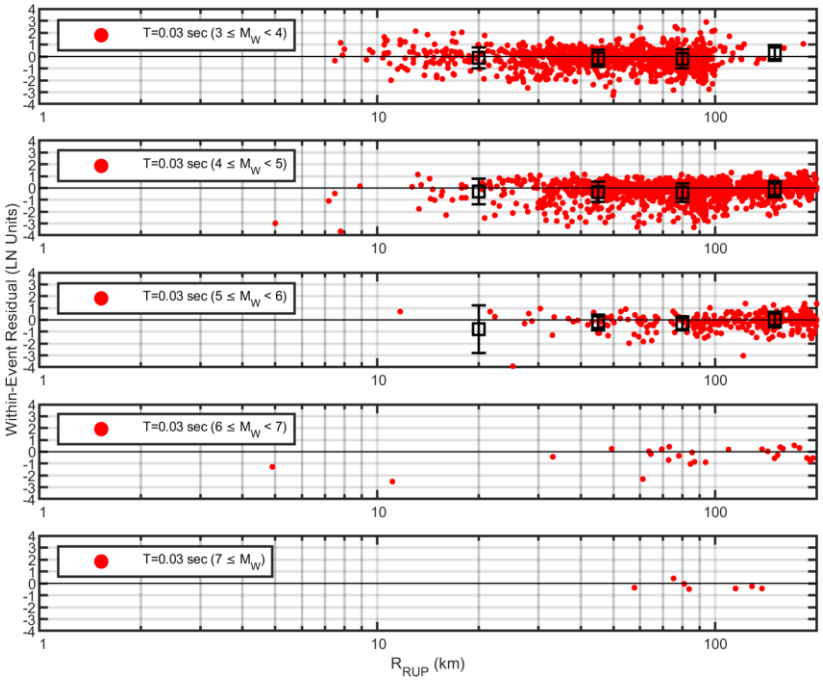

Figure 5.10. The distribution of within-event residuals with respect to rupture distance (R_{RUP}) for different moment magnitude intervals for L18 at T=0.03 seconds

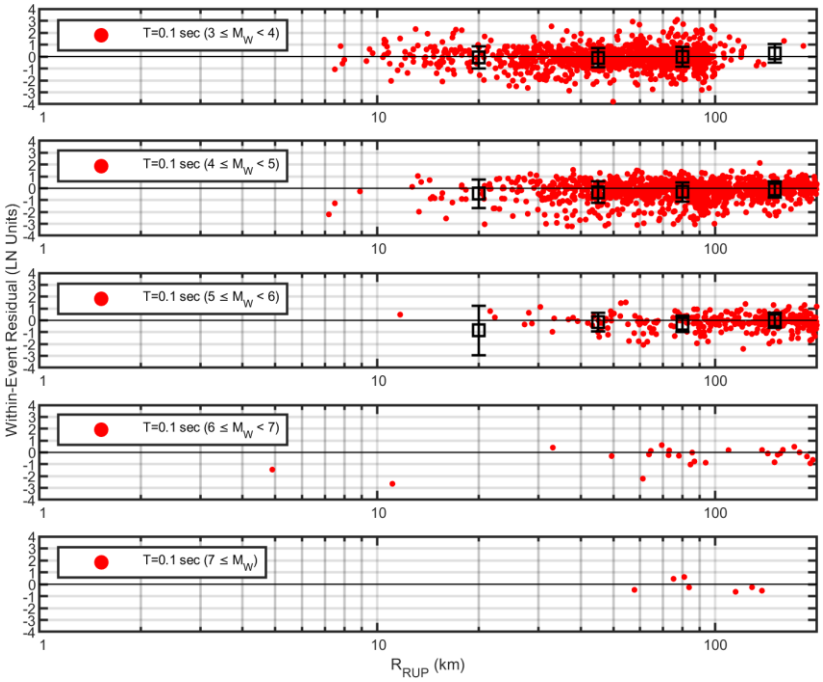

Figure 5.11. The distribution of within-event residuals with respect to rupture distance (R_{RUP}) for different moment magnitude intervals for L18 at T=0.1 seconds

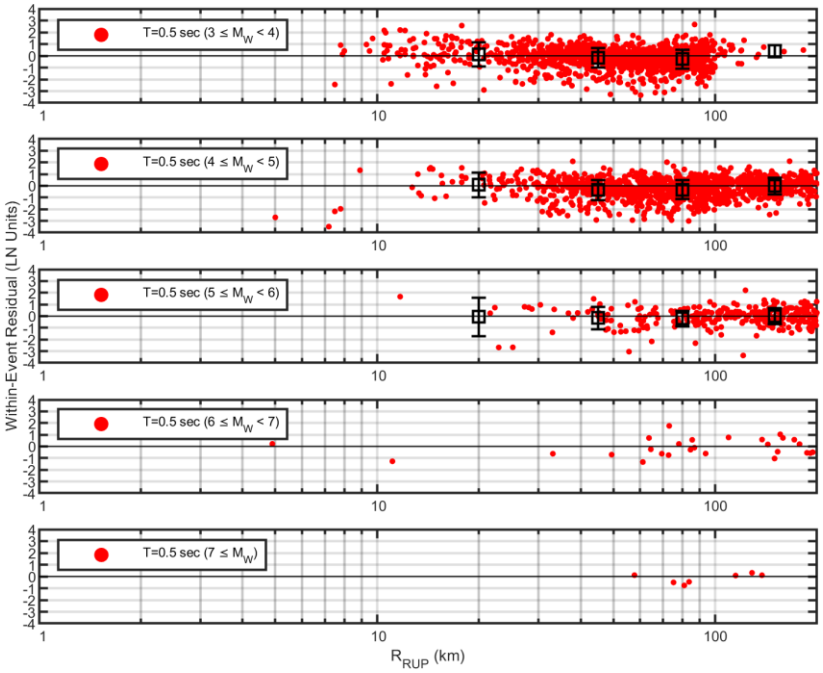

Figure 5.12. The distribution of within-event residuals with respect to rupture distance (R_{RUP}) for different moment magnitude intervals for L18 at T=0.5 seconds

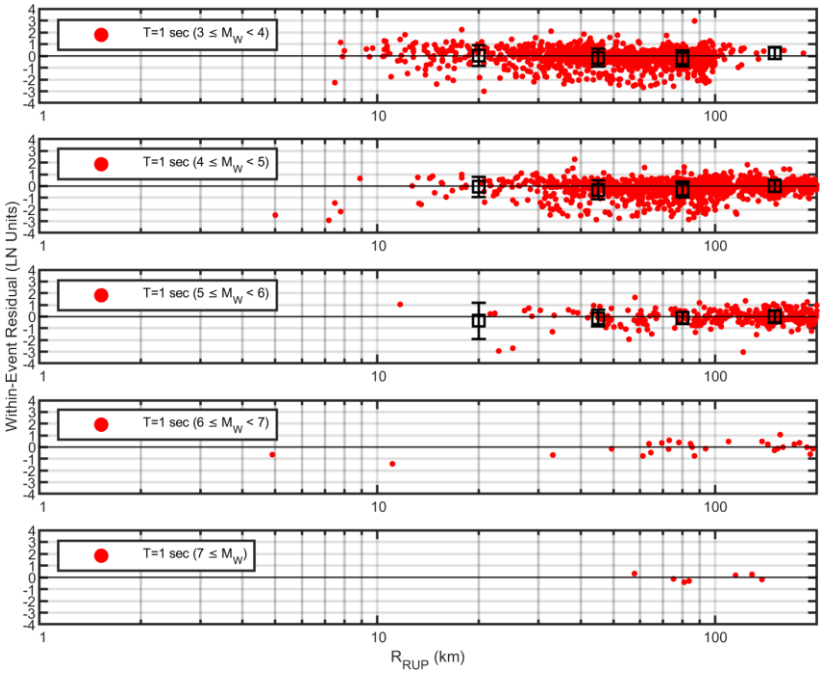

Figure 5.13. The distribution of within-event residuals with respect to rupture distance (R_{RUP}) for different moment magnitude intervals for L18 at T=1 second

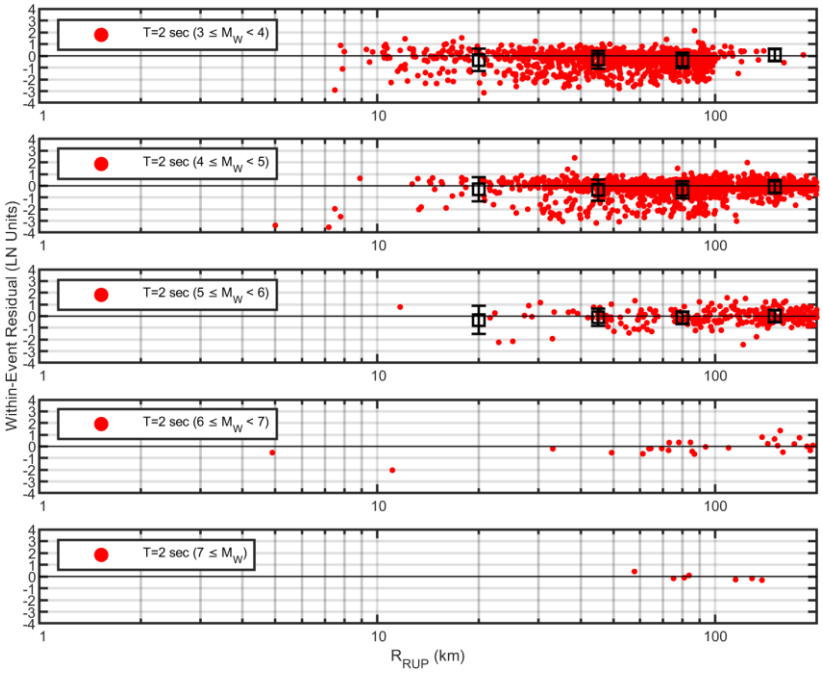

Figure 5.14. The distribution of within-event residuals with respect to rupture distance (R_{RUP}) for different moment magnitude intervals for L18 at T=2 second

Figure 5.15 illustrate the distribution of within-event residuals for L18 with V_{S30} at oscillator periods of T= 0.03, 0.1, 0.5, 1, and 2 seconds. To quantify the significance of the residuals, the p values are put to show the bias of the estimations through

whether the null hypothesis is rejected or failed to be rejected at each oscillator period. Generally, the results of p values are discussed for the 5% significance level. Figure 5.15 show that the within-event residuals are nearly at zero line at short periods (T=0.03 s, 0.1 s) with a slight overestimation bias. The large p values (p>0.05) comply with this slight shift and do not exhibit any significant bias in the residuals. Besides, there is a negative trend (meaning overestimation) for V_{S30}<700 m/s, especially for V_{S30}<500 m/s at T=0.5 s, while a positive trend (indicating underprediction) is observed at around V_{S30}=1500 m/s at T=0.5. However, there is only a slight negative trend for V_{S30}<700 m/s with a considerable underprediction at around V_{S30}=1500 m/s at long periods (T=1, 2 s). The p values at these periods (T=0.5, 1, 2 s) show significant bias since they are dramatically small, and they indicate a trend. Nevertheless, the within-event residual terms are centered around zero for V_{S30}>900 at T=2, which shows a good V_{S30} fit. The overestimation at lower frequencies indicates that there is not an obvious fit. This might be because the L18 suggested using V_{S30} with datasets similar to DATA_surf, and our dataset is not similar to this data type.

Figure 5.16 demonstrate the distribution of within-event residual for L18 with V_{SROCK} at oscillator periods T=0.03, 0.1, 0.5, 1, 2 seconds and the p-values that show the bias of the estimations. Figure 5.16 show that the event terms are located just below the zero line with a slight bias of overestimation at short periods (T=0.03, 0.1 s). The p values at these periods are 0.012, and 0.015, respectively. The within-event residuals show that there is a slight bias (p<0.05) with respect to V_{SROCK}. Also, the within-event residuals are centered at the zero line for V_{S30}>1500 m/s at longer periods (T=0.5, 1, 2 s) as opposed to the negative trend for V_{S30}<1500 m/s at the same periods. However, at T=0.5, 1, 2 seconds, p values are extremely small, which depicts a statistically significant bias. As a result, the residual analysis and the small p values (p<0.05) show that the L18 model works well for V_{SROCK}.

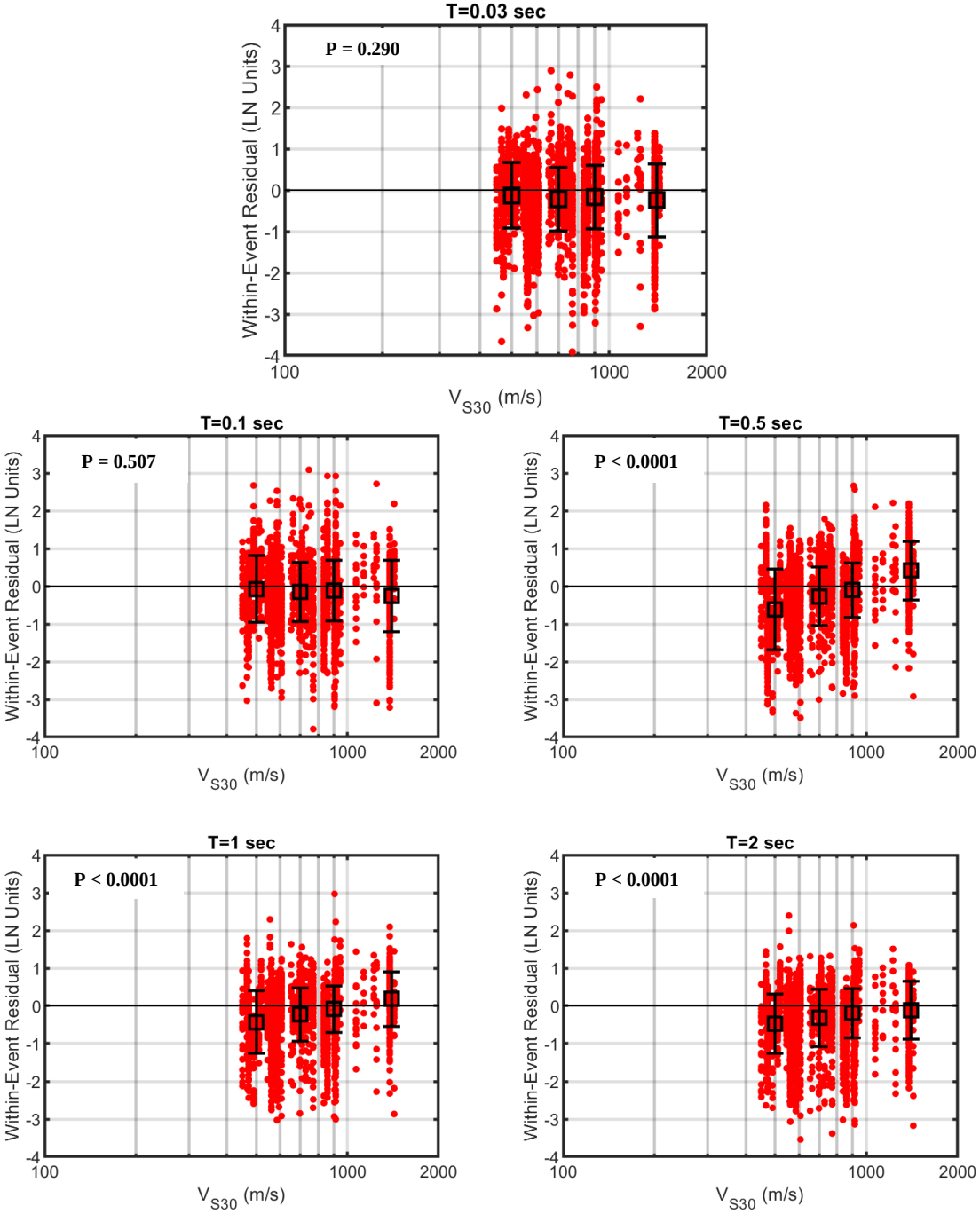

Figure 5.15. The distribution of within-event residuals with respect to V_{S30} for L18 at T=0.03, 0.1, 0.5, 1, 2 sec. The upper left panels show the p-value that represents the level of bias in the estimations

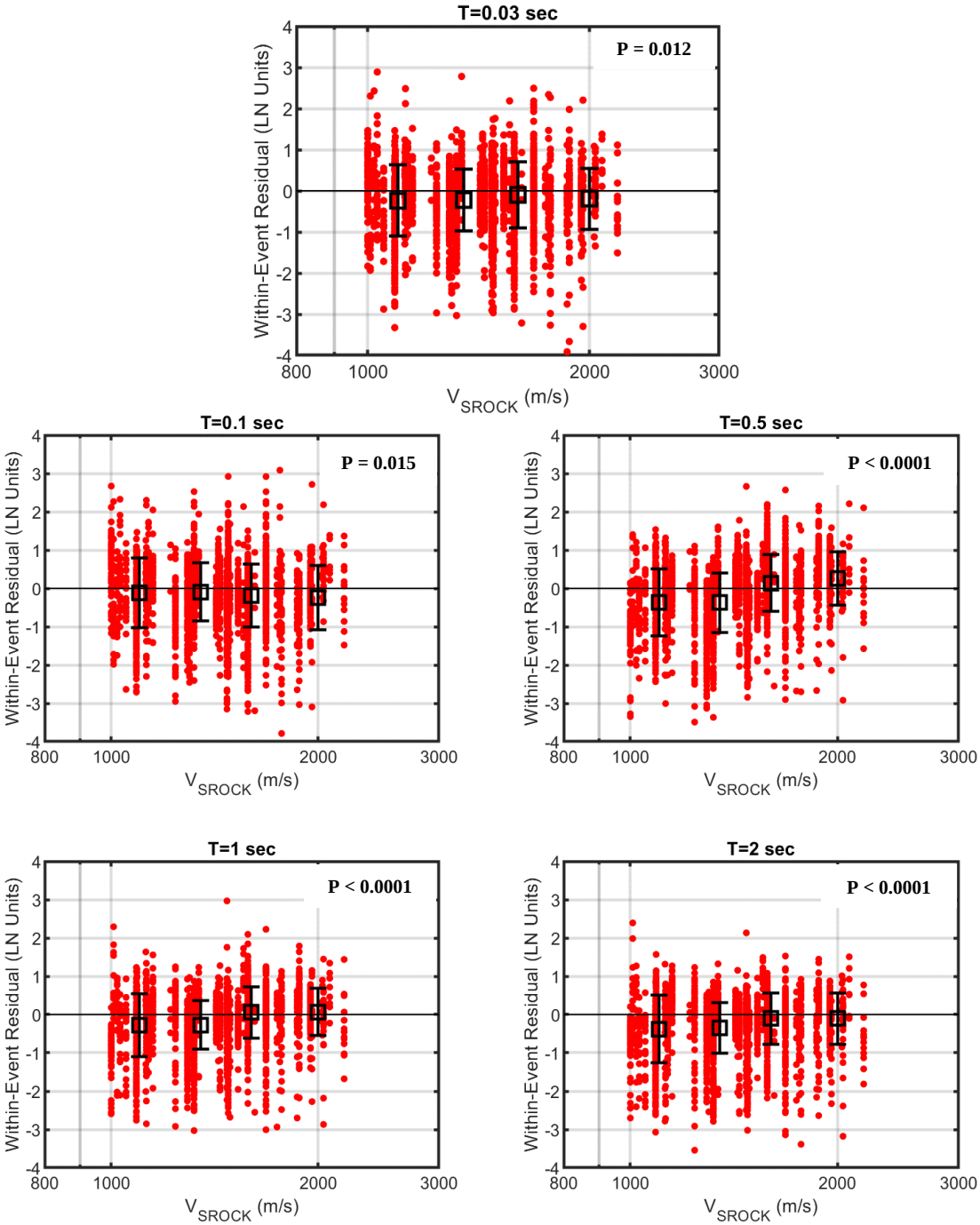

Figure 5.16. The distribution of within-event residuals with respect to V_{SROCK} for L18 at T=0.03, 0.1, 0.5, 1, 2 sec. The upper right panels show the p-value that represents the level of bias in the estimations

To conclude this chapter, L18 is utilized as the base model for analyzing its performance for estimations on rock sites of the Turkish strong ground motion database. The median predictions of L18 are quite in agreement with NGA-West2 GMMs for rock sites (V_{S30}>1000 m/s); however, L18 still overestimates for sites

with V_{S30}<1500 m/s compared to NGA-West2 GMMs at short and intermediate periods. Residual analyses illustrated that the overestimation of residuals as a function of magnitude is biased with an overestimation and it is generally an observed trend in many Turkey-adjusted GMM studies. However, the rupture distance dependency of residuals for the L18 model showed a great fit. In addition, the residual analyses for V_{S30} and small p values demonstrate a significant bias with an overestimation at long periods; therefore, the model did not work for V_{S30}. On the other hand, the residuals as a function of V_{SROCK} worked great, especially at longer periods and V_{SROCK}>1500 m/s. This is because the rock motions deconvolved from the surface level were suggested to be used with V_{SROCK} rather than V_{S30}. These results indicate that the L18 model can be used for earthquake engineering applications despite the overestimations in the between-event residuals for moment magnitude since it still stays on the safer side.

CHAPTER 6

SUMMARY AND CONCLUSIONS

This study analyzed the performance of rock GMM proposed by Laurendeau et al. (2018) (L18) for Turkey using 40 candidate strong ground motion stations and 2977 two-component ground motion records compiled from the database of the Disaster and Emergency Presidency, the Department of Earthquake (AFAD) of Turkey.

For this purpose, all strong ground motion stations available in TADAS were compiled to determine the candidate stations. The site characterization reports of 1039 ground motion stations were reviewed, and 40 candidate stations were selected. There were 6322 two-component records available in 40 seismological stations, and the quality of the raw waveforms was reviewed. After the quality-check of waveforms, 2977 records with two horizontal components were selected to be input motions. The compiled dataset consisted of events with moment magnitude ranging from 3.0 to 7.1, records with rupture distance between 4.9 km and 421.5 km, stations with V_{S30} ranging from 450 m/s to 1427 m/s, and stations with V_{SROCK} between 1000 m/s and 2183 m/s.

The simplified soil profiles were modeled for 40 stations using AFAD's site characterization reports. Each simplified soil layer is characterized by horizontal layers with dynamic (V_S, damping, and shear modulus reduction curves) and mechanical (unit weight) soil parameters. Before performing deconvolution analyses, the suitability of simplified soil profiles for equivalent linear analysis is examined through the comparison of ETF and TTF. The results showed that the general fit between ETFs and TTFs was found to be great for all stations, which indicated that the simplified soil profiles behaved linearly and they were suitable for equivalent linear analyses.

The deconvolution analyses were performed in the ground response analysis software DEEPSOIL (Hashash et. al., 2017), and the PSA_{rock} values were retrieved to examine the performance of the L18 model. To evaluate the results of 1-D equivalent

linear deconvolution analyses for each station, the AFs were plotted and compared with the S20 & H20 site amplification models. The AF plots show that many stations show a great fit with the S20 & H20 site model. However, some stations had peaks with different amplitudes than the site model, but our AFs still stayed within the mean±sigma - mean±2sigma range. In addition, there were also stations with 2 AF peaks, while the site model only had one AF peak. These differences might be because the site model used an average of simulation-based virtually generated simplified soil profiles with smooth increments in V_S profiles, whereas our AFs were determined from real V_S profiles with V_S reversals. As a result, these 1-D deconvolution analyses indicated that the deconvolution method worked quite great for all 40 stations.

To analyze the performance of the L18 model for Turkey, the between-event and within-event residuals was obtained by using the random effects regression approach (Abrahamson and Youngs, 1992), and plotted at T=0.03, 0.1, 0.5, 1, 2 s. The between-event residuals for moment magnitude indicated that the model overestimates for moment magnitudes around 5, especially at short periods. This was a general trend shown in many Turkey-adjusted GMM studies. The modifications to the residuals for moment magnitude cannot be done since most of our ground motions were not recorded by multiple stations. Our dataset mainly consisted of single-station events, as there were only 40 candidate stations selected from TADAS to represent hard rock site conditions and successfully perform deconvolution analysis. This created a problem in our between-event residuals. Thus, these between-event residuals were not real between-event residuals; therefore, modifications to the residuals cannot be done with this dataset. In terms of rupture distance, the L18 model worked quite well. However, the residual analysis for V_{S30} illustrated that the model did not work well because the L18 model suggested that V_{S30} should be used with a dataset similar to DATA_surf, which is not similar to our dataset. On the other hand, the L18 performance for V_{SROCK} was considerably great for V_{SROCK}>1500 m/s with slight overestimations for V_{SROCK}<1500 m/s, especially at longer periods. The overestimations were considered negligible because it was safer for many earthquake engineering and important infrastructure applications for rock sites. These results indicated that the L18 model can be used for Turkey in

earthquake engineering applications despite the overestimations in the between-event residuals.

REFERENCES

Abrahamson, N. A., & Silva, W. J. (1997). Empirical response spectral attenuation relations for shallow crustal earthquakes. Seismological research letters, 68(1), 94-127.

Akin, M. K., Kramer, S. L., & Topal, T. (2013). Evaluation of site amplification of Erbaa, Tokat (Turkey).

Akkar, S., Çağnan, Z., Yenier, E., Erdoğan, Ö., Sandıkkaya, M. A., & Gülkan, P. (2010). The recently compiled Turkish strong motion database: preliminary investigation for seismological parameters. Journal of Seismology, 14, 457-479.

Akkar, S., Kale, Ö., Ansari, A., Durgaryan, R., Gündoğan, A., Hamzehloo, H., Harmandar E., Tsereteli N., Waseem M., Yazjeen T., Yilmaz, M. T. (2014). EMME strong-motion database serving for predictive model selection to EMME ground motion logic-tree applications. In Second European Conference on Earthquake Engineering and Seismology.

Ancheta, T. D., Darragh, R. B., Stewart, J. P., Seyhan, E., Silva, W. J., Chiou, B. S. J., Wooddell, K. E., Graves, R. W., Kottke, A. R., Boore, D. M., Kishida, T., Donahue, J. L. (2014). NGA-West2 database. Earthquake Spectra, 30(3), 989-1005.

Ashayeri, I., Memari, M. A., & Haghshenas, E. (2021). Seismic microzonation of Sarpol-e-zahab after Mw 7.3 2017 Iran earthquake: 1D-equivalent linear approach. Bulletin of Earthquake Engineering, 19, 605-622.

Atik, L. A., Gregor, N. J., Abrahamson, N. A., & Kottke, A. R. (2022). GMPE-consistent hard rock site adjustment factors for Western North America. Earthquake Spectra, 38(4), 2371-2397.

Atkinson, G. M., & Boore, D. M. (2006). Earthquake ground motion prediction equations for eastern North America. Bulletin of the seismological society of America, 96(6), 2181-2205.

Bajaj, K., & Anbazhagan, P. (2019). Comprehensive amplification estimation of the Indo Gangetic Basin deep soil sites in the seismically active area. Soil Dynamics and Earthquake Engineering, 127, 105855.

Bard, P. Y., Bora, S. S., Hollender, F., Laurendeau, A., & Traversa, P. (2020). Are the standard VS-Kappa host-to-target adjustments the only way to get

consistent hard rock ground motion prediction?. Pure and Applied Geophysics, 177, 2049-2068.

Boore, D. M., Joyner, W. B., & Fumal, T. E. (1997). Equations for estimating horizontal response spectra and peak acceleration from western North American earthquakes: A summary of recent work. Seismological research letters, 68(1), 128-153.

Boore, D. M. (2016). Determining generic velocity and density models for crustal amplification calculations, with an update of the generic site amplification for. Bulletin of the Seismological Society of America, 106(1), 313-317.

Bozorgnia, Yousef & Ancheta, Timothy & Atkinson, Gail & Baker, Jack & Baltay, Annemarie & Boore, David & Campbell, Kenneth & Chiou, Brian & Darragh, Robert & Day, Steve & Donahue, Jennifer & Graves, Robert & Gregor, Nick & Hanks, Thomas & Idriss, I. & Kamai, Ronnie & Kishida, Tadahiro & Youngs, R. (2014). NGA-West2 research project. Earthquake Spectra. 30.

Cabas, A., & Rodriguez-Marek, A. (2017). VS-K0 correction factors for input ground motions used in seismic site response analyses. Earthquake Spectra, 33(3), 917-941.

Campbell, K. W. (2003). Prediction of strong ground motion using the hybrid empirical method and its use in the development of ground motion (attenuation) relations in eastern North America. Bulletin of the Seismological Society of America, 93(3), 1012-1033.

Choi, Y., & Stewart, J. P. (2005). Nonlinear site amplification as function of 30 m shear wave velocity. Earthquake spectra, 21(1), 1-30.

Hashash, Y. M. A., Musgrove, M. I., Harmon, J. A., Ilhan, O., Groholski, D. R., Phillips, C. A., & Park, D. (2017). DEEPSOIL 7.0. User manual, 1-169.

Edwards, B., & Fäh, D. (2017). Prediction of earthquake ground motion at rock sites in Japan: evaluation of empirical and stochastic approaches for the PEGASOS Refinement Project. Geophysical Journal International, 211(2), 766-783.

Electric Power Research Institute. (1993). (tech.). *Guidelines for Determining Design Basis Ground Motions* (Vol. 1–5).

FEMA. (2020). (tech.). *NEHRP Recommended Seismic Provisions for New Buildings and Other Structures* (Vol. I). Washington D.C.

Gülerce, Z., Kargoığlu, B., & Abrahamson, N. A. (2016). Turkey-adjusted NGA-W1 horizontal ground motion prediction models. Earthquake Spectra, 32(1), 75-100.

Hashash, Y. M., Ilhan, O., Harmon, J. A., Parker, G. A., Stewart, J. P., Rathje, E. M., Campbell, K. W., & Silva, W. J. (2020). Nonlinear site amplification model for ergodic seismic hazard analysis in Central and eastern North America. Earthquake Spectra, 36(1), 69–86.

Idriss, I. M., & Akky, M. R. (1979). Primary variables influencing generation of earthquake motions by a deconvolution process. In Structural mechanics in reactor technology. Transactions. Vol. K (a).

Jeong, S., & Bradley, B. A. (2017). Amplification of strong ground motions at Heathcote Valley during the 2010–2011 Canterbury earthquakes: Observation and 1-D site response analysis. Soil Dynamics and Earthquake Engineering, 100, 345-356.

KADİRİOĞLU, F. T., & Kartal, R. F. (2016). The new empirical magnitude conversion relations using an improved earthquake catalogue for Turkey and its near vicinity (1900-2012). Turkish Journal of Earth Sciences, 25(4), 300-310.

Kale, Ö., Akkar, S., Ansari, A., & Hamzehloo, H. (2015). A ground-motion predictive model for Iran and Turkey for horizontal PGA, PGV, and 5% damped response spectrum: Investigation of possible regional effects. Bulletin of the Seismological Society of America, 105(2A), 963-980.

Kramer, S. L. (1996). Geotechnical earthquake engineering. Pearson Education India.

Kurtuluş, C., Sertçelik, F., Sertçelik, İ., Kuru, T., Tekin, K., Ateş, E., Apak, A., Kökbudak, D., Sezer, S., & Yalçin, D. (2020). Türkiye ulusal kuvvetli yer hareketi kayıt istasyonlarının zemin özelliklerininin belirlenmesi. Gazi Üniversitesi Mühendislik Mimarlık Fakültesi Dergisi, 35(4), 1829-1846.

Laurendeau, A., Cotton, F., Ktenidou, O. J., Bonilla, L. F., & Hollender, F. (2013). Rock and stiff-soil site amplification: Dependency on VS 30 and kappa (κ 0). Bulletin of the Seismological Society of America, 103(6), 3131-3148.

Laurendeau, A., Bard, P. Y., Hollender, F., Perron, V., Foundotos, L., Ktenidou, O. J., & Hernandez, B. (2018). Derivation of consistent hard rock (1000< VS< 3000 m/s) GMPEs from surface and down-hole recordings: analysis of KiK-net data. Bulletin of Earthquake Engineering, 16, 2253-2284.

Mai, P. M., Spudich, P., & Boatwright, J. (2005). Hypocenter locations in finite-source rupture models. Bulletin of the Seismological Society of America, 95(3), 965-980.

Markham, C. S., Bray, J. D., Macedo, J., & Luque, R. (2016). Evaluating nonlinear effective stress site response analyses using records from the Canterbury earthquake sequence. Soil Dynamics and Earthquake Engineering, 82, 84-98.

Mazzoni, S., McKenna, F., Scott, M. H., & Fenves, G. L. (2006). OpenSees command language manual. Pacific Earthquake Engineering Research (PEER) Center, 264(1), 137-158.

Paolucci, E., Albarello, D., Lunedei, E., Peruzzi, G., Papasidero, M. P., Francescone, M., & Pieruccini, P. DYNAMIC CHARACTERIZATION AND DECONVOLUTION ANALYSIS FOR SOME SITES OF THE NATIONAL ACCELEROMETRIC NETWORK (RAN).

PEER. (2010). PEER Strong Motion Database. University of California, Berkeley, United States. Available online: https://peer.berkeley.edu/peer-strong-ground motion-databases (accessed on January 2023).

Pezeshk, S., Zandieh, A., & Tavakoli, B. (2011). Hybrid empirical ground motion prediction equations for eastern North America using NGA models and updated seismological parameters. Bulletin of the Seismological Society of America, 101(4), 1859-1870.

Poul, M. K., & Zerva, A. (2018). Efficient time-domain deconvolution of seismic ground motions using the equivalent-linear method for soil-structure interaction analyses. Soil Dynamics and Earthquake Engineering, 112, 138-151.

Power, M., Chiou, B., Abrahamson, N., Bozorgnia, Y., Shantz, T., & Roblee, C. (2008). An overview of the NGA project. Earthquake spectra, 24(1), 3-21.

Sandıkkaya, M. A., Akkar, S., & Bard, P. Y. (2013). A nonlinear site-amplification model for the next pan-European ground-motion prediction equations. Bulletin of the Seismological Society of America, 103(1), 19-32.

Sandıkkaya, M. A., & Akkar, S. (2017). Cumulative absolute velocity, Arias intensity and significant duration predictive models from a pan-European strong-motion dataset. Bulletin of Earthquake Engineering, 15, 1881-1898.

Scherbaum, F., Schmedes, J., & Cotton, F. (2004). On the conversion of source-to-site distance measures for extended earthquake source models. Bulletin of the Seismological Society of America, 94(3), 1053-1069.

Seyhan, E., & Stewart, J. P. (2014). Semi-empirical nonlinear site amplification from NGA-West2 data and simulations. Earthquake Spectra, 30(3), 1241-1256.

Stanko, D., Gülerce, Z., Markušić, S., & Šalić, R. (2019). Evaluation of the site amplification factors estimated by equivalent linear site response analysis using time series and random vibration theory based approaches. Soil Dynamics and Earthquake Engineering, 117, 16-29.

Stewart, J. P., Parker, G. A., Atkinson, G. M., Boore, D. M., Hashash, Y. M., & Silva, W. J. (2020). Ergodic site amplification model for central and eastern North America. Earthquake Spectra, 36(1), 42-68.

Tadas. AFAD. (n.d.). https://tadas.afad.gov.tr/

Toro, G. R., Abrahamson, N. A., & Schneider, J. F. (1997). Model of strong ground motions from earthquakes in central and eastern North America: Best estimates and uncertainties. Seismological Research Letters, 68(1), 41-57.

TBDY-2018. (2018). Turkish Building Earthquake Regulation. Ministry of Interior, Disaster and Emergency Management Authority (AFAD). Istanbul, Turkey (In Turkish). Available online: https://www.afad.gov.tr/kurumlar/afad.gov.tr/2309/files/TBDY_2018.pdf (accessed on January 2023).

Walling, M., Silva, W., & Abrahamson, N. (2008). Nonlinear site amplification factors for constraining the NGA models. Earthquake spectra, 24(1), 243-255.

Wells, D. L., & Coppersmith, K. J. (1994). New empirical relationships among magnitude, rupture length, rupture width, rupture area, and surface displacement. Bulletin of the seismological Society of America, 84(4), 974-1002.

APPENDICES

A. V_S profiles of candidate stations with only MASW measurement

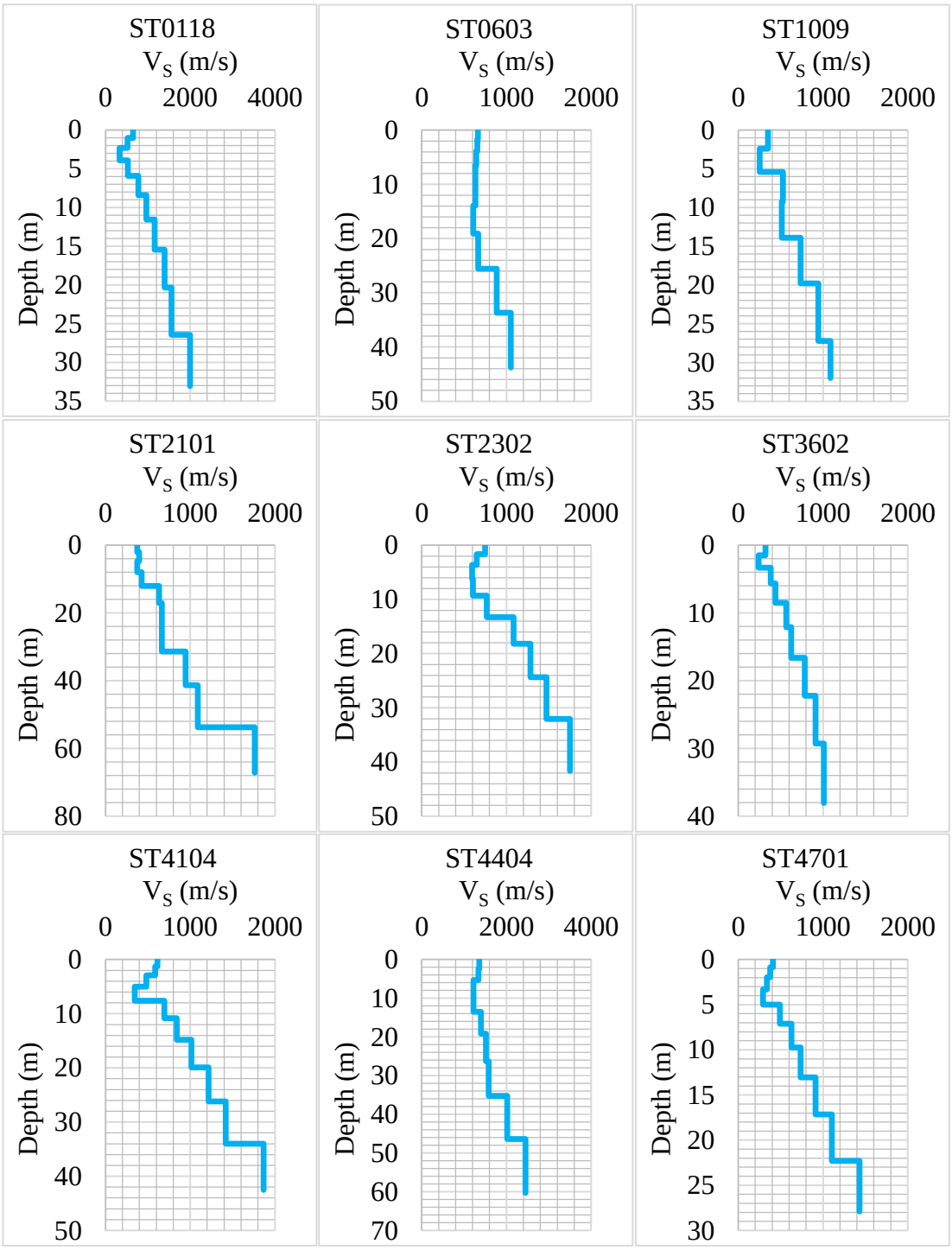

Figure A.1. V_S profiles of stations ST0118, ST0603, ST1009, ST2101, ST2302, ST3602, ST4104, ST4404, ST4701

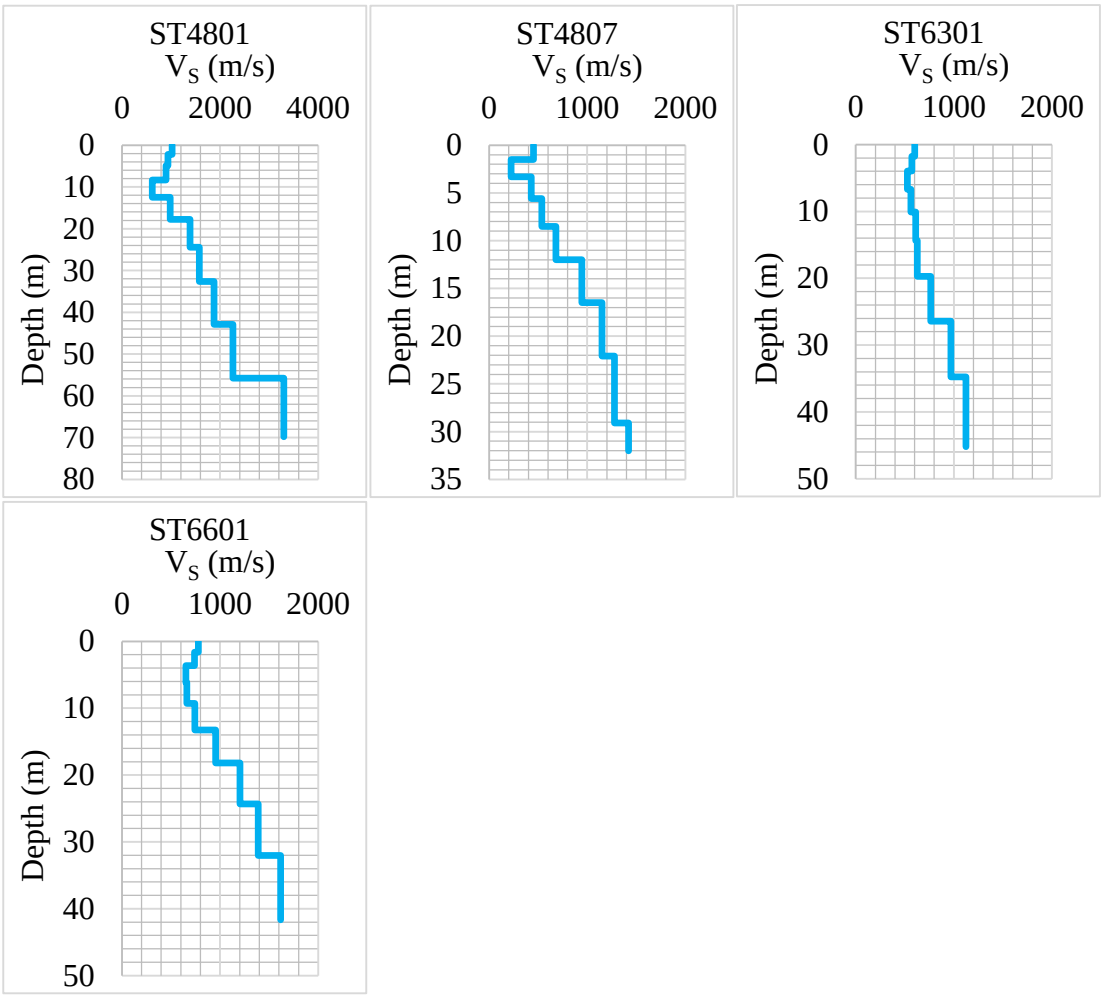

Figure A.2. V_S profiles of stations ST4801, ST4807, ST6301, ST6601

B. V_S profiles of candidate stations with MASW and ReMi measurement

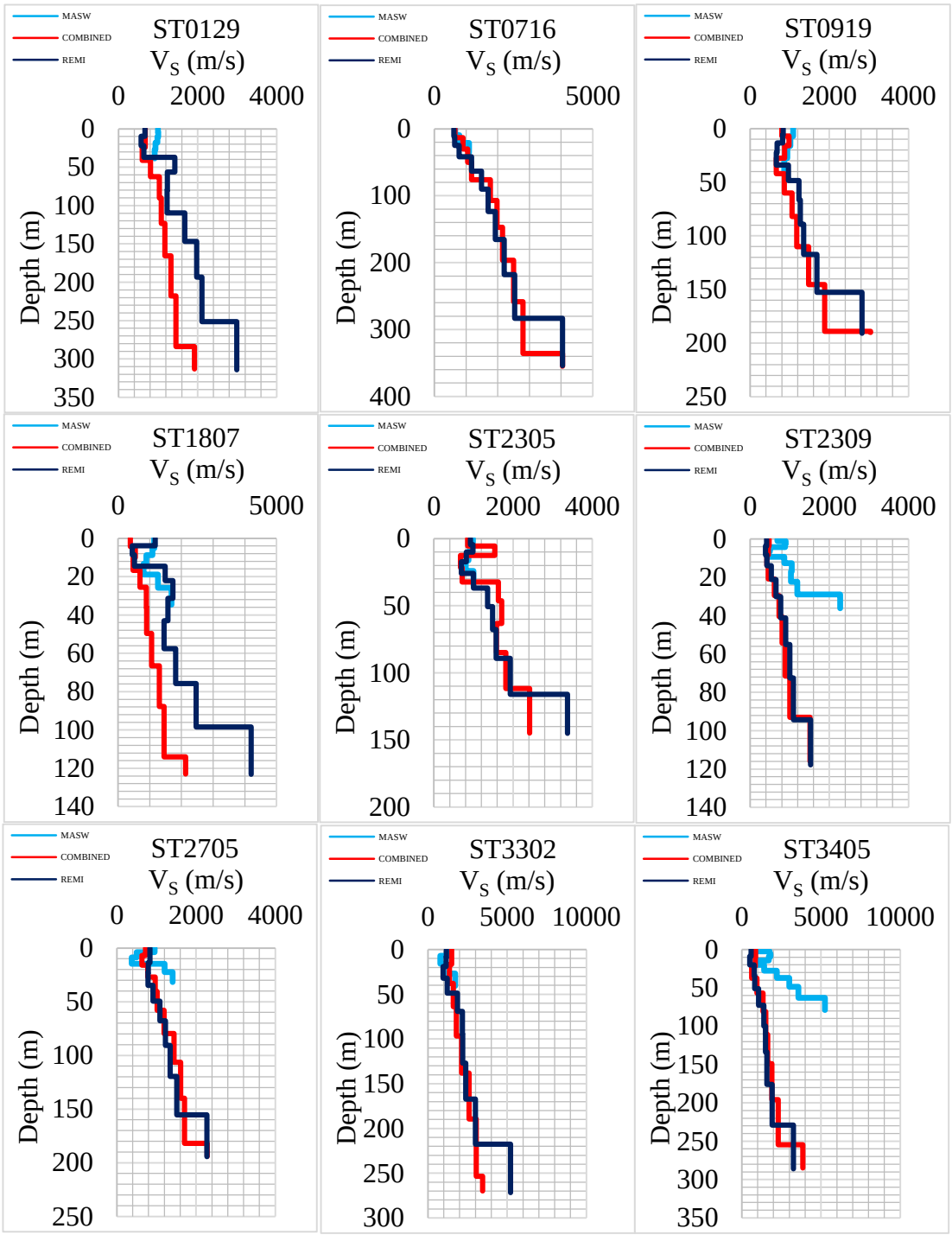

Figure B.1. V_S profiles of stations ST0129, ST0716, ST0919, ST1807, ST2305, ST2309, ST2705, ST3302, ST3405

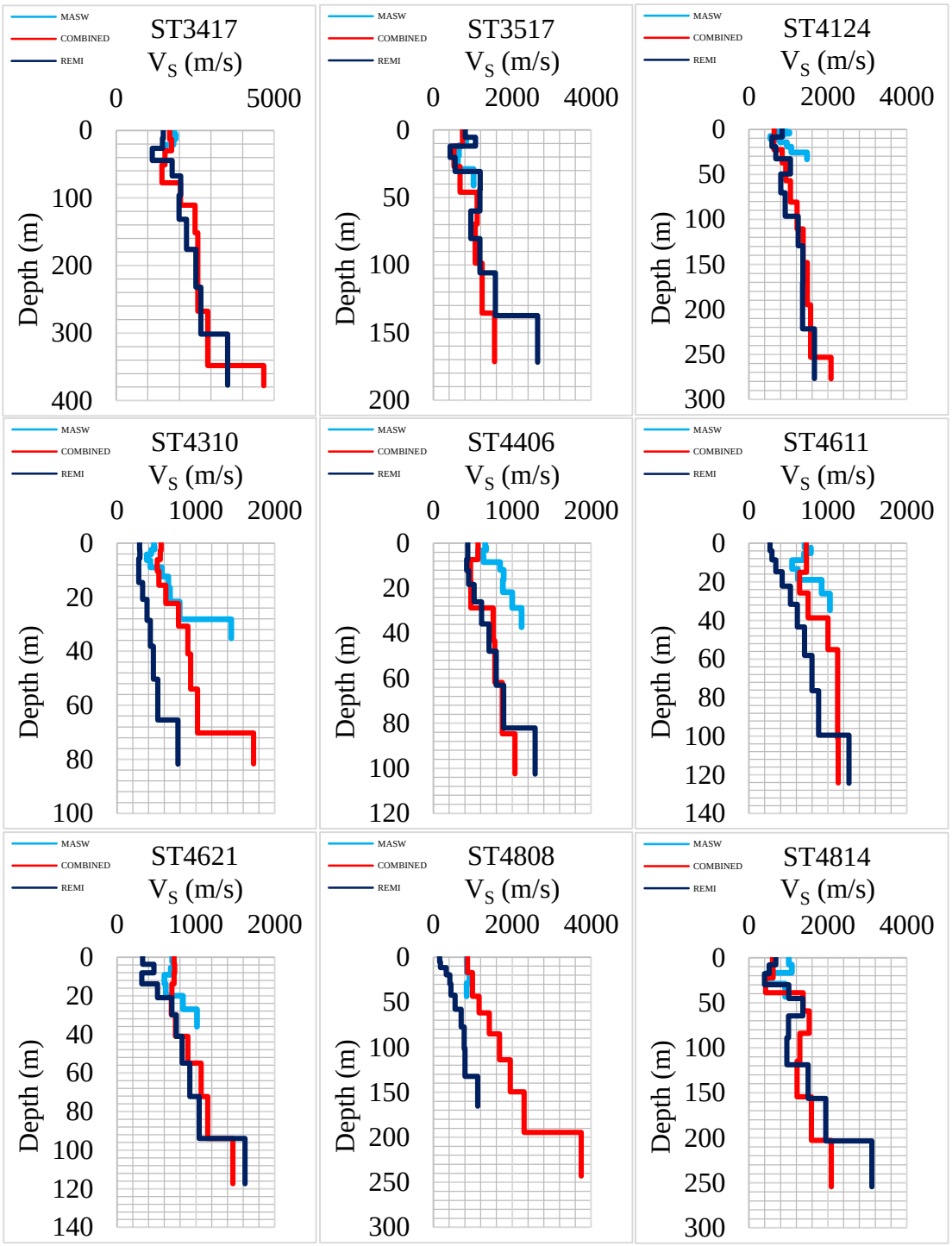

Figure B.2. V_S profiles of stations ST3417, ST3517, ST4124, ST4310, ST4406, ST4611, ST4621, ST4808, ST4814

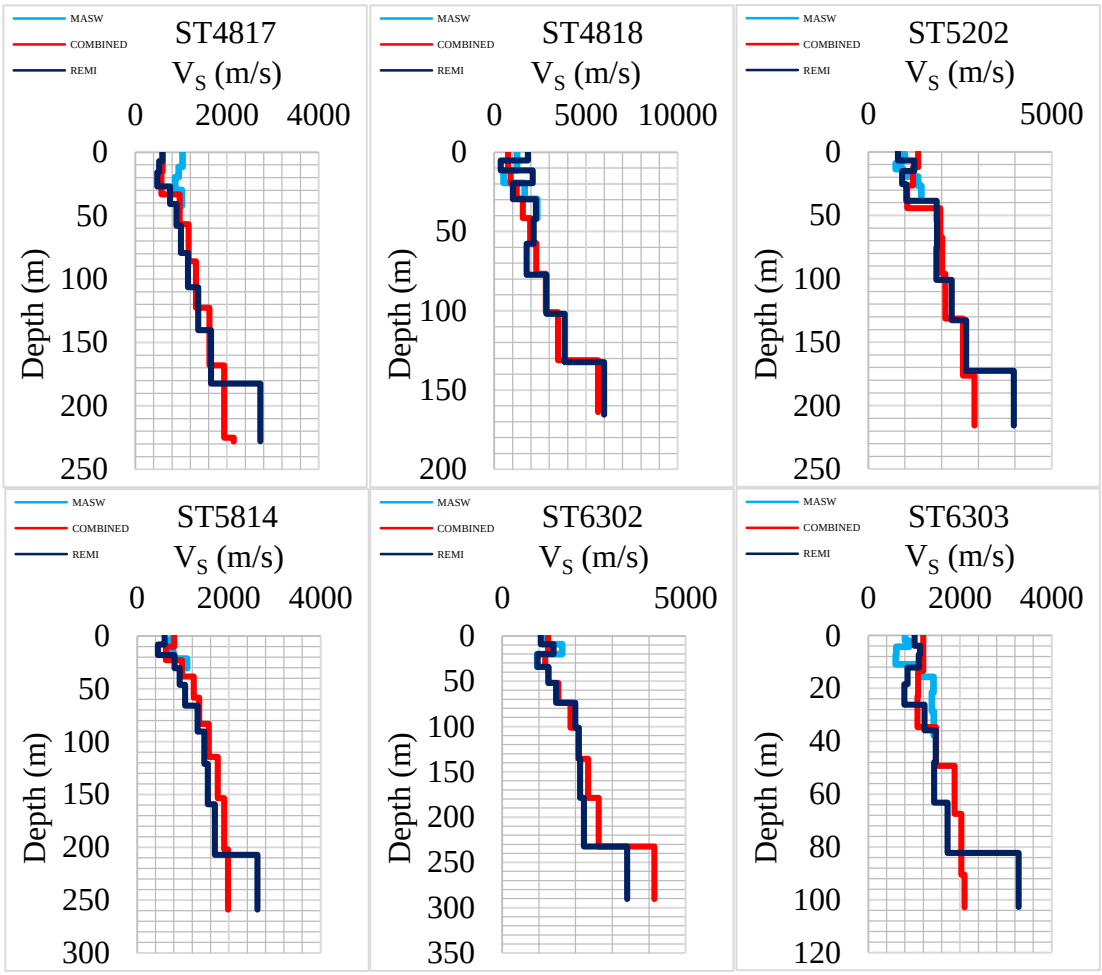

Figure B.3. V_S profiles of stations ST4817, ST4818, ST5202, ST5814, ST6302, ST6303

C. Comparison of ETF and TTF of candidate stations

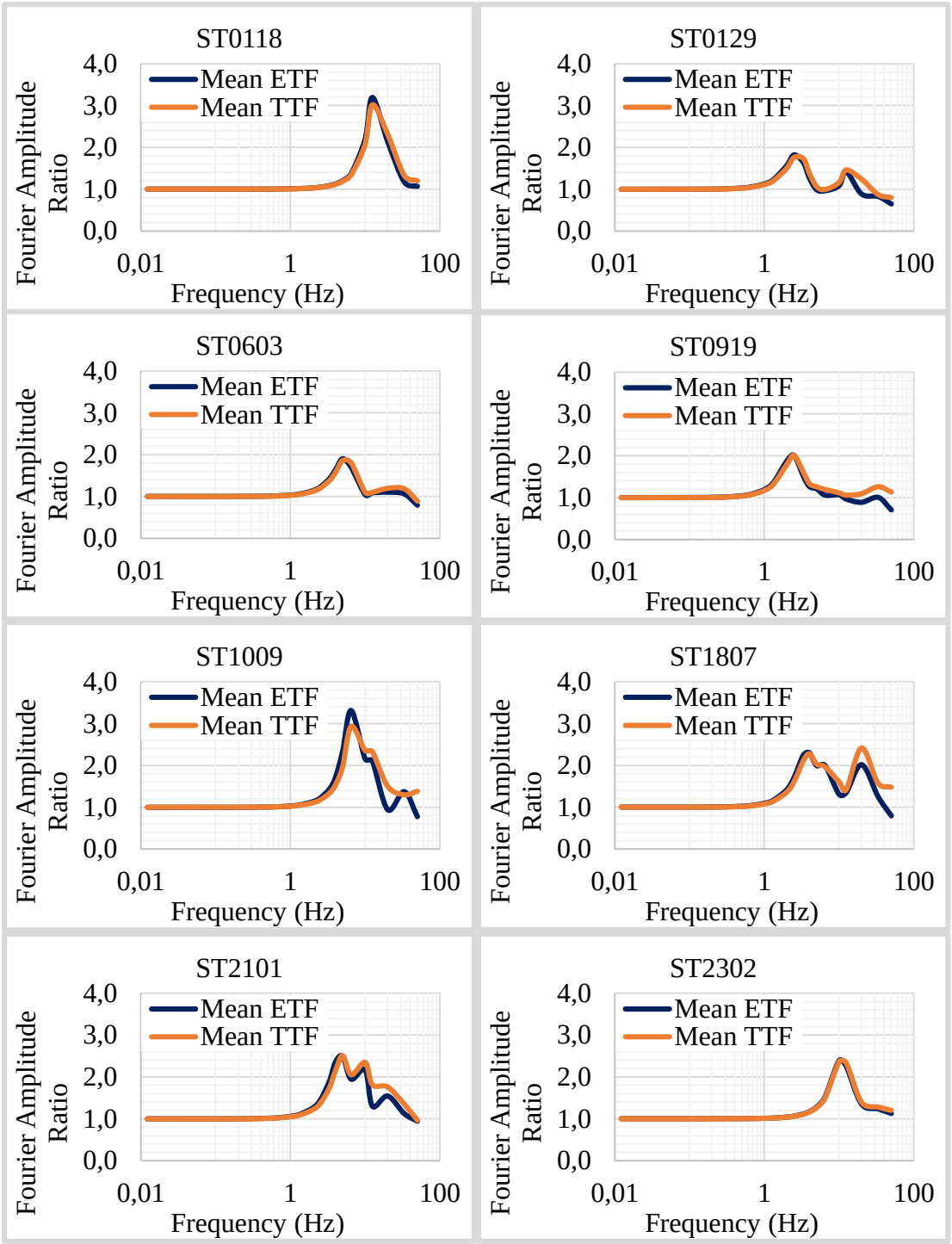

Figure C.1. Comparison of ETF and TTF of candidate stations ST0118, ST0129, ST0603, ST0919, ST1009, ST1807, ST2101, ST2302

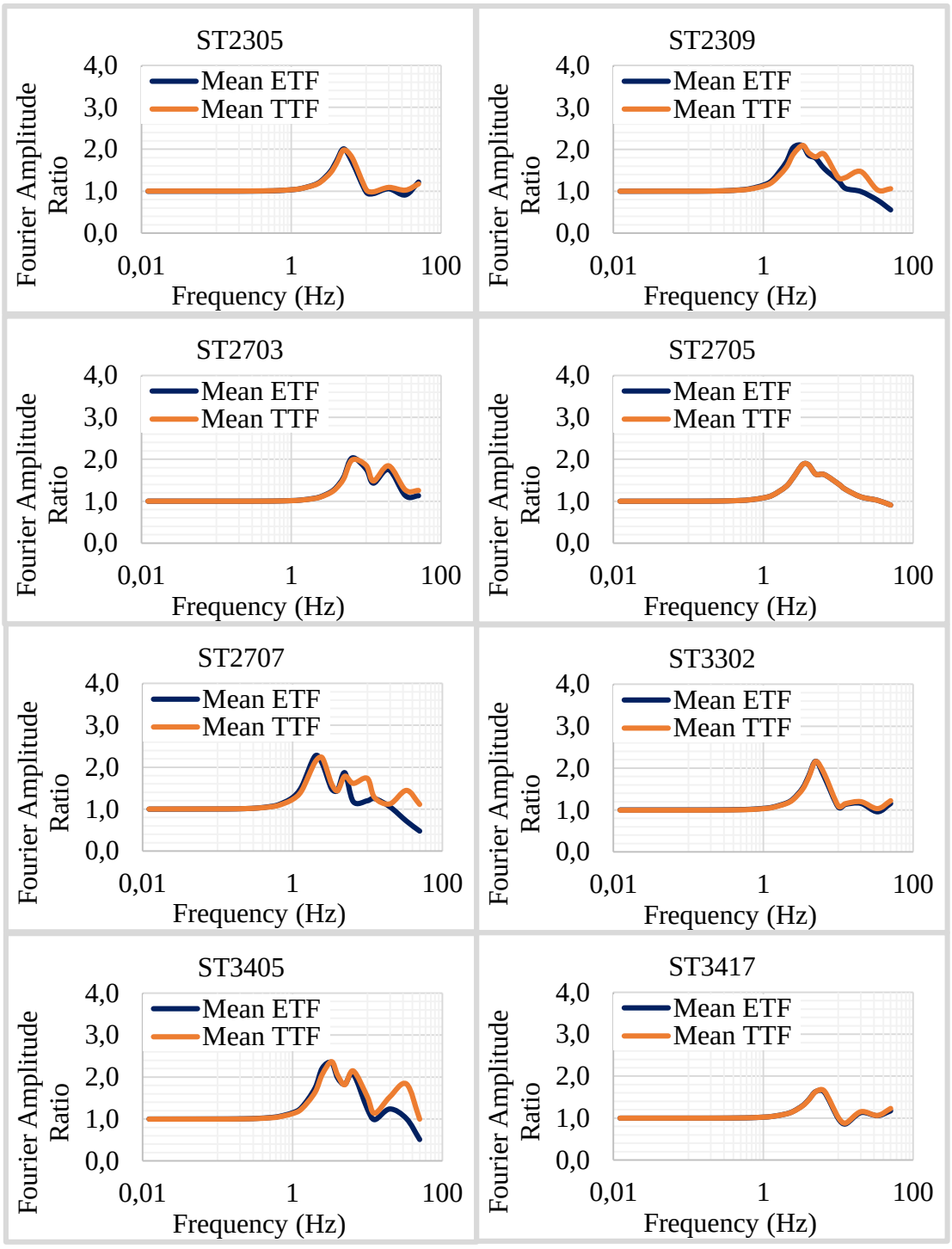

Figure C.2. Comparison of ETF and TTF of candidate stations ST2305, ST2309, ST2703, ST2705, ST2707, ST3302, ST3405, ST3417

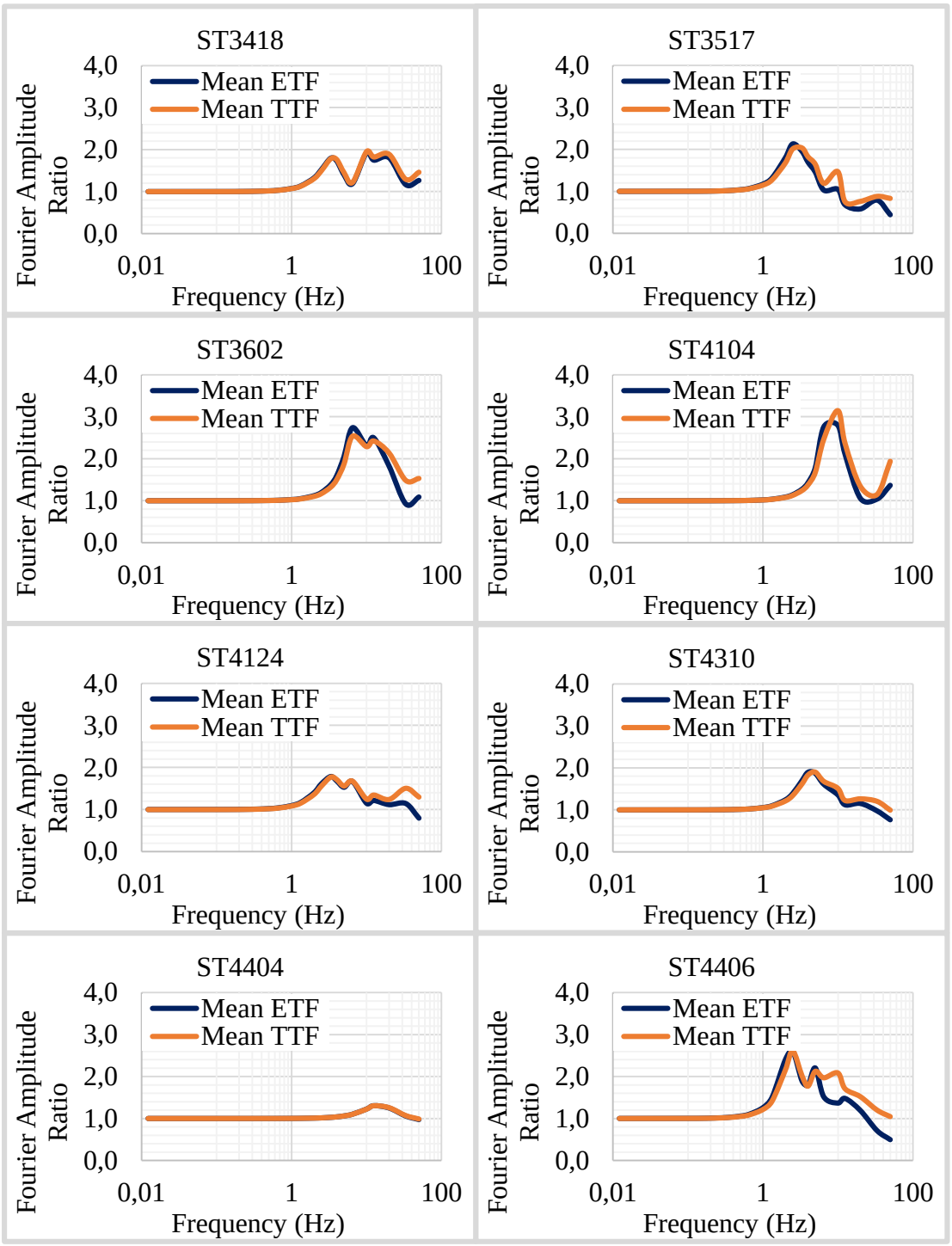

Figure C.3. Comparison of ETF and TTF of candidate stations ST3418, ST3517, ST3602, ST4104, ST4124, ST4310, ST4404, ST4406

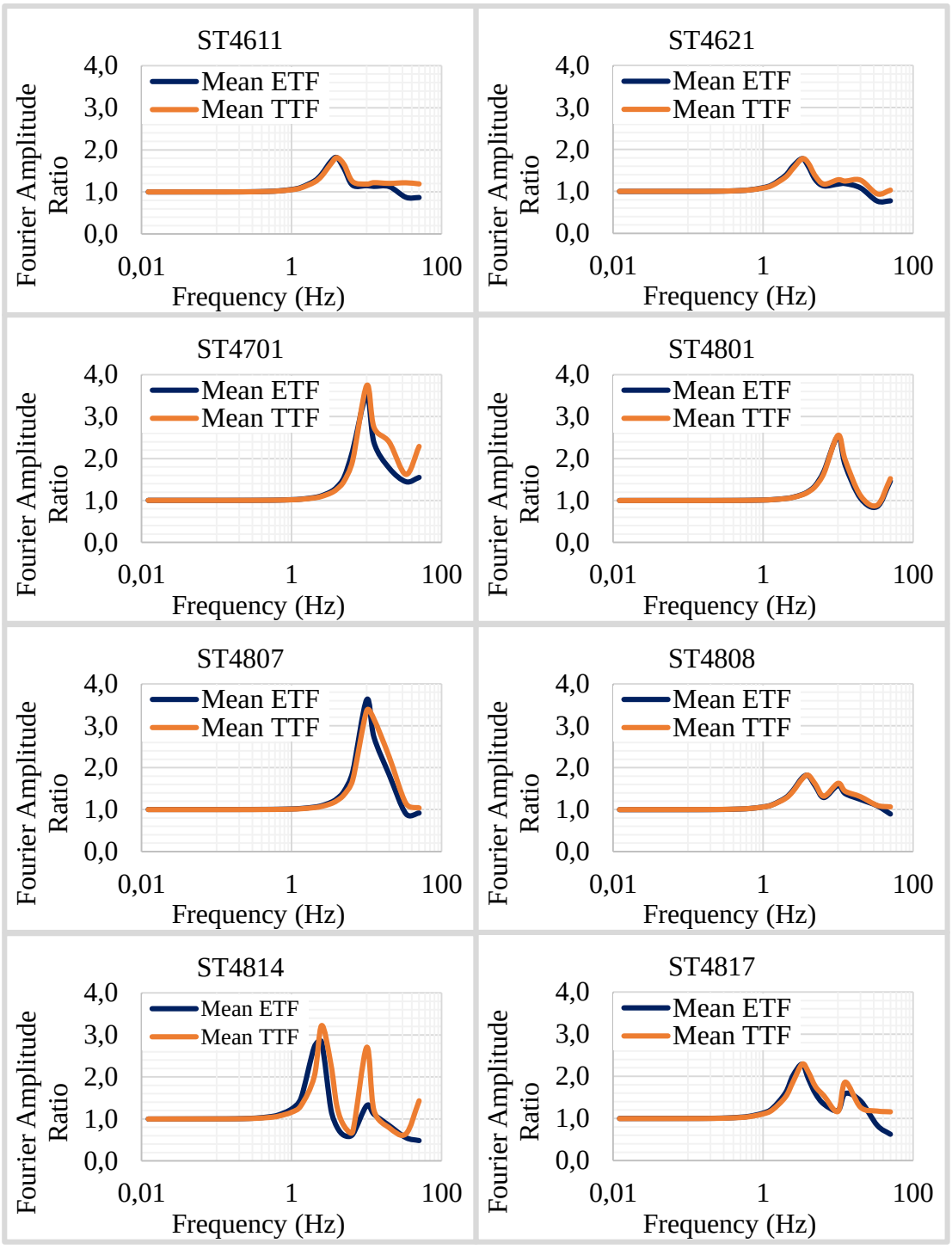

Figure C.4. Comparison of ETF and TTF of candidate stations ST4611, ST4621, ST4701, ST4801, ST4807, ST4808, ST4814, ST4817

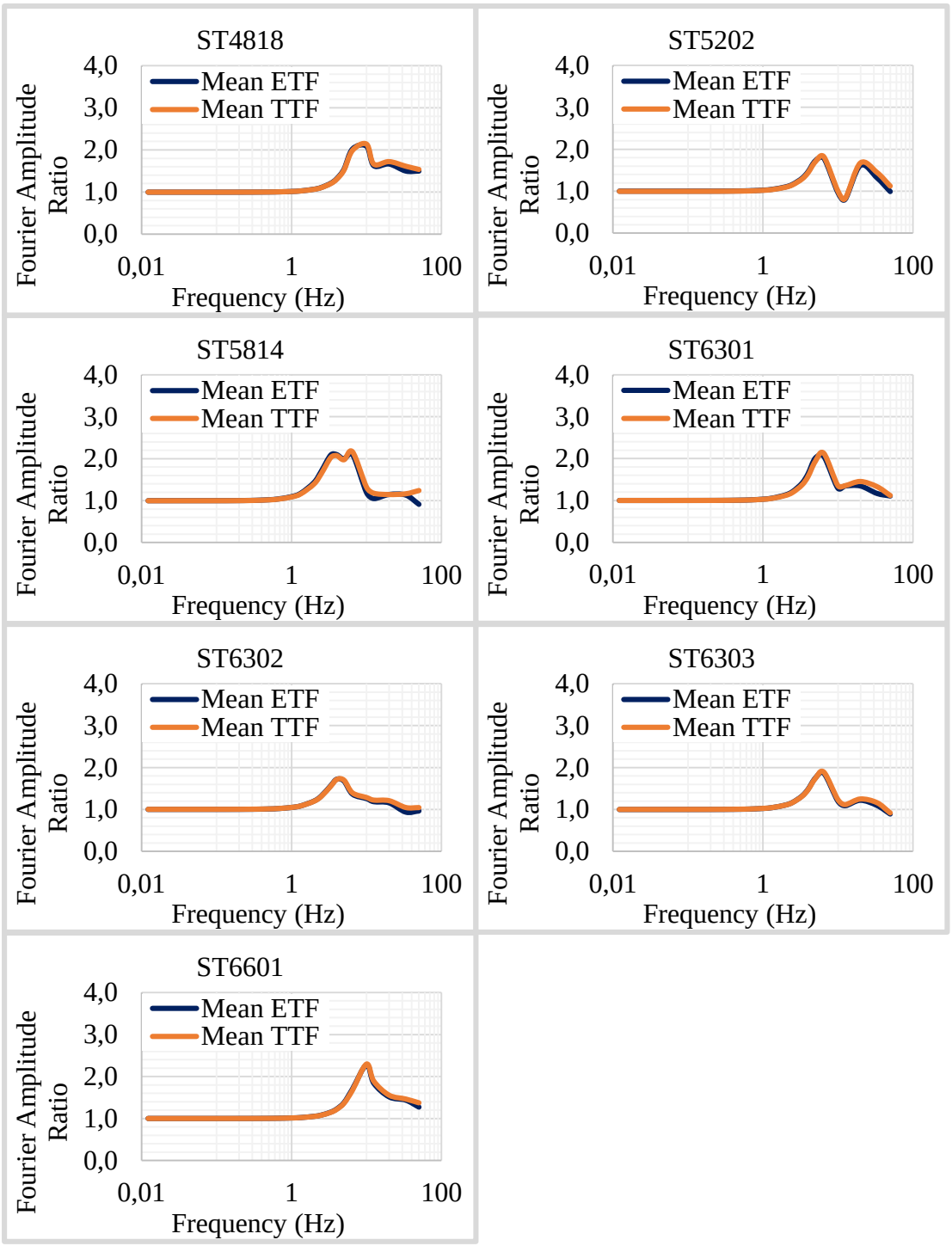

Figure C.5. Comparison of ETF and TTF of candidate stations ST4818, ST5202, ST5814, ST6301, ST6302, ST6303, ST6601